https://doi.org/10.5194/essd-2025-668
Preprint. Discussion started: 13 February 2026

Open Access Earth System Science Data Discussions

A global dataset of δ^{13}C-CH_4 source signatures and associated uncertainties (1998–2022), with a sensitivity analysis to support isotopic inversions

Emeline Tapin[1, *], Antoine Berchet[1], Adrien Martinez[1], Malika Menoud[1, †], Joël Thanwerdas[2], Xin Lan[3, 4], Edward Malina[5], Daniele Gasbarra[5], and Marielle Saunois[1]

[1]Laboratoire des Sciences du Climat et de l'Environnement (LSCE), CEA, CNRS, UVSQ, Université Paris-Saclay, Gif-sur-Yvette, France
[2]Empa, Swiss Federal Laboratories for Materials Science and Technology, Dübendorf, Switzerland
[3]CIRES, University of Colorado Boulder, CO, 80309, United States
[4]NOAA Global Monitoring Laboratory, Boulder, CO, 80305, United States
[5]European Space Agency - ESRIN, Frascati, 00044, Italy
[†]Now at: UNEP, International Methane Emissions Observatory (IMEO), Paris, France
[*]Correspondence: emeline.tapin@lsce.ipsl.fr

Abstract. The isotopic composition of atmospheric methane (δ^{13}C-CH_4) provides critical constraints for attributing methane emissions to specific sources. In this study, we present updated global maps of δ^{13}C-CH_4 source signatures across five major methane-emitting sectors (fossil fuels and geological, agriculture and waste, biomass and biofuel burning, wetlands, and other natural sources) for the period 1998–2022. These maps integrate recent spatially explicit datasets and literature-derived observations, and include explicit quantification of both intrinsic (within-sector) and aggregation-related uncertainties. Building upon previous global compilations, our dataset extends the temporal coverage to 2022, harmonizes sectoral definitions with the Global Methane Budget framework, and provides a consistent and traceable quantification of uncertainties suitable for atmospheric inversions. We assess the influence of these updated source signatures on the modeled atmospheric δ^{13}C-CH_4 using forward simulations within the Community Inversion Framework (CIF) coupled to the LMDz transport model. A comprehensive sensitivity analysis quantifies the impacts of key drivers of uncertainty, including emission flux datasets, OH sinks, kinetic isotope effects, and isotopic source signatures. We show that uncertainties in methane oxidation chemistry and source signatures, particularly from agriculture and waste, dominate the variability in the modeled δ^{13}C-CH_4 signal, while the impact of flux aggregation choices is comparatively minor. The updated isotopic dataset is provided on a global $1° \times 1°$ grid, supporting future atmospheric inversions and improved methane budget assessments at global and regional scales. Practical guidelines for configuring isotopic inversions, including recommended uncertainty specifications and key parameters to optimize, are also provided, offering a framework for next-generation δ^{13}C–CH_4 inversion studies. The final version of the gridded δ^{13}C–CH_4 source signature dataset is available at the ESA Open Science Data portal: https://opensciencedata.esa.int/products/d13c-ch4-signatures-smart-ch4/collection.

https://doi.org/10.5194/essd-2025-668
Preprint. Discussion started: 13 February 2026

Open Access Earth System Science Data Discussions

1 Introduction

Methane (CH_4) is the second most significant anthropogenic greenhouse gas after carbon dioxide (CO_2), playing a major role in current climate change (Stocker, 2014; Forster et al., 2023a). Its atmospheric concentration has more than doubled since pre-industrial times, to reach 1930 ppb in 2024 (Forster et al., 2023b; Lan et al., 2025). Despite its lower abundance compared to CO_2, CH_4 has contributed approximately 31 % (1.19 W m^{-2}) of the total radiative forcing from anthropogenic greenhouse gases since 1750 (Forster et al., 2023b), owing to its high global warming potential (GWP: 29.8 over 100 years, 82.5 over 20 years). Its relatively short atmospheric lifetime (about 9 years; Prather et al., 2012) compared to CO_2 makes it an effective target for near-term climate mitigation strategies (Ocko et al., 2021; Shindell et al., 2021). Global initiatives such as the Global Methane Pledge (launched at COP26) aim to reduce global anthropogenic methane emissions by 30 % by 2030 compared to 2020 levels (Global Methane Pledge, 2023; UNEP, 2022). After a stabilization phase between 1999 and 2006, atmospheric CH_4 resumed its growth after 2007, diverging from trajectories compatible with the Paris Agreement (Nisbet et al., 2019). This renewed increase remains a subject of active scientific debate (Schwietzke et al., 2016; Schaefer et al., 2016; Nisbet et al., 2016; Rigby et al., 2017; Saunois et al., 2017; Worden et al., 2017; McNorton et al., 2018; Thompson et al., 2018; Schaefer, 2019; Turner et al., 2019; Nisbet et al., 2019; Fujita et al., 2020; Zimmermann et al., 2020; Jackson et al., 2020; Basu et al., 2022; Chandra et al., 2024; Thanwerdas et al., 2024), and highlights the urgent need to better constrain methane sources and sinks (e.g., Saunois et al., 2017, 2020, 2025). Since 2020, the growth of atmospheric CH_4 has further accelerated, with unprecedented annual increases recorded between 2020 and 2022 (Michel et al., 2024; Jackson et al., 2024).

Methane emissions have both natural (around 200 Tg CH_4 yr^{-1}, e.g., wetlands, freshwaters, geological sources) and anthropogenic origins (around 320 Tg CH_4 yr^{-1}, e.g., agriculture, fossil fuel, waste) (Saunois et al., 2025). However, large uncertainties persist in the relative contributions of these sources. CH_4 fluxes can be estimated using two main approaches: bottom-up and top-down methods. Bottom-up methods use either emission inventories derived from sectoral activity data and emission factors, or process-based models (Saunois et al., 2025). While they offer detailed source-level information, these estimates are not directly constrained by atmospheric observations and often lead to budgets that are inconsistent with the atmospheric CH_4 burden. In contrast, top-down methods rely on atmospheric measurements of CH_4, including in situ observations from ground-based stations and remote sensing data from satellites, combined with transport models (e.g., LMDZ) to statistically optimize emissions. These approaches are global and observation-based but often struggle to attribute emissions to specific sources when those are co-located or have overlapping temporal signals (Houweling et al., 2017; Bergamaschi et al., 2018). They can also face regional attribution challenges, particularly in areas with sparse or uneven observational coverage (Saunois et al., 2020, 2025). The discrepancies between these two methods, in both magnitude and spatial distribution, highlight major gaps in our understanding of CH_4 sources and sinks (Saunois et al., 2025). Accurately attributing atmospheric CH_4 to specific formation processes can be difficult, especially when co-located sources cannot be differentiated using CH_4 mixing ratios or their spatial and seasonal variability (Bergamaschi et al., 2010, 2013; Kirschke et al., 2013; Saunois et al., 2017). Yet the quantification of individual methane sources is required to implement effective mitigation strategies.

https://doi.org/10.5194/essd-2025-668
Preprint. Discussion started: 13 February 2026

Open Access Earth System Science Data Discussions

The isotopic composition of methane, particularly the ratio of ^{13}C to ^{12}C, can be used for source attribution because it depends on the formation pathway (e.g., Sherwood et al., 2017; Lan et al., 2021b). It is expressed as δ^{13}C-CH_4:

$$\delta^{13}\text{C-CH}_4 = \left(\frac{\left(^{13}\text{C}/^{12}\text{C}\right)_{\text{sample}}}{R_{\text{VPDB}}} - 1 \right) \times 1000, \tag{1}$$

where $\left(^{13}\text{C}/^{12}\text{C}\right)$ denotes the ratio of molar quantities of ^{13}C to ^{12}C in the sample, and $R_{\text{VPDB}} = 1.1113 \times 10^{-2}$ is the ^{13}C/^{12}C ratio of the Vienna Pee Dee Belemnite (VPDB) reference material (Dunn et al., 2024; Camin et al., 2025).

Different CH_4 sources exhibit characteristic δ^{13}C-CH_4 signatures due to their formation processes. Microbial sources (e.g., wetlands, ruminants) typically emit methane that is strongly depleted in ^{13}C, with values ranging from -65 to $-55‰$ (Sherwood et al., 2017, 2021). Geographic variability in livestock emissions reflects differences in plant diets, specifically between C_3 plants (e.g., wheat, rice, trees) and C_4 plants (e.g., maize, sugarcane, tropical grasses), which have distinct carbon isotope compositions (Lan et al., 2021a). Wetland signatures also vary spatially, with more depleted values observed in boreal regions compared to tropical zones (Ganesan et al., 2018; Douglas et al., 2021; Oh et al., 2022). Fossil fuel-related variability can be large, driven by geological origin and processing techniques, with δ^{13}C-CH_4 signatures spanning from -55 to $-30‰$ (Sherwood et al., 2017; Milkov and Etiope, 2018). Geological emissions may also reflect a diversity of geochemical processes, including both thermogenic and microbial pathways, leading to a broader range of δ^{13}C-CH_4 signatures (Sherwood et al., 2017; Etiope et al., 2019). Pyrogenic sources (e.g., biomass and biofuel burning) are enriched in ^{13}C, with values ranging from $-25‰$ to $-15‰$ (Sherwood et al., 2017, 2021), depending on the dominant vegetation type (C_3 or C_4) (Still et al., 2003; Randerson et al., 2012; Lan et al., 2021a). In addition to source-specific isotopic signatures, atmospheric sinks also fractionate methane isotopes through the Kinetic Isotope Effect (KIE). Lighter isotopologues ($^{12}CH_4$) react faster with major oxidants such as OH, Cl, and O(^{1}D) than their heavier counterparts ($^{13}CH_4$), leading to ^{13}C enrichment in the remaining methane. This process alters the isotopic composition of atmospheric CH_4 signal compared to the original source-weighted average signatures.

Over the past two decades, a decreasing trend in atmospheric δ^{13}C-CH_4 has been observed alongside increasing CH_4 concentrations (Nisbet et al., 2023; Michel et al., 2024; Schuldt et al., 2024, 2025). This anti-correlation suggests shifts in source contributions, sink processes, or both, providing additional constraints for methane budget reconstructions. Measurements of δ^{13}C-CH_4 are increasingly integrated into atmospheric inversions to differentiate methane sources through their isotopic signatures (Schwietzke et al., 2016; Lan et al., 2021a). Such data help distinguish co-located or seasonally overlapping sources, assess sectoral contributions, and improve the accuracy of global and regional methane budgets. However, the global network of in situ δ^{13}C-CH_4 measurements remains sparse, resulting in limited spatial coverage and hampering the characterization of regional isotopic gradients. This motivates the exploration of satellite-based retrievals of isotopic methane, which could substantially enhance global coverage. Feasibility studies using instruments such as GOSAT, TROPOMI, and Sentinel-5/UVNS have demonstrated the potential of remote sensing for δ^{13}C-CH_4 observations (Malina et al., 2018, 2019). Recent inversion studies have already begun incorporating δ^{13}C-CH_4 observations from surface networks (e.g., Fujita et al., 2020; Basu et al., 2022; Drinkwater et al., 2023; Thanwerdas et al., 2024), paving the way for future applications that jointly exploit surface and satellite isotopic constraints. However, further studies are needed to properly evaluate possible use of satellite-based isotopic observations in inversions as retrieval uncertainties remain large.

https://doi.org/10.5194/essd-2025-668
Preprint. Discussion started: 13 February 2026

Open Access Earth System Science Data Discussions

A prerequisite for such isotopic inversions is the availability of spatially explicit source signature maps and associated uncertainties. Existing datasets include contributions from Ganesan et al. (2018), Chang et al. (2019), Etiope et al. (2019), Sherwood et al. (2017, 2021), Lan et al. (2021a), Oh et al. (2022), and Menoud (2022). However, limitations remain, particularly in representing uncertainties and covariance structures of isotopic priors (Basu et al., 2022; Thanwerdas et al., 2024). Full sensitivity analyses are also needed to assess the robustness of inversion results with respect to isotopic assumptions (Thanwerdas et al., 2022b).

In this study, we present updated spatially explicit δ^{13}C-CH_4 source signature maps, with associated uncertainty estimates, to support global and regional methane inversions. Our main objectives are to: (i) improve prior knowledge of isotopic compositions for major CH_4 sectors and subsectors, (ii) evaluate the influence of the revised maps on modeled atmospheric δ^{13}C-CH_4 using forward simulations, (iii) quantify the sensitivity of modeled δ^{13}C-CH_4 to key parameters and regions, and (iv) provide uncertainty estimates and recommendations for integrating isotopic constraints into inversion frameworks.

Rather than validating the updated source signature maps against atmospheric observations, the sensitivity analysis focuses on quantifying the impact of key sources of uncertainty on modeled atmospheric δ^{13}C-CH_4 distributions. This sensitivity-centered approach allows us to identify the dominant drivers of variability in the modeled isotopic signal and to provide practical recommendations for future inversion studies. Model-data comparisons, while essential, are beyond the scope of this work and will be addressed in subsequent studies.

The structure of the paper is as follows. Section 2 describes the development of the updated δ^{13}C-CH_4 source signature maps. Section 3 presents the atmospheric modeling framework used for the sensitivity analysis. Section 4 reports and discusses the main results.

2 Development of updated δ^{13}C-CH_4 source signature maps

To improve the spatial and temporal representation of isotopic methane emissions in inverse modeling, we developed a comprehensive set of global maps representing the δ^{13}C-CH_4 source signatures across major methane-emitting sectors and sub-sectors, covering the period 1998–2022. The dataset is available at the ESA Open Science Data portal: https://opensciencedata.esa.int/products/d13c-ch4-signatures-smart-ch4/collection These maps have a spatial resolution of $1° \times 1°$ (global coverage) and a monthly time step, providing improved temporal representation and either matching or improving the spatial resolution of previous datasets. It is based on a synthesis of recent gridded data products and regional observations from peer-reviewed literature (Sect. 2.1). The resulting dataset distinguishes five primary source sectors: fossil fuel exploitation and geological (FFG), agriculture and waste (AGW), biomass and biofuel burning (BB), wetlands (WET), and other natural sources (NAT), each composed of multiple underlying sub-sectors detailed (Sect. 2.2). The associated uncertainties were also calculated (Sect. 2.3). The methodology presented in this section provides a reproducible and publicly available framework to generate δ^{13}C-CH_4 source signature maps at global scale, including explicit quantification of associated uncertainties. All acronyms, sector names and dataset abbreviations used throughout this study are summarized in Table S1 for clarity.

https://doi.org/10.5194/essd-2025-668
Preprint. Discussion started: 13 February 2026

Open Access Earth System Science Data Discussions

2.1 Construction of sub-sector isotopic signature maps

The construction of these maps relied on the integration of the most up-to-date isotopic datasets available for each methane source sub-sector. Table 1 provides an overview of the aggregated source sectors, their sub-sectors, the associated δ^{13}C-CH_4 ranges, isotopic data sources, and corresponding emission fluxes. Gridded products were prioritized when available (e.g., Lan et al. 2021a; Oh et al. 2022), and were supplemented by regional datasets (e.g., Menoud et al. 2024) or literature-based estimates when spatially explicit data were lacking. To ensure representativeness at the global scale, a combination of pixel-level (P), regional (R), and global (G) datasets was used. The temporal resolution of the isotopic signatures was preserved when available in the source datasets, using annual (A) or monthly (M) variations. Otherwise, constant (C) values over the 1998–2022 period were assumed. Each entry in Table 1 is associated with metadata indicating its spatial (P, R, G) and temporal (C, A, M) resolution. All isotopic signatures are expressed relative to the VPDB standard; a discussion of the VPDB vs. historical PDB reference scales and their negligible impact on the simulations is provided in Sect. S1.1. The following sections detail the specific methodologies applied to key source categories and describe how temporal or spatial gaps were addressed to produce a consistent, gridded isotopic dataset.

Treatment of European fossil fuel isotopic signatures

For fossil fuel emissions in Europe, regional measurements from the European Methane Isotope Database (EMID; Menoud et al. 2024) were combined with the global inventory from Lan et al. (2021a) to improve the spatial accuracy of isotopic signatures. The Lan et al. (2021a) dataset, based on the compilation by Sherwood et al. (2021), includes isotopic data from over 13,000 locations from 347 references, though it remains largely U.S. centered. The EMID database provides additional coverage, including both literature data and new measurements from the MEMO^2 project for fossil fuel sources over Europe (European Commission, 2017). The extended global database, combining EMID with Sherwood et al. (2021) and MEMO^2, consists of over 13,313 δ^{13}C measurements from 64 countries.

The integration of these two datasets was conducted as follows:

1. Country-level average δ^{13}C-CH_4 signatures were computed from EMID for some European countries (e.g., UK, Germany, Poland, Romania, France), corresponding to those for which data are available in the EMID inventory.

2. These averages were then combined with Lan et al. (2021a) data using a weighting factor that accounts for the number of additional observations in EMID compared to Sherwood et al. (2021) dataset.

The resulting aggregated values are presented in Table S2.

https://doi.org/10.5194/essd-2025-668
Preprint. Discussion started: 13 February 2026

Open Access Earth System Science Data Discussions

Table 1. Methane emission sectors aggregated for atmospheric modeling, including representative δ^{13}C-CH_4 isotopic signatures and flux estimates over 1998–2022. For each major sector (FFG, AGW, BB, WET, NAT), sub-sectoral values are compiled and aggregated using flux-weighted averages. Isotopic signature ranges reflect observed variability within each sub-sector, based on available spatial and temporal resolution: (P) pixel-level, (R) regional, or (G) global data, and (C) constant, (A) annual, or (M) monthly data. Flux estimates are derived from the Emissions Database for Global Atmospheric Research (EDGARv8; (Crippa et al., 2023)), the Global Fire Emissions Database (GFED4s; (van Wees et al., 2022)), and the Global Methane Budget (GMB; (Martinez et al., 2024)).

Sectors	Sub-sectors	Source Signature (‰, [min–max])	Isotopic Signature References	Flux (Tg y^{-1}, [min–max])	Flux References
FFG	Coal	-43.7 [-64.1– -30.8]	(Lan et al., 2021a; Menoud et al., 2024, ; R,C)	35.6 [23.4–46.8]	EDGARv8
	Oil and gas	-44.0 [-65.0– -29.1]	(Lan et al., 2021a; Menoud et al., 2024, ; R,A)	73.2 [63.0–81.5]	EDGARv8
	Geological	-46.6 [-68.0– -24.3]	(Etiope et al., 2019, ; P,C)	21.1	GMB
	Aggregated	-44.2 [-65.0– -24.3]		**129.9**	
AGW	Livestock	-65.8 [-67.8– -54.6]	(Lan et al., 2021a, ; P,C)	101.4 [91.0–112.3]	EDGARv8
	Wastewater	-50.9	(Menoud et al., 2024, ; G,C)	38.4 [30.4–46.8]	EDGARv8
	Landfills	-56.2	(Menoud et al., 2024, ; G,C)	33.6 [30.4–40.2]	EDGARv8
	Agricultural waste	-54.9	(Menoud et al., 2024, ; G,C)	11.7 [10.8–12.7]	EDGARv8
	Rice	-59.9	(Menoud et al., 2024, ; G,C)	35.8 [32.7–37.4]	EDGARv8
	Aggregated	-60.2 [-67.6– -50.9]		**221.0**	
BB	Biofuel burning	-24.3 [-26.7– -12.6]	(Lan et al., 2021a, ; P,C)	11.9 [11.2–12.3]	EDGARv8
	Biomass burning	-24.2 [-26.7– -12.6]	(Lan et al., 2021a, ; P,C)	13.2 [9.3–20.2]	GFED4s
	Aggregated	-24.3 [-26.7– -12.6]		**25.1**	
WET	Wetlands	-58.6 [-73.6– -18.2]	(Oh et al., 2022, ; P,M)	151.6	GMB
	Aggregated	-58.6 [-73.6– -18.2]		**151.6**	
NAT	Termites	-63.4	(Thompson et al., 2018, ; G,C)	9.9	GMB
	Oceans	-42.0	(Sansone et al., 2001, ; G,C)	11.5	GMB
	Aggregated	-51.9 [-63.4– -42.0]		**21.5**	

Temporal extrapolation

To ensure full temporal coverage over the 1998–2022 period, extrapolation was required for certain datasets whose original time series ended prematurely, specifically for the oil & gas and wetland sub-sectors. In both cases, specific strategies were applied based on known emission trends and isotopic characteristics of source signatures.

For the oil & gas sub-sector, the dataset from Lan et al. (2021a) ends in 2016. Post-2016 values were extrapolated only for U.S. data, based on documented trends in U.S. unconventional gas production (U.S. Energy Information Administration, EIA), notably shale gas, which typically exhibits lighter δ^{13}C-CH_4 signatures than conventional sources (Sherwood et al., 2017). Basin-level variability in both gas production and isotopic composition was accounted for using data from the EIA natural gas reports and published isotopic measurements (Milkov et al., 2020b). Outside the U.S., signatures values were held constant. We adopted a two-step method to extrapolate U.S. δ^{13}C-CH_4 values post-2016:

https://doi.org/10.5194/essd-2025-668
Preprint. Discussion started: 13 February 2026

1. computing basin-weighted δ^{13}C-CH_4 values based on production volumes, using shale gas data per basin (EIA) and basin-specific isotopic signatures (Milkov et al., 2020b);

2. adjusting national-scale δ^{13}C-CH_4 values according to the evolving share of shale gas in total production (EIA).

For wetlands, the monthly δ^{13}C-CH_4 source signature maps from Oh et al. (2022) also end in 2016. To extend the dataset beyond this point, we extrapolated the 2016 seasonal cycle linearly and incorporated the long-term trend in source signatures of $-0.02‰, \mathrm{yr}^{-1}$ observed over the 1984–2016 period (Oh et al., 2022).

2.2 Aggregation into source sectors

To facilitate the integration of δ^{13}C-CH_4 source signatures into atmospheric modeling and to optimize computational efficiency, detailed source sub-sectors were aggregated into broader emission sectors using flux-weighted mean values (more details in Annex S1.2. This aggregation preserves the key isotopic characteristics of different emission types while reducing model complexity. The classification follows the methodology adopted in the Global Methane Budget (GMB Saunois et al., 2025), grouping methane emissions into five principal source categories (Table 1):

- FFG includes emissions from oil, gas, coal, industrial activities, transport, and natural geological seepage.
- AGW encompasses emissions from enteric fermentation, rice cultivation, manure management, and waste decomposition.
- BB sector comprises emissions from open biomass combustion and biofuel use.
- WET includes natural wetland emissions as well as emissions from freshwater systems such as lakes, ponds, reservoirs, rivers, and streams.
- NAT sector covers natural non-wetland emissions, including mostly those from termites and oceanic sources.

This aggregation aims to ensure isotopic representativity within each sector, in line with recent recommendations for source signature consistency (Mannisenaho et al., 2023). An exception may apply to the NAT sector, which encompasses heterogeneous processes (e.g., termite emissions vs. oceanic sources) that are not co-located. These sub-sources were grouped primarily due to their relatively small fluxes and to limit the number of categories for computational efficiency, rather than based on isotopic or spatial consistency. A comprehensive mapping between detailed subcategories and the aggregated sectors used in this study is provided in Table 1. In cases where isotopic data were missing for a specific pixel, flux-weighted average values were used so that each sector's data covered the entire domain.

2.3 Uncertainty assessment of aggregated source signatures

This section describes how uncertainties in aggregated δ^{13}C-CH_4 source signatures are estimated. All uncertainties are evaluated at the global scale, i.e. they are not spatially resolved at the grid-cell level.

https://doi.org/10.5194/essd-2025-668
Preprint. Discussion started: 13 February 2026

Open Access Earth System Science Data Discussions

2.3.1 Total uncertainty (σ_{total})

To quantify the uncertainty associated with the aggregated δ^{13}C-CH_4 source signatures (σ_{total}), we consider two main components: (i) the propagated uncertainty from sub-sector level to sector level (σ_{prop}), i.e. the intrinsic isotopic uncertainty from sub-sector, and (ii) the aggregation uncertainties (σ_{agg}), i.e. the variability introduced when aggregating sub-sector signatures into sector-level values, using a given set of flux weights from prior inventories. Assuming that the two types of uncertainties are independent, the total uncertainty for each aggregated sector is calculated by combining these two components:

$$\sigma_{\mathrm{total}} = \sqrt{\sigma_{\mathrm{prop}}^2 + \sigma_{\mathrm{agg}}^2} \tag{2}$$

The corresponding relative uncertainty (in percentage) is then calculated as:

$$\text{Relative uncertainty } (\%) = \left(\frac{\sigma_{\mathrm{total}}}{\left| \overline{\delta^{13}\mathrm{C}_{\mathrm{sector}}} \right|} \right) \times 100 \tag{3}$$

where σ_{prop} corresponds to the propagated uncertainty at the sector level derived from sub-sector uncertainties (‰), σ_{agg} represents the uncertainty associated with the aggregation method, estimated from sensitivity tests (‰) and $\overline{\delta^{13}\mathrm{C}_{\mathrm{sector}}}$ denotes the mean isotopic signature of the aggregated sector (‰).

Because the propagated uncertainty σ_{prop} is provided as a range, the resulting total uncertainty σ_{total} is also expressed as a corresponding range rather than a single value.

2.3.2 Propagated uncertainty from sub-sectors (σ_{prop})

The term σ_{prop} represents the propagated uncertainty from sub-sector isotopic composition (σ_i) to the aggregated sector level. First, the isotopic uncertainty for each sub-sector (σ_i) is estimated using two complementary approaches, depending on the origin of the data:

- The standard deviations of δ^{13}C-CH_4 values reported in the literature, using the dataset compiled by Menoud et al. (2022), which captures spatial variability and methodological dispersion;
- The uncertainty values reported by Lan et al. (2021a), who derived them from 10,000 Monte Carlo simulations at the grid-cell level, explicitly propagating measurement and modeling errors through source attribution and mixing processes.

The Monte Carlo approach provides a precise uncertainty estimate directly linked to sub-sector diversity but may underestimate broader, large-scale variability and inter-regional differences. Conversely, the literature-based standard deviation offers a more conservative benchmark that captures additional inter-study, regional, and methodological variability. The two approaches (literature-based standard deviations and Monte Carlo uncertainties) provide lower and upper estimates of the sub-sector isotopic uncertainty.

https://doi.org/10.5194/essd-2025-668
Preprint. Discussion started: 13 February 2026

Second, the sub-sector uncertainties (σ_i) are propagated into the aggregated sector uncertainty component (σ_{prop}) using a flux-weighted error propagation approach:

$$\sigma_{\text{prop}} = \sqrt{\sum_i \left(\frac{F_i}{F_{\text{total}}}\right)^2 \sigma_i^2} \tag{4}$$

where F_i is the flux of sub-sector i (Tg yr^{-1}), F_{total} is the total flux of the aggregated sector (Tg yr^{-1}), and σ_i is the isotopic uncertainty of sub-sector i (‰).

The aggregated sector uncertainty (σ_{prop}) is reported as a range, with the lower bound corresponding to the Monte Carlo estimate and the upper bound corresponding to the literature-based estimate.

2.3.3 Aggregation uncertainty (σ_{agg})

This component reflects the sensitivity of aggregated signatures to methodological choices of weighting fluxes in the construction of the aggregated sector dataset. It is evaluated through a series of sensitivity tests (see Sect. 4.2), and computed as the standard deviation across the resulting aggregation scenarios:

$$\sigma_{\text{agg}} = \sqrt{\frac{1}{N}\sum_{j=1}^{N}(\bar{x}_j - \bar{x})^2} \tag{5}$$

where $\bar{x}_j$ is the mean isotopic signature derived from aggregation method j, $\bar{x}$ is the overall mean isotopic signature across all tested methods, and N is the number of tested aggregation methods.

In summary, this framework provides consistent tools to estimate sectoral δ^{13}C-CH_4 uncertainties, combining sub-sector variability and aggregation effects. Because uncertainties in isotopic signature values and their spatial allocation propagate into regional and global inversions, ultimately influencing source attribution, it is particularly important to assess them. The resulting uncertainties are directly usable in atmospheric models and inversions to inform prior error structures and guide optimization choices (see Sect. 4.3.2).

3 Atmospheric framework for sensitivity analysis

Building on recent flux inventories and isotopic signature datasets, we developed updated δ^{13}C-CH_4 source signature maps suitable for atmospheric modeling and inversion studies (see Sect. 2). This section presents how these maps are integrated into forward atmospheric simulations to assess how key parameters uncertainties propagate to the modeled δ^{13}C-CH_4 signal. We first describe the modeling framework used for the simulations (Sect. 3.1), then detail the sensitivity experiments designed to explore the influence of critical drivers, including methane fluxes, fluxes used for isotopic aggregation, OH fields, OH kinetic isotope effects, and isotopic source signatures (Sect. 3.2).

https://doi.org/10.5194/essd-2025-668
Preprint. Discussion started: 13 February 2026

3.1 Description of atmospheric simulations

To assess the influence of key parameters and evaluate the impact of the updated δ^{13}C-CH_4 signature dataset, we conducted a sensitivity analysis based on forward simulations of methane mole fractions and δ^{13}C-CH_4 signals over the period 1998–2022. These simulations were performed within the Community Inversion Framework (CIF; Berchet et al., 2021). The CIF was extended by Thanwerdas et al. (2022a) to incorporate isotopic constraints, enabling the joint simulation and assimilation of CH_4 mole fractions and their δ^{13}C-CH_4 composition. The following subsections describe in detail all components of the forward simulations.

3.1.1 Global transport model

The simulations were conducted using the LMDz transport model, a component of the coupled model from the Institut Pierre-Simon Laplace (IPSL-CM), developed at the Laboratoire de Météorologie Dynamique (LMD; Hourdin et al., 2006). The offline version was used, driven by ECMWF ERA-Interim reanalyses, as described in Chevallier et al. (2005). LMDz operates at a horizontal resolution of $3.75^\circ \times 1.875^\circ$, with 39 vertical hybrid sigma-pressure levels extending up to approximately 75 km. The model time step is 30 minutes. Vertical diffusion is parameterized following the local approach of Louis (1979), while deep convection is represented using the Kerry Emanuel scheme (Remaud et al., 2018) .

3.1.2 Emissions fluxes

Source categories are described in Table 1 with the following emission fluxes: All flux datasets were selected to ensure consistency with the Global Methane Budget (GMB) framework (Saunois et al., 2020, 2025), which provides the reference basis for methane emission assessments.

- **Anthropogenic sources:** Emissions from agriculture, waste, fossil fuel exploitation, and biofuel combustion are taken from the EDGARv8 inventory (Crippa et al., 2023). This dataset provides detailed activity data and region-specific emission factors, enabling realistic representation of spatial and temporal variability across sectors and regions.
- **Biomass burning:** Emissions from wildfires and agricultural burning are derived from the Global Fire Emissions Database (GFED4s) (van Wees et al., 2022). GFED4s integrates satellite observations of burned area, fire radiative power, and biogeochemical model outputs to provide monthly CH_4 flux estimates.
- **Wetlands:** Wetland emissions are estimated using the multi-model mean of 11 process-based models compiled within the Global Methane Budget framework (Martinez et al., 2024). These fluxes are provided as monthly climatological values.
- **Freshwater systems:** Emissions from lakes and reservoirs are based on the CH_4 flux maps by Stavert et al. (2022). Initial global emissions are estimated at 95 Tg yr^{-1}, reduced to 73 Tg yr^{-1} after ice-cover corrections. Following Martinez et al. (2024), emissions are further rescaled by a factor of one-third, resulting in a global total of 53 Tg yr^{-1} (Saunois et al., 2025).

https://doi.org/10.5194/essd-2025-668
Preprint. Discussion started: 13 February 2026

- **Termites:** Termite emissions follow Martinez et al. (2024) based on the S. Castaldi model, providing a spatially explicit global climatology without accounting for seasonal variability.

- **Geological methane:** Geological emissions use the gridded climatology from Etiope et al. (2019), rescaled to a total global flux of 23 Tg CH_4 yr^{-1} by Martinez et al. (2024). Offshore geological emissions, including marine seepage, are excluded to avoid double counting.

- **Oceanic methane:** Ocean emissions rely on the climatological dataset of Weber et al. (2019), which combines microbial CH_4 production in the water column and geological seepage from seafloor sediments. These emissions are considered seasonally invariant and included as a static component of the total CH_4 flux budget (Martinez et al., 2024).

3.1.3 Initial conditions

Initial conditions for CH_4 and δ^{13}C-CH_4 for the year 1998 were derived from an inversion covering the period 1988–2020 (Thanwerdas et al., 2024). A spin-up period from 1998 to 2016 was used to allow the model to adjust to realistic atmospheric gradients, particularly for δ^{13}C-CH_4 (Tans, 1997). Only the period 2016–2020 is analyzed to ensure that the model has reached a stable state and to enable direct comparison between simulations, which differ only from the perturbed parameters (see Sect. 3.2).

3.1.4 Chemistry

Methane oxidation is simulated using the generic chemical module of the offline LMDz model (Pison et al., 2009; Thanwerdas et al., 2022b). The chemical scheme includes reactions with hydroxyl radicals (OH), excited atomic oxygen ($O(^1D)$), and chlorine radicals (Cl). Oxidant concentrations are prescribed from precomputed daily 3-D fields summarized in Table 2.

- **Hydroxyl radicals (OH):** OH is the primary sink for atmospheric methane. Monthly mean OH fields are taken from LMDz-INCA simulations (Hauglustaine et al., 2004), driven by consistent meteorological forcing with the transport model.

- **Excited atomic oxygen ($O(^1D)$):** $O(^1D)$ contributes mainly to methane oxidation in the stratosphere. A monthly climatology from the TRANSCOM project (Patra et al., 2011) is used.

- **Chlorine radicals (Cl):** Methane destruction by Cl radicals is particularly relevant in both the marine boundary layer and the stratosphere. Cl fields are based on the dataset of Wang et al. (2021), as recommended by Thanwerdas et al. (2022b), and include both tropospheric and stratospheric concentrations.

Isotopic fractionation from CH_4 oxidation is expressed by the kinetic isotope effects (KIEs), which quantify the difference in reaction rates between $^{12}CH_4$ and $^{13}CH_4$. The KIE values used for each oxidant are summarized in Table 2. A sensitivity analysis is conducted on the OH-KIE value, given its significant impact on the atmospheric $\delta^{13}CH_4$ signal (see Sect. 3.2).

https://doi.org/10.5194/essd-2025-668
Preprint. Discussion started: 13 February 2026

Open Access Earth System Science Data Discussions

Table 2. Fractionation coefficients for methane oxidation reactions with OH, O(^{1}D), and Cl. The kinetic isotope effect (KIE) values are shown for each reaction, along with their respective references and sources of the 3D oxidant fields. For Cl, the KIE is expressed as a temperature-dependent exponential function, where T denotes temperature in Kelvin (K).

Oxidant	$k(^{12}CH4)/k(^{13}CH4)$	**Reference**	**3D Field Source**
OH	1.0039	Saueressig et al. (2001)	LMDz-INCA (Hauglustaine et al., 2004)
O(^{1}D)	1.013	Saueressig et al. (2001)	TRANSCOM (Patra et al., 2011)
Cl	$1.043 \times e^{6.455K/T}$	Saueressig et al. (1995)	Wang et al. (2021)

3.1.5 Soil sink

Soil uptake is a significant sink for atmospheric methane, and accounts for approximately 35 Tg CH_4 yr^{-1} in the global methane budget (Saunois et al., 2025). Moreover, the soil sink is known to induce isotopic fractionation, which must be accounted for in forward simulations of the isotopic signal (Snover and Quay, 2000). In this study, rather than using a fixed negative flux, we represent soil uptake as a first-order deposition process, where the deposition velocity v_{dep} is computed from prescribed soil fluxes and modeled surface CH_4 concentrations. This approach allows the sink to respond to atmospheric gradients and enables a consistent application of isotopic fractionation. Representing soil uptake via a deposition velocity ensures that the isotopic fractionation is applied dynamically to both $^{12}CH_4$ and $^{13}CH_4$, in proportion to their atmospheric concentrations and the kinetic isotope effect.

The monthly deposition velocity is calculated as:

$$v_{\text{dep}} = \frac{F_{\text{soil}}}{C_{\text{CH}_4}} \tag{6}$$

where F_{soil} is the prior soil uptake flux from the GMB dataset (Martinez et al., 2024), and C_{CH_4} is the modeled surface CH_4 mole fraction from inversion (Thanwerdas et al., 2024).

To account for isotopic fractionation during methane uptake by soils, a kinetic isotope effect (KIE) is applied. The deposition velocity for $^{13}CH_4$ is computed as:

$$v_{\text{dep},\,^{13}\text{CH}_4} = \frac{v_{\text{dep},\,^{12}\text{CH}_4}}{\text{KIE}_{\delta^{13}\text{C}}} \tag{7}$$

with a fractionation factor $\text{KIE}_{\delta^{13}\text{C}} = 1.020$, based on the experimental results of Snover and Quay (2000).

The methodology presented in this section provides a consistent framework for simulating atmospheric CH_4 mole fractions and δ^{13}C-CH_4 signals using the CIF coupled to the LMDz transport model.

3.2 Protocol for sensitivity experiments

A series of sensitivity simulations was conducted to assess the impact of key input uncertainties on the modeled spatial and temporal variability of atmospheric δ^{13}C-CH_4 signal and CH_4 mole fractions. The purpose of these sensitivity experiments

https://doi.org/10.5194/essd-2025-668
Preprint. Discussion started: 13 February 2026

320 and the way input and output uncertainties are propagated within the inversion framework are illustrated in Fig. 3. These experiments, summarized in Table 3, are grouped into four main categories:

Table 3. Overview of the simulation setups used for the sensitivity analysis. Simulations are grouped into three main categories (*Category*): chemistry, aggregation, and fluxes. The column *Subcategory* specifies the specific parameter being tested (e.g., OH fields, KIE values, wetland emissions, freshwater emissions, anthropogenic emissions). Simulation names in *italic* correspond to the reference simulations used in each category. Models and datasets used include: INCA (Hauglustaine et al., 2004), IAV (Patra et al., 2021), MCFCAL (Patra et al., 2011) for OH fields, Saueressig (Saueressig et al., 2001) and Cantrell (Cantrell et al., 1990) for OH kinetic isotope effects (KIE), EDGARv8 (Crippa et al., 2023), GFEI v2 (Scarpelli et al., 2022), CEDS v2021-04-21 (O'Rourke et al., 2021), and GAINSv4 (Höglund-Isaksson et al., 2020) for anthropogenic emissions, GMB (Martinez et al., 2024) for freshwater emissions, and various versions of wetland emissions from Saunois et al. (2020), including GMB_Mean (climatological mean of 11 models), GMB_NoClimato (monthly mean of 11 models), and LPJ (LPJ-wsl model).

Category	**Subcategory**	**Simulation name**	**OH**	**KIE**	**Flux aggregation**	**Fluxes**		
						Wetlands	**Freshwaters**	**Anthropogenic**
Chemistry	OH	*OH_INCA*	**INCA**	Saueressig	EDGAR	GMB_Mean	No	EDGAR
		OH_IAV	**IAV**	Saueressig	EDGAR	GMB_Mean	No	EDGAR
		OH_MCFCAL	**MCFCAL**	Saueressig	EDGAR	GMB_Mean	No	EDGAR
		OH_INCA_2024	**INCA**	Saueressig	EDGAR	GMB_Mean	No	EDGAR
	KIE	*KIE_SAUERESSIG*	INCA	**Saueressig**	EDGAR	GMB_Mean	No	EDGAR
		KIE_CANTRELL	INCA	**Cantrell**	EDGAR	GMB_Mean	No	EDGAR
Aggregation	Aggregation	*AGGREG_EDGAR*	INCA	Saueressig	**EDGAR**	GMB	No	EDGAR
		AGGREG_GFEI	INCA	Saueressig	**GFEI**	GMB_Mean	No	EDGAR
		AGGREG_CEDS	INCA	Saueressig	**CEDS**	GMB_Mean	No	EDGAR
		AGGREG_GAINS	INCA	Saueressig	**GAINS**	GMB_Mean	No	EDGAR
		NO_AGGREG	INCA	Saueressig	**None**	GMB_Mean	No	None
Fluxes	Wetlands	*WET_GMB*	INCA	Saueressig	EDGAR	**GMB_Mean**	No	EDGAR
		WET_SAT_WET_CH4	INCA	Saueressig	EDGAR	**SatWetCH$_4$**	No	EDGAR
		WET_GMB_NO_CLIMATO	INCA	Saueressig	EDGAR	**GMB_NoClimato**	No	EDGAR
		WET_LPJ	INCA	Saueressig	EDGAR	**LPJ**	No	EDGAR
	Freshwaters	*FLUX_NO_FRESH*	INCA	Saueressig	EDGAR	GMB_Mean	**No**	EDGAR
		FLUX_FRESH	INCA	Saueressig	EDGAR	GMB_Mean	**Yes**	EDGAR
	Anthropogenic	*ANTHROPO_EDGAR*	INCA	Saueressig	EDGAR	GMB_Mean	No	**EDGAR**
		ANTHROPO_GAINS	INCA	Saueressig	EDGAR	GMB_Mean	No	**GAINS**
		ANTHROPO_CEDS	INCA	Saueressig	EDGAR	GMB_Mean	No	**CEDS**
		ANTHROPO_GFEI	INCA	Saueressig	EDGAR	GMB_Mean	No	**GFEI**

https://doi.org/10.5194/essd-2025-668
Preprint. Discussion started: 13 February 2026

- **Flux aggregation:** We tested the sensitivity of modeled outputs to the choice of emission inventories used for isotopic flux aggregation. Fluxes were aggregated using different anthropogenic inventories, namely the Emissions Database for Global Atmospheric Research (EDGARv8; Crippa et al. 2023), the Global Fuel Exploitation Inventory (GFEIv2; Scarpelli et al. 2022), the Community Emissions Data System (CEDSv2021; O'Rourke et al. 2021), and the Greenhouse Gas and Air Pollution Interactions and Synergies model (GAINSv4; Höglund-Isaksson et al. 2020). These datasets are collectively referred to as "inventories" hereinafter. We also tested the effect of increasing the number of aggregated source categories (from 5 to 14) to assess the trade-offs between computational efficiency and isotopic detail (see Section 2.2).

- **Chemistry:** Sensitivity to CH_4 oxidative loss processes was explored by using different OH fields, including the INCA model (Hauglustaine et al., 2004), the TRANSCOM-MCFCAL ensemble (Patra et al., 2011), and the IAV scenario (Patra et al., 2021), as well as by varying the kinetic isotope effects (KIEs) associated with CH_4 oxidation by OH radicals (Cantrell et al., 1990; Saueressig et al., 2001).

- **CH_4 fluxes:** Sensitivity to the choice of methane flux datasets was assessed for three sectors: wetlands (GMB climatology and interannual variability (IAV) (Martinez et al., 2024), LPJ from GMB (Saunois et al., 2020), SatWetCH_4 (Bernard et al., 2024)); freshwater systems (on/off configuration using GMB (Martinez et al., 2024)); and anthropogenic sources (EDGARv8, CEDSv2021, GAINSv4, GFEI).

- **Isotopic signature:** For the five main source sectors, a Monte Carlo ensemble (five members) was generated to isolate the influence of source signature uncertainties on the modeled δ^{13}C-CH_4. Isotopic signatures were randomly perturbed within their sector-specific uncertainty ranges, assumed to follow normal distributions (see Section 4.1.3). Each spatial domain draws independently from this distribution, so that different regions may receive different perturbed values within the same Monte Carlo member. Further details, including the statistical parameters used for each sector, are provided in Table S3.

The sensitivity analysis focuses on the period from 2016 to 2020 included. The years from 1998 to 2015 are used as a spin-up period to let the model adjust. The simulation outputs from January 2016 to December 2020 are analyzed. The years 2021–2022 are excluded to ensure consistency across all simulations, as some of the emission inventories used (e.g., GAINS) are only available up to 2020. These simulations aim to quantify the uncertainties introduced by methodological choices during the construction of isotopic signature maps and their propagation into modeled outputs, namely atmospheric methane mole fractions and isotopic signals. They also allow quantification of the individual contribution of each factor to the overall uncertainty in modeled methane mole fractions and isotopic signals.

The sensitivity of each parameter was quantified using the relative standard deviation (RSD), defined as:

$$\mathrm{RSD} = \frac{\sigma}{\mu} \times 100\% \tag{8}$$

where σ is the standard deviation (SD) and μ is the mean of the modeled outputs (simulated methane mole fraction and isotopic composition) across the sensitivity simulations for a given parameter, computed at each pixel at the surface level. Both the SD

https://doi.org/10.5194/essd-2025-668
Preprint. Discussion started: 13 February 2026

and the RSD were calculated within each sensitivity category (aggregation, chemistry, fluxes, isotopic signatures) to isolate the influence of each individual parameter set on the modeled outputs.

The SD provides an absolute measure of dispersion (e.g., in ppb for CH_4 mole fraction values or in ‰, for isotopic signals), while the RSD expresses this variability relative to the mean, allowing direct comparison between parameters of different magnitudes. An elevated RSD indicates that the modeled output is highly sensitive to the parameter in question and highlights a potential leverage point for reducing overall uncertainty. Conversely, a low RSD suggests that the parameter has only a limited impact on the variability of the output field.

The RSD is particularly useful in isotopic modeling, where flux amplitude, isotopic source signature, and chemical processes interact in non-linear ways. Uncertainties in the isotopic composition of a source propagate to the RSD of the modeled isotopic signal, but large fluxes from other regions with well-constrained isotopic signatures can dampen this variability.

The modeling framework described in this section enables a systematic exploration of the sensitivity of atmospheric δ^{13}C-CH_4 to variations in fluxes, chemical sinks, and isotopic source signatures. We now examine the updated δ^{13}C-CH_4 source signature maps in detail and quantify their uncertainties before analyzing the results of the sensitivity simulations.

4 Results and discussion

This section presents the key results of this study, including the spatial and temporal characteristics of the updated δ^{13}C-CH_4 source signature maps and their associated uncertainties (Sect. 4.1), as well as the atmospheric sensitivity simulations outcomes (Sect. 4.2). The objectives are to identify dominant sources of uncertainty affecting the modeled δ^{13}C-CH_4 signal and to provide guidelines to integrate the updated isotopic dataset into atmospheric inversions (Sect. 4.3).

4.1 Updated δ^{13}C-CH_4 source signature maps

Building updated δ^{13}C-CH_4 maps with quantified uncertainties is a prerequisite for improving the robustness of future top-down methane budget assessments. In this section, we present the new δ^{13}C-CH_4 source signature maps developed for this study, based on the methodology detailed in section 2. We describe the spatial patterns of aggregated sectoral signatures (Sect. 4.1.1), their temporal variability over the 1998–2022 period (Sect. 4.1.2), the associated uncertainties (Sect. 4.1.3), and provide a comparison with existing datasets (Sect. 4.1.4).

4.1.1 Updated δ^{13}C-CH_4 source signatures

Figure 1 presents the aggregated global maps of δ^{13}C-CH_4 source signatures averaged over the period 1998–2022. The spatial variability in these maps reflects both the diversity of isotopic signatures across sub-sectors (see Sect. 1) and the spatial distribution of methane fluxes within each grid cell. The fluxes used for aggregation are detailed in Table 1, which also reports the mean, minimum, and maximum δ^{13}C-CH_4 source signatures. Additional maps showing individual sub-sectors are provided in Figure S1. The key spatial features for δ^{13}C-CH_4 of each sector are summarized below:

https://doi.org/10.5194/essd-2025-668
Preprint. Discussion started: 13 February 2026

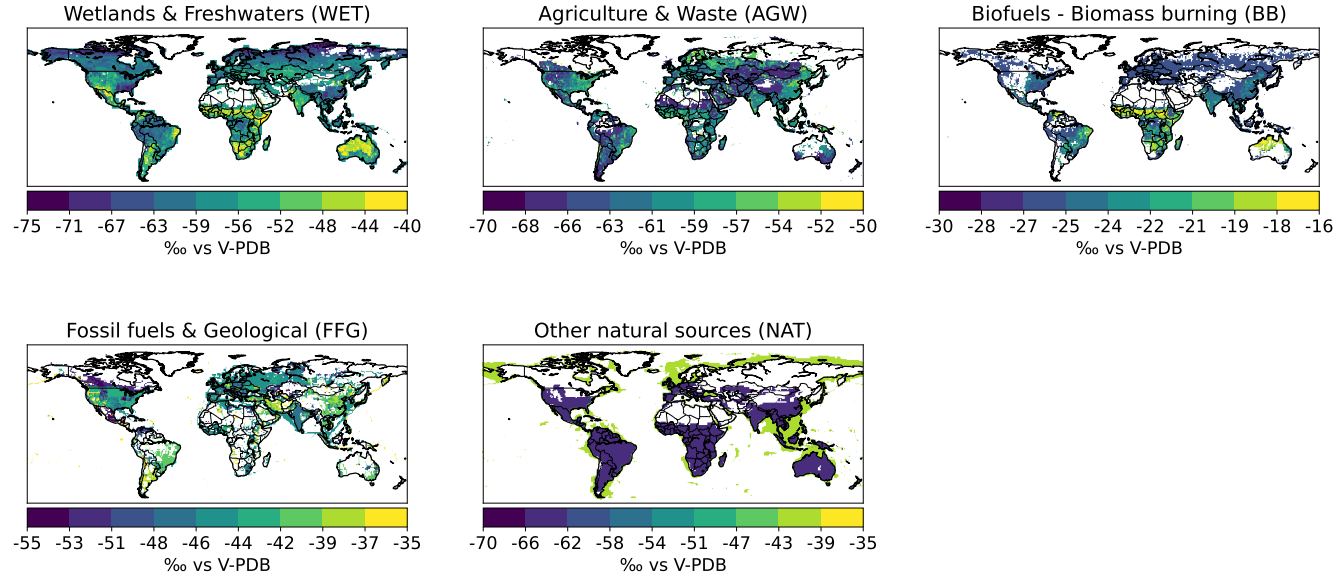

Figure 1. Maps of δ^{13}C-CH_4 source signatures (‰) for each of the five source sectors, flux-weighted averages over 1998–2022. Only grid cells with CH_4 fluxes exceeding 0.025 mg CH_4 m^{-2} day^{-1} are shown. Note that color scales differ between panels to better highlight spatial patterns within each source sector.

- **FFG**: More enriched signatures (close to -40‰) are observed in regions with oil and gas exploitation (e.g., Middle East, USA), while more depleted values (below -50‰) occur in coal-dominated, oil sands, or geological seepage areas (e.g., Canada). These patterns reflect the isotopic diversity of fossil sub-sources, as documented in previous studies (Figures S1, S2; Schwietzke et al. 2016; Sherwood et al. 2017; Milkov et al. 2020b; Menoud et al. 2022).

- **AGW**: Spatial variability results from the balance between depleted livestock emissions (~ -66‰) and more enriched waste-related sources (-51 to -56‰). Urbanized regions (e.g., South-East Asia, Europe) show enriched signatures due to dominant landfill and wastewater emissions, whereas rural areas with rice and livestock (e.g., Argentina, Sub-Saharan Africa) are more depleted (Figures S1, S2).

- **BB**: Isotopic gradients are primarily latitudinal, driven by the distribution of C_3 and C_4 plants. Tropical and subtropical regions dominated by C_4 vegetation exhibit more enriched values, while boreal regions show more depleted signatures (Still et al., 2003; Randerson et al., 2012; Lan et al., 2021a).

- **WET**: Generally depleted values (-50 to -70‰) are observed, with more depleted signatures in high-latitude and boreal wetlands, and relatively enriched ones in tropical wetlands (Oh et al., 2022).

https://doi.org/10.5194/essd-2025-668
Preprint. Discussion started: 13 February 2026

– **NAT**: This sector includes geographically distinct emissions from oceans (more enriched, $\sim -42‰$) and termites (more depleted, $\sim -65‰$). The corresponding isotopic signatures reflect the spatial distribution of each sub-source, as shown in the sub-sector maps (Figures S1, S2).

The spatial patterns described above directly influence the simulated atmospheric δ^{13}C-CH_4 signal, which may affect the results of inverse modeling. Furthermore, uncertainties in sub-sector isotopic values and their spatial allocation propagate into regional and global inversions, ultimately influencing source attribution. A detailed quantification of these uncertainties is therefore essential to assess their potential impact and guide the design of robust inversion frameworks (Sect. 4.1.3).

The maps also highlight regions where different source types co-occur, potentially complicating the separation of natural and anthropogenic emissions. For example, tropical regions such as Southeast Asia, parts of Africa, and northern South America host both WET and AGW emissions in close proximity. The spatial co-location and similarity of isotopic signatures between these sources can produce blended atmospheric signals, making it challenging to disentangle their respective contributions in top-down inversions. These overlaps underscore the importance of high-resolution spatial and temporal information in both methane fluxes and isotopic signatures to improve source attribution in complex emission environments.

4.1.2 δ^{13}C-CH_4 source signature timeseries

Figure 2 presents the monthly δ^{13}C-CH_4 source signature time series for the methane sectors considered in this study over the period 1998–2022. The time series are based on flux-weighted averages. In the following, we describe the temporal evolution and variability of each sector's isotopic signature and discuss the underlying drivers. Most aggregated source sectors show limited temporal variability in their δ^{13}C-CH_4 signature over the 1998–2022 period, with typical long-term change changes below 1 ‰. The isotopic signature of FFG sources exhibits a slight enrichment over time, increasing from approximately -44.6 ‰ in the early 2000s to around -43.9 ‰ after 2020. Several factors can explain this increase. First, the rapid expansion of shale gas production, particularly in North America after 2010, introduced additional emissions with relatively enriched isotopic signatures compared to conventional natural gas (Milkov et al., 2020a). In the United States, shale gas accounted for 48% of total dry natural gas production in 2013 and reached 82% by 2023 (IEA, 2013-2023; Saunois et al., 2025). Second, the relative contributions of fossil fuel subsectors have evolved over the past two decades. According to Saunois et al. (2025), based on the synthesis of multiple emission inventories, including EDGARv6.0 and v7.0 (Ferrario et al., 2021; Crippa et al., 2023), GAINSv4.0 (Höglund-Isaksson et al., 2020), CEDS (O'Rourke et al., 2021), the share of coal-related emissions, typically more depleted in δ^{13}C-CH_4, increased from approximately 21% of total fossil fuel emissions in the early 2000s to about 25% in the 2010s. Meanwhile, oil and gas emissions, associated with less depleted signatures, also grew but were partially counterbalanced by this increasing coal contribution. This sectoral shift has likely moderated the enrichment of the global signature driven by shale gas. Third, geological sources are considered stable over time, both in terms of flux and isotopic signature, providing a background that buffers the sector's temporal variability. Overall, these combined effects explain the modest but persistent enrichment observed in the FFG sector's isotopic signature over the past two decades. No significant seasonal variation is detected for FFG sector, which is consistent with the absence of seasonal modulation in the underlying inventories. However,

https://doi.org/10.5194/essd-2025-668
Preprint. Discussion started: 13 February 2026

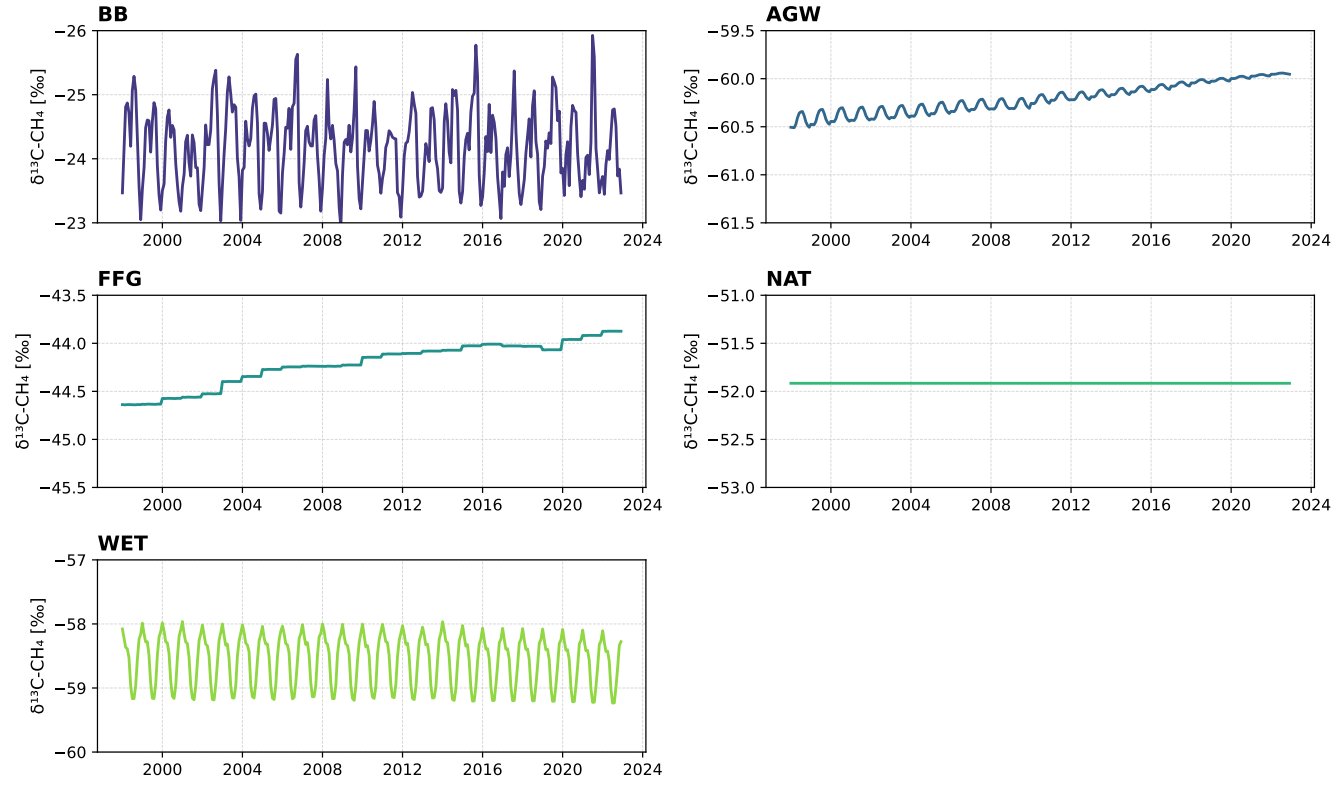

Figure 2. Monthly δ^{13}C-CH_4 source signatures from major sectors over the period 1998–2022. Each subplot corresponds to a specific sector (AGW, WET, BB, FFG, NAT).

real-world temporal variability may not be fully captured by inventories. Geopolitical events (e.g., changes in gas trade flows) and evolving gas processing or distribution practices could alter the isotopic composition of emissions over time. While isotopic signatures are generally stable (Schoell et al., 1993), shifts in the relative contribution of end-member sources or changes in gas composition could induce detectable trends (Schwietzke et al., 2014; Sherwood et al., 2017). Such factors remain difficult to assess without dedicated observational constraints.

The AGW signature shows a slight enrichment from about -60.4 to -59.9 ‰. Since the isotopic values of the subcategories (e.g., livestock, wastewater, landfill, rice, and agricultural waste) are held constant, this change reflects a redistribution of fluxes within the AGW sector. Specifically, the relative contribution of livestock and rice cultivation, which together accounted for approximately 69% of AGW emissions in 2000–2009, decreased to around 68% in 2010–2019. At the same time, waste-related sources (i.e., landfills, wastewater, and agricultural waste) increased from about 31% to 32% of AGW emissions over the same period. This subtle but consistent shift towards more enriched waste sources likely drives the observed isotopic enrichment, particularly in rapidly developing regions with strong urban waste emissions (Saunois et al., 2025). Moreover, the AGW sector exhibits a seasonal cycle in its isotopic signature, primarily driven by rice cultivation, which is the only sub-sector with

https://doi.org/10.5194/essd-2025-668
Preprint. Discussion started: 13 February 2026

pronounced seasonal variability in emissions. The slight reduction in the relative contribution of rice, from about 19% to 16% of total AGW emissions between 1998 and 2022, leads to a corresponding decrease in the seasonal amplitude of the δ^{13}C-CH_4 signature, reflecting the reduced influence of this highly seasonal sub-sector compared to other more temporally stable AGW sources. In addition to changes in source distribution, long-term shifts in agricultural practices may slightly influence isotopic source signatures. For instance, changes in livestock diet, such as a varying balance between C3 and C4 feeds, and large-scale changes in atmospheric δ^{13}C–CO_2 may both affect CH_4 isotopic composition. Chang et al. (2019) showed that the progressive depletion of atmospheric δ^{13}C–CO_2 since the 1960s, driven by fossil fuel combustion, has led to a corresponding decline in δ^{13}C of both C3 and C4 plants. This trend propagates through the food chain, ultimately affecting the δ^{13}C–CH_4 signature from ruminants. Although such effects likely occur, they are not yet explicitly represented in our dataset due to a lack of systematic isotopic observations that track temporal changes in agricultural feedstocks or cultivation practices.

The WET isotopic signature remains largely stable over the period 1998–2022, with only a minor change from approximately -58.6 to -58.7 ‰, consistent with the trend reported by Oh et al. (2022). More importantly, wetlands exhibit a strong seasonal cycle in δ^{13}C-CH_4 signatures, with more depleted values during the summer months. This seasonal variation is driven by the dominance of methane emissions from boreal wetlands during summer, which are isotopically lighter than emissions from tropical wetlands (Oh et al., 2022).

The BB isotopic signature remains stable around -24.3 ‰ throughout the study period, consistent with the identical δ^{13}C–CH_4 signatures prescribed for biomass burning and biofuel burning subcategories (Lan et al., 2021a). However, the sector exhibits a pronounced seasonal cycle, with less depleted values during the boreal winter. This pattern reflects the higher contribution of biomass burning emissions from the Southern Hemisphere during this period, which are characterized by relatively enriched δ^{13}C–CH_4 signatures (see Fig. 1).

The NAT isotopic signature remains constant throughout the period, as expected. Values for both subcategories (oceanic and termites) are derived using climatological fluxes and fixed δ^{13}C-CH_4 values, leading to negligible variability over time.

Overall, the temporal evolution of sectoral isotopic signatures highlights the combined influence of sector-specific trends, source redistributions, and seasonal dynamics on the isotopic composition of global methane emissions.

4.1.3 Uncertainty in δ^{13}C-CH_4 source signature

Table 4 presents the uncertainty ranges associated with the δ^{13}C-CH_4 source signatures for each major sector and their respective sub-sectors. The uncertainty in aggregated δ^{13}C-CH_4 source signatures arises from two primary components: (1) the variability across sub-sectors, expressed first as the range of sub-sector uncertainties (σ_i), and then as a flux-weighted propagated uncertainty to the sector level (σ_{prop}), and (2) the aggregation uncertainty (σ_{agg}), reflecting the sensitivity of sectoral signatures to the prior flux distribution used for aggregation (see methodology in Sect. 2.3). In the following, we first analyse the uncertainty intrinsic to each sectors, then examine the additional uncertainty introduced by aggregation at the sector level, and finally discuss the total propagated uncertainties and their implications for methane source attribution.

https://doi.org/10.5194/essd-2025-668
Preprint. Discussion started: 13 February 2026

Open Access Earth System Science Data Discussions

Sub-sector	σ_i (‰)	Sector	σ_{prop} (‰)	σ_{agg} (‰)	σ_{total} (‰)	σ_{Menoud} (‰)	$\overline{\text{Uncertainty}}_{\text{Menoud}}$ (‰)
Coal	3.0 – 10.0						
Oil and Gas	1.0 – 7.7	**FFG**	1.1 – 5.2	1.0	1.5 – 5.3	9.0	1.9
Geological	1.5 – 1.6						
Livestock	0.2 – 5.8						
Wastewater	1.7 – 3.2						
Landfills	1.7 – 3.4	**AGW**	0.5 – 2.8	1.7	1.8 – 3.3	6.5	2.0
Agricultural waste	1.7 – 6.6						
Rice	1.1 – 4.5						
Biofuel burning	0.8 – 11.2	**BB**	0.5 – 6.0	0.1	0.5 – 6.0	6.9	1.9
Biomass burning	0.8 – 5.2						
Wetlands	0.4 – 8.2	**WET**	0.4 – 8.2	0.0	0.4 – 8.2	8.1	3.2
Oceans	2.8 – 7.6	**NAT**	2.0 – 5.4	0.0	2.0 – 5.4	7.6	3.2
Termites	2.8 – 7.6						

Table 4. Summary of uncertainty estimates for aggregated δ^{13}C-CH_4 source signatures by sector (in ‰), based on data from 2016–2020. Sector acronyms are as follows: FFG = Fossil Fuels & Geological sources, AGW = Agriculture & Waste, BB = Biomass & Biofuel Burning, WET = Wetlands, NAT = Other Natural sources. σ_i refers to the range of isotopic uncertainties across sub-sectors (in ‰). These are taken from Lan et al. (2021a) (lower bound) and Menoud et al. (2022) (upper bound). The sub-sector uncertainty for geological sources is taken from Etiope et al. (2019). σ_{prop} represents the sector-level propagated uncertainty, derived from the flux-weighted combination of sub-sector uncertainties. σ_{agg} corresponds to the uncertainty introduced by the aggregation method, based on sensitivity tests using different prior flux inventories. σ_{total} is the total combined uncertainty, calculated as $\sigma_{\text{total}} = \sqrt{\sigma_{\text{prop}}^2 + \sigma_{\text{agg}}^2}$. σ_{Menoud} and $\overline{\text{Uncertainty}}_{\text{Menoud}}$ refer to the standard deviation and mean uncertainty reported by Menoud (2022) across all available literature. Note that since σ_{prop} is derived from the same base dataset, the propagated and total uncertainties (σ_{prop}, σ_{total}) are not fully independent of σ_{Menoud} and $\overline{\text{Uncertainty}}_{\text{Menoud}}$, but provide complementary comparison insight.

Propagated uncertainty from sub-sectors (σ_{prop})

The propagated uncertainty at the aggregated sector level, denoted σ_{prop}, captures the combined effect of isotopic variability among sub-sectors within each source category. It is computed using a flux-weighted combination of individual sub-sector uncertainties (σ_i), as described in Sect.2.3. These sub-sector uncertainties reflect both the intrinsic heterogeneity of emission processes and the spread of values reported in the literature. The resulting σ_i and σ_{prop} values for each sector are summarized in Table 4. Below, we describe the dominant contributors to σ_{prop}, ordered from highest to lowest sectoral uncertainty.

https://doi.org/10.5194/essd-2025-668
Preprint. Discussion started: 13 February 2026

- WET exhibits the largest propagated uncertainty ($\sigma_{\text{prop}} = 0.4$–$8.2‰$), directly inherited from the wide range of sub-sector values ($\sigma_i = 0.4$–$8.2‰$). The high variability reflects the influence of multiple environmental factors, including substrate type, methanogenic pathways (acetate fermentation vs. CO_2 reduction), and the $\delta^{13}C$ content of the organic matter (Ganesan et al., 2018; Oh et al., 2022).

- BB displays a propagated uncertainty of 0.5–6.0‰. This stems from the isotopic contrast between C_3 and C_4 vegetation: C_4 plants tend to produce more enriched $\delta^{13}C$-CH_4 during combustion. The range of σ_i (0.8–11.2‰) reflects differences in vegetation type across ecosystems and latitudes (Chanton et al., 2000; Brownlow et al., 2017; Menoud et al., 2022).

- NAT show a high sectoral uncertainty ($\sigma_{\text{prop}} = 2.0$–$5.4‰$), driven by the strong isotopic contrast for oceanic and termite sub-sectors. Both sub-sectors exhibit broad σ_i values (2.8–7.6‰), reflecting limited measurement coverage and substantial environmental dependency.

- FFG sources encompass oil, gas, coal, and geological seepage, each with distinct isotopic characteristics. The coal sub-sector, in particular, contributes significantly to the sector-level propagated uncertainty ($\sigma_{\text{prop}} = 1.1$–$5.2‰$) due to its high variability ($\sigma_i = 3.0$–$10.0‰$). The diversity in extraction technologies (e.g., conventional vs. unconventional gas), geological formations (e.g., shale vs. coalbed), temporal shift and regional practices leads to strong heterogeneity and uncertainty in fossil fuel signatures (Lan et al., 2021a; Menoud et al., 2022).

- AGW exhibits the lowest sectoral propagated uncertainty among the sectors ($\sigma_{\text{prop}} = 0.5$–$2.8‰$), despite moderate to high sub-sector variability ($\sigma_i = 0.2$–$6.6‰$). This is due to a flux-weighted balancing effect between well-characterized sources.

These propagated uncertainties from sub-sectors highlight the need for more systematic and representative measurements, particularly in under-sampled regions (e.g., tropics), and sectors (e.g. coal mines). Targeted field campaigns and isotopic monitoring networks could help reduce this uncertainty. Nonetheless, because of the inherent diversity and variability of methane formation processes, some degree of irreducible uncertainty must be accounted for and formally propagated in inversion frameworks (see Sect. 4.3.2).

Aggregation uncertainty (σ_{agg})

Aggregation is primarily required for computational efficiency in inversion frameworks (Sect.2.2). But, this necessary simplification introduces methodological uncertainty that must be explicitly quantified and propagated (Sect.2.3). The aggregation uncertainty, denoted σ_{agg}, represents the error introduced when multiple sub-sectors are combined into a single aggregated sector based on their respective emission fluxes. The corresponding values for each sector are reported in Table 4. Although this component is generally smaller and more stable than σ_{sub}, it increases for sectors that involve several formation pathways and isotopic fractionation, such as FFG (1.0‰) and AGW (1.7‰), where heterogeneous sub-sector compositions lead to significant propagation effects. These values illustrate that choices made in emission inventories, not only in flux magnitudes but also in source definitions and partitioning, can significantly shape sector-level isotopic signatures.

https://doi.org/10.5194/essd-2025-668
Preprint. Discussion started: 13 February 2026

Notably, discrepancies among major methane inventories, including EDGARv8 (Crippa et al., 2023), GAINSv4 (Höglund-Isaksson et al., 2020), CEDSv2021 (O'Rourke et al., 2021), and GFEIv2 (Scarpelli et al., 2022), contribute significantly to this aggregation uncertainty. For instance, for the FFG sector, the aggregation uncertainty is around 2.2% at the global scale, reflecting heterogeneity across inventories. Variability in emission factors and inventory methodologies, as described in Saunois et al. (2025), contribute strongly to this uncertainty. For example, oil and gas system emissions estimates vary considerably due to differences in emission factors and methodological assumptions across countries and inventories. Similarly, for the AGW sector, the aggregation uncertainty (2.8%) reflects differences in how fluxes are allocated among agriculture and waste-related sub-sectors across inventories. For example, manure emissions can be allocated either to the agriculture or to the waste category, which can shift the aggregated isotopic signature. On the contrary, for WET, no aggregation uncertainty is reported because this sector is not an aggregation of multiple subcategories. For NAT, since termite and ocean sources do not overlap geographically, the aggregation uncertainty is null.

Total uncertainty (σ_{total})

The total uncertainty, σ_{total}, represents the combined effect of sub-sector variability and aggregation uncertainty. The full range of uncertainty values per sector (σ_{total}) is reported in Table 4. This range corresponds to the spread of possible standard deviations (i.e. the uncertainty spread) rather than to a range of actual δ^{13}C–CH_4 signature values. This total uncertainty varies across sectors. For example, the BB and WET sectors exhibit wide uncertainty ranges, from 0.5 to 6.0‰ and from 0.4 to 8.2‰, respectively, primarily driven by sub-sector uncertainties. For the BB sector, the total uncertainty is largely driven by the sub-sector variability of biofuel burning. For WET, the large uncertainty is mainly due to the inherent spatial and seasonal variability of wetland emissions. The FFG and AGW sectors show total uncertainties of up to 5.3‰ and 3.3‰, respectively, which is consistent with their source diversity and complex sub-sector structures. NAT sources display lower average uncertainties overall.

The columns σ_{Menoud} (standard deviation within the dataset) and $\overline{\text{Uncertainty}}_{\text{Menoud}}$ (mean uncertainty) in Table 4 offer a comparison with extensive literature compilations (Menoud, 2022). Our total uncertainties are comparable to or smaller than these literature-based estimates, suggesting that the applied aggregation methodology provides a structured and quantitative framework for uncertainty propagation that complements broader bibliographic syntheses. However, the sub-sector uncertainties (σ_{prop}) used in our calculations are derived from the same dataset compiled by Menoud (2022). Therefore, σ_{prop} and σ_{total} are not fully independent from the comparison values in σ_{Menoud} and $\overline{\text{Uncertainty}}_{\text{Menoud}}$. The comparison is nonetheless informative as it illustrates how the literature-based source variability propagates through our aggregation scheme.

These sectoral uncertainties are subsequently propagated in our sensitivity simulations (see Sect. 3.2). They serve as a quantitative basis for defining the plausible variability ranges of source signatures, allowing us to assess their influence on modeled atmospheric δ^{13}C-CH_4 distributions. In atmospheric inversion frameworks, the total sectoral uncertainty (σ_{total}) can also be used to inform the specification of the prior error covariance matrix (B matrix) (see Sect. 4.3.2).

https://doi.org/10.5194/essd-2025-668
Preprint. Discussion started: 13 February 2026

Open Access Earth System Science Data Discussions

4.1.4 Comparison with δ^{13}C-CH_4 datasets from previous studies

Sector	Sub-sector	δ^{13}C-CH_4 This Study (‰, range)	Menoud et al. (2022) (‰, N)	Lan et al. (2021a) (‰, N or range)	Thanwerdas et al. (2024) (‰, range)
FFG	Coal	−43.7 [−44.5 / −43.3]	−50.7 (66)	−43.6 [−44.3 / −43.3]	−49.6 [−54.7 / −36.1]
	Oil & Gas	−44.0 [−44.1 / −43.8]	−44.5 (243)	−43.9 [−44.0 / −43.5]	−45.2 [−54.7 / −36.9]
	Geological sources	−46.6	N/A	−46.6*	−49.0
	Weighted mean	−44.2 [−44.6 / −43.9]			−45.2 [−54.7 / −36.1]
AGW	Livestock	−65.8 [−65.9 / −65.7]	−63.0 (43)	−65.8 [−65.9 / −65.7]	−63.6 [−66.8 / −60.8]
	Wastewater	−50.9	−50.9 (25)	−46.7 (1)	−48.0
	Landfills	−56.2	−56.2 (47)	−55.0 (10)	−52.0
	Agricultural waste	−54.9	−54.9 (28)	−57.8 (5)	−52.0
	Rice	−59.9	−59.9 (24)	−60.5 (20)	−63.0
	Weighted mean	−60.2 [−60.4 / −59.9]			−59.5 [−66.8 / −49.5]
BB	Biofuel burning	−24.3 [−24.5 / −24.0]	−22.7 (10)	−24.3 [−24.5 / −24.0]	−20.0
	Biomass burning	−24.2 [−25.1 / −23.1]	−26.1 (30)	−24.2 [−25.1 / −23.1]	−24.3 [−24.9 / −20.9]
	Weighted mean	−24.3 [−24.7 / −23.9]			−22.7 [−24.9 / −20.9]
WET	Wetlands	−58.6	−63.3 (108)	−58.6**	−60.9 [−74.9 / −50.0]
	Weighted mean	−58.6 [−58.6 / −58.6]			−60.9 [−74.9 / −50.0]
NAT	Termites	−63.4	−65.2 (7)	−63.4 (6)	−63.4
	Oceans	−42.0			−42.0
	Weighted mean	−51.9 [−51.9 / −51.9]			−45.5 [−63.0 / −42.0]

Table 5. Globally averaged δ^{13}C-CH_4 values (‰) for each source sector, weighted by methane flux over 1998–2022. Flux-weighted mean values were calculated using a consistent methane flux dataset across sectors and years (see Table 1), but only in cases where δ^{13}C-CH_4 signatures vary spatially or when aggregating sub-sectors. For literature datasets (e.g., Menoud et al. (2022); spatially fixed values for Lan et al. (2021a) and Thanwerdas et al. (2024)), the reported values correspond to simple arithmetic means and are not flux-weighted. Ranges in brackets indicate minimum and maximum of mean value over time. Numbers in parentheses denote the number of measurements used in the respective studies. * Value from Etiope et al. (2019). ** Value from Oh et al. (2022).

Table 5 presents a comparison between the updated δ^{13}C-CH_4 source signatures from this study and estimates reported by Menoud et al. (2022), Lan et al. (2021a), and Thanwerdas et al. (2024). The dataset from Menoud et al. (2022) is a compilation of δ^{13}C-CH_4 measurements from the literature, providing observation-based global mean signatures for major source sub-sectors. In contrast, both Lan et al. (2021a) and Thanwerdas et al. (2024) combine data compilations with gridded or model-

https://doi.org/10.5194/essd-2025-668
Preprint. Discussion started: 13 February 2026

derived products depending on the source sector, and also provide observation-based global mean signatures for major source sub-sectors. In our analysis, flux-weighted mean values were consistently applied across sectors and years when δ^{13}C-CH_4 signatures exhibit spatial variability or when aggregating sub-sectors. For literature datasets (i.e. Menoud et al. (2022), the spatially fixed values from Lan et al. (2021a) and Thanwerdas et al. (2024)), we used the reported mean values directly, which are not flux-weighted but correspond to simple arithmetic means.

For the FFG sector, our weighted mean signature is $-44.2‰$, which is generally consistent with Lan et al. (2021a) but slightly more enriched compared to Menoud et al. (2022) and Thanwerdas et al. (2024) whose values extend to more depleted ranges. Coal sources show greater differences, with our estimate around $-43.7‰$ compared to $-50.7‰$ in Menoud et al. (2022). This discrepancy can be explained by differences in data selection criteria and spatial weighting. Our estimate is derived using flux-weighted averaging that emphasizes high-emitting coal regions, particularly in China, where emissions tend to be less depleted than the global average (e.g., Wei et al., 2014; Qin et al., 2006; Sherwood et al., 2017; Lan et al., 2021a). In contrast, the value reported by Menoud et al. (2022) is an arithmetic mean of a broad compilation of site-level measurements, including more depleted coal emissions from regions with lower production or different geological contexts. The oil and gas isotopic signature is close to previous studies, with minor variation likely due to regional refinements. Geological emissions are fixed at $-46.6‰$, in line with the geochemical value from Etiope et al. (2019).

In the AGW sector, livestock methane isotopic values ($-65.8‰$) are more depleted than reported by Menoud et al. (2022) ($-63.0‰$) and Thanwerdas et al. (2024) ($-63.6‰$). This difference likely stems from our use of the spatially explicit source signature maps from Lan et al. (2021a), which account for regional differences in C_3/C_4 feed composition using global maps of biomass C_3/C_4 ratios (Randerson et al., 2012; Still et al., 2003). Flux-weighted averaging based on these maps emphasizes regions dominated by C_3 vegetation, such as temperate zones, resulting in more depleted signatures. Our estimate is also consistent with the $-64.9‰$ value reported for 2012 by Chang et al. (2019). Waste-related emissions, including landfill, wastewater, and agricultural waste, are updated following Menoud et al. (2022), resulting in relatively values: $-50.9‰$ for wastewater, $-56.2‰$ for landfill, and $-54.9‰$ for agricultural waste. This increase is attributed to changes in waste management practices, notably increased biogas production, which tends to leak methane with relatively higher δ^{13}C (Menoud et al., 2022). Rice emissions, also from Menoud et al. (2022), are set at $-59.9‰$, slightly more enriched than the $-63.0‰$ used in Thanwerdas et al. (2024) due to differences in the amount of compiled litterature.

For BB, our weighted mean of $-24.3‰$ from Lan et al. (2021a) matches closely the value from Thanwerdas et al. (2024), while being slightly more depleted than in Menoud et al. (2022). WET signatures, derived largely from Oh et al. (2022), have a weighted mean of $-58.6‰$, slightly enriched compared to Menoud et al. (2022) ($-63.3‰$) and consistent with Lan et al. (2021a). Natural sources (NAT) retain previous estimates, with termites at $-63.4‰$ and oceans at $-42.0‰$, reflecting values from Lan et al. (2021a) and Thanwerdas et al. (2024). The weighted mean of $-51.9‰$ accounts for the relative contribution of these sources.

For termites, we adopted a value of $-63.4‰$, consistent with Lan et al. (2021a) and Thanwerdas et al. (2024). The depleted signature of $-76.1‰$ reported by Sugimoto et al. (1998) was not used here due to concerns about potential outliers. This choice

https://doi.org/10.5194/essd-2025-668
Preprint. Discussion started: 13 February 2026

explains the discrepancy with the more depleted mean of Menoud et al. (2022), who included the Sugimoto et al. (1998) value in their compilation.

Generally, the updated δ^{13}C-CH_4 source signature maps show clear sectoral and regional patterns, with depleted signatures for wetlands and agriculture, and enriched signatures for fossil fuel and biomass burning emissions. Temporal variations are limited over the study period, except in sectors where emissions were known to vary in time. Uncertainty analysis highlights significant variability, particularly for the agriculture and waste sector. The updated maps are broadly consistent with recent datasets. In the next section, we assess how the uncertainties over inputs propagate to the modeled atmospheric δ^{13}C-CH_4 signal through sensitivity simulations.

4.2 Sensitivity of simulated atmospheric δ^{13}C-CH_4 signal and CH_4 mole fractions to key parameters

Forward atmospheric simulations provide a framework for assessing the impact of source signature uncertainties on modeled δ^{13}C-CH_4 (see Sect. 3.1). By testing several sets of key input parameters (see Sect. 3.2), we can identify which sources of uncertainty have the strongest influence on the atmospheric isotopic signal. This approach, and the way input and output uncertainties are propagated within the inversion framework, is illustrated in Fig. 3. In this section, we evaluate the sensitivity of simulated atmospheric CH_4 mole fractions and δ^{13}C-CH_4 isotopic signals at the surface, where observations are available, to key parameters, including emission inventories for aggregation (Sect. 4.2.1), fluxes (Sect. 4.2.2), chemical reactions (Sect. 4.2.3), and source signatures (Sect. 4.2.4). Table 6 provides a comparative overview of the sensitivities, allowing a quick identification of which parameters most influence the modeled CH_4 mole fractions and isotopic signals. Detailed results and interpretations are provided in the following sub-sections.

https://doi.org/10.5194/essd-2025-668
Preprint. Discussion started: 13 February 2026

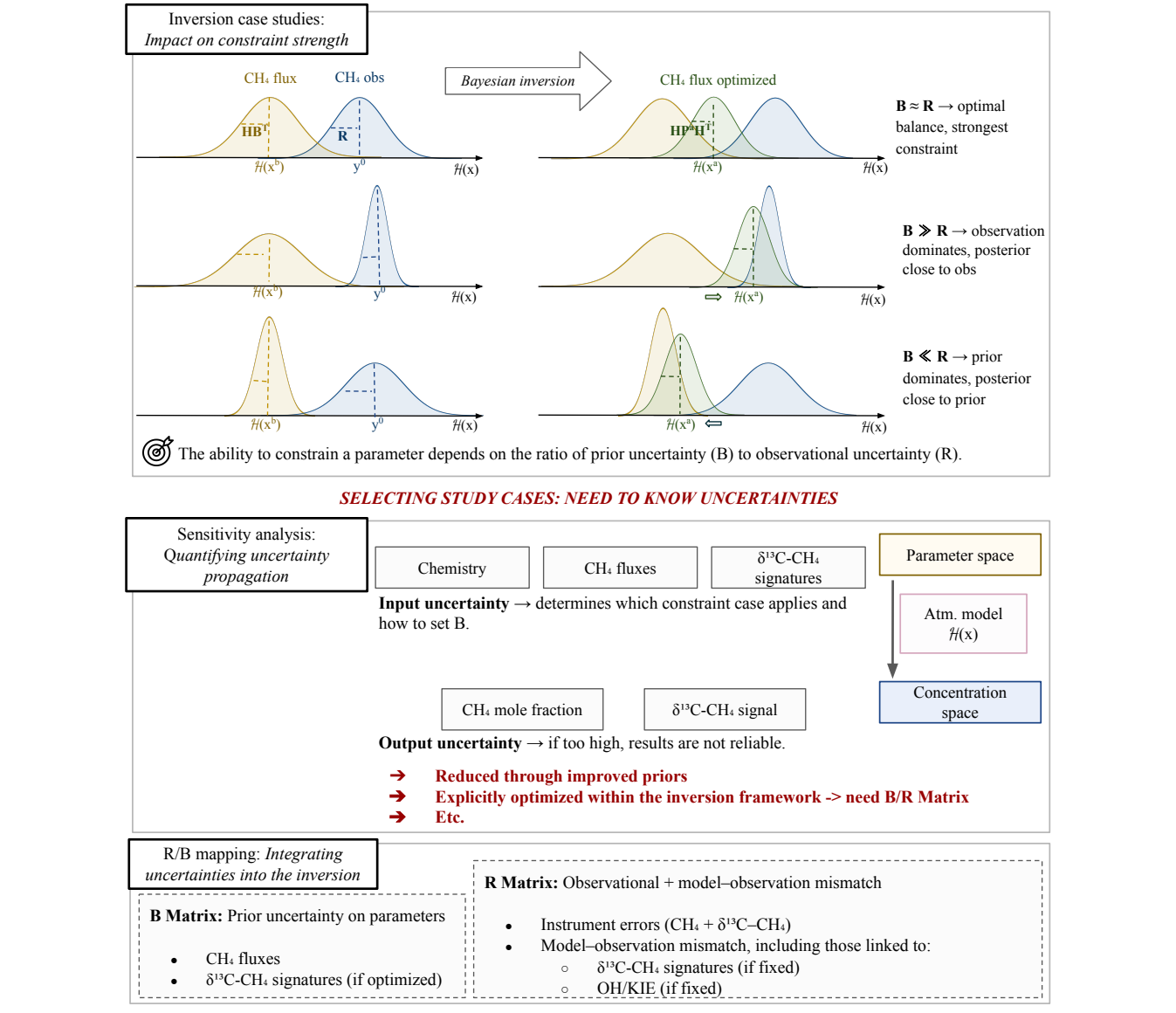

Figure 3. In the upper panel, coloured Gaussian curves (yellow: prior, blue: observation, green: posterior) illustrate how the ratio between B (prior error covariance matrix) and R (observation error covariance matrix) determines the strength of the inversion constraint: (i) when B ≈ R, the optimal balance yields the strongest constraint; (ii) when B ≫ R, observations dominate and the posterior approaches the observations; (iii) when B ≪ R, the prior dominates and the posterior remains close to the prior. The middle panel conceptually shows how uncertainties are quantified in the sensitivity framework. Input uncertainties determine which constraint case applies and how to set B in the parameter space, which is mapped into the concentration space by the atmospheric model operator H(x). Output uncertainties indicate the reliability of the inversion results; if too high, results are not robust. They can be reduced through improved priors or explicitly optimized within the inversion framework. The bottom panel summarises how these uncertainties are formalised within the B matrix and the R matrix.

https://doi.org/10.5194/essd-2025-668
Preprint. Discussion started: 13 February 2026

Open Access Earth System Science Data Discussions

Table 6. Summary of the sensitivity of modeled CH_4 mole fraction and $\delta^{13}C$–CH_4 signal to key parameters at surface level over 2016–2020. Values are given as relative and absolute standard deviations (first and second number in each cell, respectively).

Category	Sensitivity of CH_4	Sensitivity of δ^{13}C-CH_4
Flux aggregation	0.1% / 5.6 ppb	0.3% / 0.06‰
Fluxes		
Wetland fluxes	1.7% / 25.2 ppb	0.9% / 0.18‰
Freshwater fluxes	1.4% / 67.8 ppb	0.9% / 0.21‰
Anthropogenic fluxes	2.4% / 30.1 ppb	1.6% / 0.29‰
Chemistry		
OH fields	3.6% / 49.6 ppb	0.0% / 0.02‰
OH Kinetic Isotope Effect (KIE)	0.0% / 0.0 ppb	2.2% / 0.40‰
Source signature		
Fossil Fuel and Geological (FFG)	0.0% / 0.0 ppb	0.4% / 0.04‰
Agriculture and Waste (AGW)	0.0% / 0.0 ppb	1.7% / 0.32‰
Biomass Burning (BB)	0.0% / 0.0 ppb	0.8% / 0.16‰
Natural Sources (NAT)	0.0% / 0.0 ppb	0.4% / 0.07‰
Wetlands (WET)	0.0% / 0.0 ppb	0.1% / 0.02‰

4.2.1 Sensitivity to fluxes used for aggregation

Figure 4 summarizes the sensitivity of flux aggregation to different prior datasets. Panel (a) shows the variability of flux estimates between inventories, highlighting where emission fluxes are most uncertain. Since this test focuses specifically on uncertainties arising from the flux-weighted aggregation of isotopic signatures, only anthropogenic sectors (FFG, AGW and BB) are included (see Sect. 3.2). Panel (b) presents the resulting variability in the aggregated δ^{13}C-CH_4 source signatures by sector. Panel (c) shows the sensitivity of simulated atmospheric δ^{13}C-CH_4 signals to these aggregated isotopic changes at surface level. It is important to note that panel (c) displays a single sensitivity map representing the combined impact of flux-weighted isotopic signatures variations across all anthropogenic sectors on isotopic signal simulated at the surface. Because only isotopic signatures are perturbed while the underlying emission fluxes remain unchanged, this test does not directly affect CH_4 mole fractions. The only noticeable effect on CH_4 mole fractions occurs in the "NO_AGGREG" setup, in which the number of aggregated source categories was increased from 5 to 14 to evaluate the impact of the trade-offs between computational efficiency and isotopic detail (see Sect. 3.2), resulting in a very small change in simulated CH_4 mole fractions (about 5.6 ppb on average; Table 6). Figure S3 shows the same information as in Fig. 4 but expressed in terms of relative standard deviation (RSD). Together, these results illustrate how inventory discrepancies propagate through to atmospheric simulations of δ^{13}C-CH_4 signal.

https://doi.org/10.5194/essd-2025-668
Preprint. Discussion started: 13 February 2026

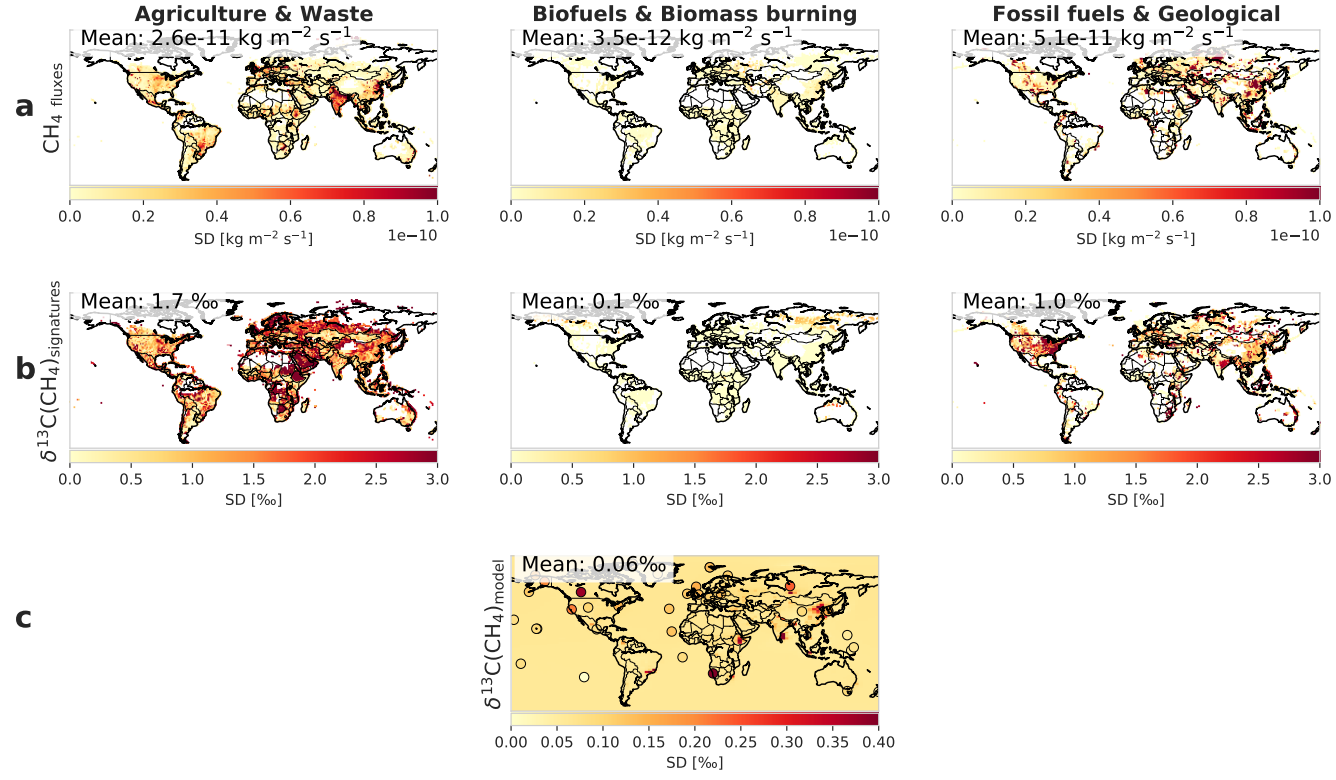

Figure 4. (a) SD (in kg .m^{-2} .s^{-1}) of the fluxes among different prior datasets (GAINSv4, CEDSv2021, GFEIv2, EDGARv8) (over 2016–2020) at surface level. Values are only displayed when the associated CH_4 flux is higher than 0.2 mgCH_4·m^{-2}·day^{-1}, for aggregated categories. (b) SD in ‰ of the δ^{13}C-CH_4 source signature by aggregated category at surface level. (c) SD in ‰ of the δ^{13}C-CH_4 signals from the forward model outputs at surface level. Coloured circles indicate SD of observed δ^{13}C-CH_4 values at each surface station over the study period (Michel et al., 2024; Schuldt et al., 2025).

The largest flux uncertainties (Figure S3a) are observed in the Fossil Fuels & Geological (FFG) and Agriculture & Waste (AGW) sectors (65% and 41% respectively). These uncertainties stem from differences between inventories, which exhibit regional discrepancies. For example, in Central Asia (Turkmenistan, Afghanistan, Uzbekistan), there are significant differences in fossil fuel emission estimates. In Turkmenistan, GAINS estimates 1259 kt CH_4 yr^{-1}, while EDGARv8 and CEDS report 1343 and 1351 kt CH_4 yr^{-1} respectively and GFEI 888 kt CH_4 yr^{-1}. Although totals appear similar, the spatial allocation and sectoral breakdown differ markedly between inventories. This is partly because inventories rely on national reports submitted to the UNFCCC, ensuring consistency at the country level but not necessarily in spatial detail or sub-sector attribution. Additionally, satellite-based studies (e.g., Vanselow et al., 2024) have identified emission events in regions such as Turkmenistan, associated with fossil fuel infrastructure. However, such episodic or localized emissions are generally not included in bottom-up inventories, which may underestimate the true emission rates. In the AGW sector, a high RSD is observed in Botswana.

https://doi.org/10.5194/essd-2025-668
Preprint. Discussion started: 13 February 2026

This is linked to the aggregation structure in GAINS, where large African regions are aggreggated, whereas other inventories provide country-level estimates.

The impact of these flux uncertainties on δ^{13}C-CH_4 source signatures (Figure 4b) is especially pronounced in the AGW sector, which shows the highest isotopic sensitivity (1.7‰), particularly in the Middle East and parts of Africa. This is related to the relative contributions of sub-sectors with distinct isotopic signatures, such as livestock (more depleted) and waste (less depleted), as defined in the inventories. For instance, in Ethiopia (2016 – 2020), livestock accounts for 79% of AGW emissions in CEDS and GAINS, but only 67% in EDGARv8, which is reflected in the region's isotopic signature variability. In contrast, the FFG sector shows lower isotopic sensitivity despite higher flux uncertainties (2.2%). This is explained by the more homogeneous isotopic signatures of coal, oil and gas and geological, and the smaller relative isotopic differences among sub-sectors. The uncertainties are highest in North America, they are mainly associated with the difference in relative contribution of oil and gas versus coal in the datasets. The variability in Chinese coal emissions is also well documented, with CEDS based on EDGARv4.2 previously overestimating emissions compared to recent regional inventories (Liu et al., 2021; Saunois et al., 2025). These results highlight the key role of emission partitioning within aggregated categories in shaping the final isotopic source signature, particularly in the AGW sector. These uncertainty values are used to define the σ_{agg} parameter in the uncertainty analysis (see Section 4.1.3).

The sensitivity of simulated atmospheric δ^{13}C-CH_4 signals to aggregation choices remains globally low, with a mean RSD of 0.32% (Figure S3c) and a mean SD of approximately 0.06‰ (Figure 4c). This suggests that, despite regional discrepancies, aggregation uncertainties have a limited impact on large-scale atmospheric isotopic patterns. Moreover, the values shown in Figure S3c represent relative sensitivities computed over the entire model domain, which tends to dilute localized sensitivity hotspots. When compared to the RSD of observed δ^{13}C-CH_4 values at surface stations (e.g., Michel et al., 2024; Schuldt et al., 2025), the simulated sensitivities is smaller. This indicates that real-world atmospheric variability exceeds the response induced by inventory-driven aggregation uncertainties, and further support the limited impact of this specific error source on the modelisation of the atmospheric isotopic signal at observational sites (more details in Section 4.3).

4.2.2 Sensitivity to uncertainties in methane fluxes from wetlands, freshwaters, and anthropogenic sectors

Figure 5 summarizes the sensitivity of atmospheric simulations to uncertainties in methane flux estimates from key source sectors: wetlands, freshwaters, and the total anthropogenic emissions (i.e. the sum of all anthropogenic sources). Unlike the previous section, where only isotopic signatures were perturbed through flux-weighted aggregation, here the underlying emission fluxes themselves are varied in the model simulations. Panel (a) shows the SD of CH_4 emissions across inventories, and highlight where flux uncertainties are the greatest. For a detailed breakdown of anthropogenic subsectors (e.g., fossil fuels, waste, agriculture), refer to supplementary Figures S5 and S6, which show their individual contributions. Panels (c) and (e) display the impact of uncertainties in wetlands, freshwaters, and anthropogenics fluxes on modeled CH_4 mole fractions and δ^{13}C-CH_4 signals, respectively, at surface level. Figure S4 shows the same information in terms of RSD. Theses figures show how uncertainties in sectoral emissions propagate into atmospheric simulations.

https://doi.org/10.5194/essd-2025-668
Preprint. Discussion started: 13 February 2026

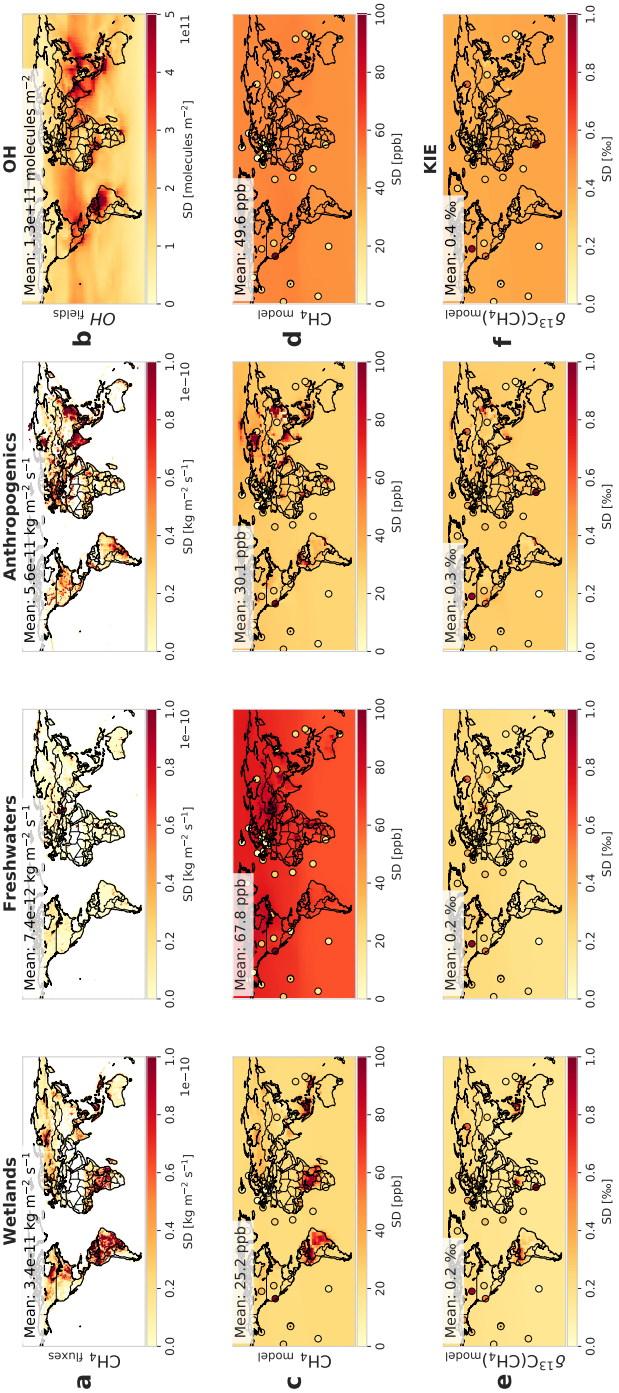

Figure 5. Standard deviation (SD) over 2016–2020. (a) SD (in kg .m^{-2} .s^{-1}) of CH_4 emissions from wetlands, freshwaters, and anthropogenic sectors (AGW, FFG, BB) at surface level. Values are only displayed when the associated CH_4 flux exceeds 0.2 mg $CH_4 \cdot m^{-2} \cdot day^{-1}$. (b) SD (in molec .$m^{-2}$) of the total tropospheric OH column (pressure levels below 250 hPa). (c) SD (in ppb) of CH_4 mole fractions at surface level from forward model outputs, driven by uncertainty in emission fluxes. Coloured circles indicate RSD of observed CH_4 mole fractions at surface stations with co-located $\delta^{13}C(CH_4)$ measurements. (d) Same as (c), but driven by uncertainty in OH fields. (e) SD (in ‰) of $\delta^{13}C\text{-}CH_4$ values at surface level from forward model outputs, driven by uncertainty in emission fluxes. Coloured circles indicate RSD of observed $\delta^{13}C\text{-}CH_4$ values at the same stations (Michel et al., 2024; Schuldt et al., 2025). (f) Same as (e), but driven by uncertainty in kinetic isotope effects (KIE) during CH_4 oxidation.

https://doi.org/10.5194/essd-2025-668
Preprint. Discussion started: 13 February 2026

Methane flux uncertainties are highest for anthropogenic sources (mean RSD of 129%), followed by wetlands (96%) and freshwaters (22%) (Figure S4a). These differences arise from inventory discrepancies, the inherent complexity of methane emission processes (e.g., large spatio-temporal variability, dependence on environmental conditions and management practices), and the uneven availability of observational data across regions and sectors, which limits the capacity to constrain emissions. Among anthropogenic subsectors, fossil fuels exhibit the largest uncertainty (RSD 83.8%, Figure S5), driven by inconsistent national reporting, the use of variable emission factors, and the presence of poorly constrained super-emitters (Lauvaux et al., 2022; Saunois et al., 2025). Waste emissions follow (RSD 51.9%), and include landfills, agricultural waste, and wastewater. The limited spread across inventories for landfills is mostly due to the use of similar Tier 1 methods and data sources, not better emission constraints. Substantial uncertainties persist due to variations in emissions arising from different climate conditions, landfill management practices, and the inherent temporal and geographical variability of landfill emissions (Wang et al., 2023; Krautwurst et al., 2017; Nisbet et al., 2019; Bourn et al., 2019). Wastewater emissions remain particularly uncertain due to variability in treatment processes and limited measurements (Saunois et al., 2025). Biofuel burning shows a high RSD (55.7%) but low absolute impact due to its smaller flux. Agriculture (RSD 42.2%) contributes significantly in absolute terms due to its large emissions. Regarding natural sources, wetland emission uncertainties stem from multiple factors: inconsistent wetland extent maps (Melton et al., 2013; Bohn et al., 2015), uncertainties in methane production and oxidation modeling (Knox et al., 2021), and the influence of environmental drivers such as temperature and water table depth (Tian et al., 2010; Poulter et al., 2017). The dominant source of long-term uncertainty is wetland areal extent (Poulter et al., 2017; Karlson and Bastviken, 2023), while seasonal variability is primarily driven by meteorology (Parker et al., 2022; McNicol et al., 2023). Tropical wetlands remain particularly uncertain due to sparse data coverage despite their importance for global feedbacks (Nisbet, 2023; Zhang et al., 2023; France et al., 2022). Freshwater emissions are also uncertain due to poorly mapped inland waters, complex seasonal dynamics, and diverse emission pathways (e.g., diffusion, ebullition, plant-mediated transport) (Van Bergen et al., 2019; Lauerwald et al., 2023; Saunois et al., 2025). However, as only one freshwater dataset was available the sensitivity shown here reflects the introduction of freshwater emissions into the simulation (ON/OFF comparison) rather than a quantified uncertainty across multiple estimates.

Panel (c) of Figure 5 shows how flux uncertainties propagate into modeled CH_4 mole fractions. The strongest sensitivity is linked to freshwater emissions, with an average variability of 68 ppb (4.4%). This reflects a significant contribution to total methane emissions (+53 Tg CH_4 yr^{-1}) and strong regional impacts, particularly near the Caspian Sea, where freshwater sources dominate and where no wetland or oceanic fluxes were present in the reference simulation, thus amplifying the local sensitivity (Figure S2). Anthropogenic fluxes contribute to a variability of 30 ppb (2.4%), especially in major fossil fuel production regions such as Siberia and industrialized areas like Eastern China. Wetland fluxes result in a variability of 25 ppb (1.7%), concentrated in high-emission regions such as the Amazon, Southeast Asia, and the Congo Basin.

Similarly, modeled δ^{13}C-CH_4 signals (panel e) show a spatial pattern that mirrors CH_4 mole fraction sensitivity. Wetland and freshwater flux uncertainties both lead to an average isotopic variability of 0.2‰ (0.9%), while anthropogenic fluxes cause 0.3‰ (1.6%). These findings emphasize that sectoral flux uncertainties substantially influence regional isotopic signal, particularly in areas with high methane emissions.

https://doi.org/10.5194/essd-2025-668
Preprint. Discussion started: 13 February 2026

Observed SDs from surface monitoring sites (shown as colored circles) are also displayed in panels (c) and (e) for comparison. In several cases, modeled isotopic sensitivities exceed the observed SD, especially for freshwater, induced CH_4 variability, highlighting their relevance for inversion performance (see Sect. 4.3.2). As illustrated in panels (c) and (e), the maps convey two layers of information: regional hotspots where large uncertainties may hamper local flux attribution (e.g., Caspian region, Chinese industrial basins, Congo wetlands, etc.), and background sensitivity over well-mixed or remote areas, which are critical for constraining hemispheric to global budgets. This distinction is further discussed in Sect. 4.3.2.

4.2.3 Sensitivity to atmospheric chemistry parameters

Figure 5 also illustrates the uncertainties related to atmospheric chemistry parameters, focusing mainly on the kinetic isotope effect (KIE) of methane oxidation by tropospheric hydroxyl radicals (OH), which are the primary oxidant of methane. Panel (b) presents the SD of the total tropospheric OH column (pressure levels below 250 hPa), highlighting regions with the largest OH uncertainties. Panel (d) shows how these uncertainties affect modeled CH_4 mole fractions at surface level. Panel (f) displays how uncertainty over KIE impacts atmospheric δ^{13}C-CH_4 signals. OH uncertainty does not affect δ^{13}C-CH_4 signal, and OH-KIE does not impact CH_4 mole fractions. Figure S4 shows the same information in terms of RSD.

Uncertainties in OH fields (Figure 5b and Figure S4b) are substantial (e.g., Nicely et al., 2017; Collins et al., 2017; Zhao et al., 2019; Stevenson et al., 2020). SD are particularly high over tropical continental regions such as Amazonia, South Asia, and the African savannas, where OH concentrations peak due to intense photochemistry and high humidity and where strong inter-model differences coexist (Zhao et al., 2019). These areas are also subject to highly variable and poorly constrained emissions of OH precursors, including biogenic VOCs, biomass burning, and soil NO_x which contribute to large inter-model range (Zhao et al., 2019; Saunois et al., 2025).

The sensitivity of simulated CH_4 mole fractions to OH variability (Figure 5d) is relatively uniform globally, with an average SD of 49.6 ppb (RSD of 3.6%). This confirms that the oxidative sink is a dominant factor controlling methane concentrations and that its uncertainties propagate broadly rather than being confined to specific regions. While OH-related uncertainties propagate globally and uniformly, their impact near source regions appears limited (Figure 5d). This is particularly relevant given ongoing concerns about CH_4–OH interactions in polluted areas, where local nonlinearities may arise due to complex dependencies of OH concentrations on emissions of NO_x, CO, and volatile organic compounds (VOCs) (Lin et al., 1988; Guthrie, 1989; Holmes et al., 2013; Lelieveld et al., 2016; Gaubert et al., 2017). In theory, elevated CH_4 concentrations could partially saturate the OH sink, especially in regions with high levels of co-emitted VOCs and NO_x that alter oxidative capacity. However, this expected nonlinearity is not strongly expressed in the CH_4 sensitivity maps. Because OH concentrations are prescribed and do not respond to CH_4 levels in our configuration, the oxidative capacity is higher than it would be under interactive chemistry. This conservative setup further dampens any potential CH_4–OH saturation effects, explaining the relatively uniform CH_4 sensitivity patterns shown in Figure 5d. Moreover, the SD induced by OH variability exceeds the observed SD of CH_4 mole fractions at most monitoring sites, indicating that OH-related uncertainties alone can introduce model variability greater than observational noise.

https://doi.org/10.5194/essd-2025-668
Preprint. Discussion started: 13 February 2026

Regarding the kinetic isotope effect, Figure 5f and Figure S4f show that uncertainties in the OH-KIE induce a geographically homogeneous SD of 0.4 ‰ (RSD of 2.2%) in the atmospheric δ^{13}C-CH_4 signal (Michel et al., 2024; Schuldt et al., 2025). Importantly, this 0.4‰ SD exceeds the observed SD of atmospheric δ^{13}C-CH_4 at surface stations Schuldt et al., 2025, highlighting that OH-KIE uncertainties can dominate over measurement variability and must therefore be accurately represented in inversion frameworks (see Sect. 4.3.2).

4.2.4 Sensitivity of simulated atmospheric δ^{13}C-CH_4 to source signatures

Figure 6 and Figure S7 present the sensitivity of the simulated atmospheric δ^{13}C-CH_4 signal to uncertainties in source-specific isotopic signatures, based on the Monte Carlo simulations (see Sect. 3.2). Panel (a) displays the SD of the prescribed δ^{13}C-CH_4 source signatures used as input to the simulations. The highest signature RSDs are associated with the BB sector, with an RSD of 36 % and a SD of 7.8 ‰, followed by FFG sector (RSD: 13.0 %, SD: 6.1 ‰), NAT sector (RSD: 12.0 %, SD: 5.3 ‰), WET sector (RSD: 9.2 %, SD: 5.2 ‰), and AGW sector (RSD: 7.3 %, SD: 4.6 ‰). These RSD values are consistent with the sector-specific uncertainty ranges summarized in Table S3. The spatial pattern of these uncertainties reflects the regional sampling domains used in the Monte Carlo parameterization (see Sect. 3.2).

Panel (b) shows the resulting variability in modeled atmospheric δ^{13}C-CH_4 at surface level. These simulations only perturb the isotopic composition of the emissions while keeping total CH_4 fluxes fixed, as a result, there is no corresponding effect on CH_4 mole fractions. Despite having a comparatively lower SD in its source signature, the AGW sector emerges as the dominant driver of atmospheric δ^{13}C-CH_4 uncertainty, with a mean sensitivity of 0.32‰ (1.74%). This impact is particularly pronounced in regions with high AGW emissions, such as India, where EDGARv8 estimates an annual mean emission of 26 Tg CH_4 per year over the period 2016–2020. Other sectors contribute less significantly to overall isotopic variability but still have regionally relevant effects: BB contributes 0.16‰ (0.84%), FFG 0.04‰ (0.43%), NAT (NAT) 0.07‰ (0.38%), and WET 0.02‰ (0.10%).

In summary, uncertainties in source-specific isotopic signatures, particularly from AGW sector, translate into substantial variability in the simulated δ^{13}C-CH_4 signal. This effect is especially pronounced in emission hotspots, where even small shifts in isotopic assumptions can significantly affect local atmospheric signals. Conversely, background regions remain sensitive to these uncertainties through long-range transport, potentially biasing hemispheric or global source attribution. Moreover, the mean RSD induced by AGW source signature uncertainties (1.74%) exceeds the observed RSD of δ^{13}C-CH_4 at most surface stations, suggesting that this parameter is a major limiting factor for isotopic inversions. For other sectors (e.g., BB, FFG, NAT), the simulated RSD remains generally closer to or below observed values, depending on the station location and the local sensitivity to each source's isotopic signature. These findings underscore the need to improve isotopic characterization of agricultural and waste-related methane sources, especially in hotspots regions. Implications for the design and configuration of such systems are discussed in Sect. 4.3.2.

Our sensitivity analysis shows that uncertainties in the OH kinetic isotope effect (KIE) are the dominant drivers of variability in the modeled δ^{13}C-CH_4 signal at global scale. Uncertainties in agriculture and waste sector source signatures and fluxes also

https://doi.org/10.5194/essd-2025-668
Preprint. Discussion started: 13 February 2026

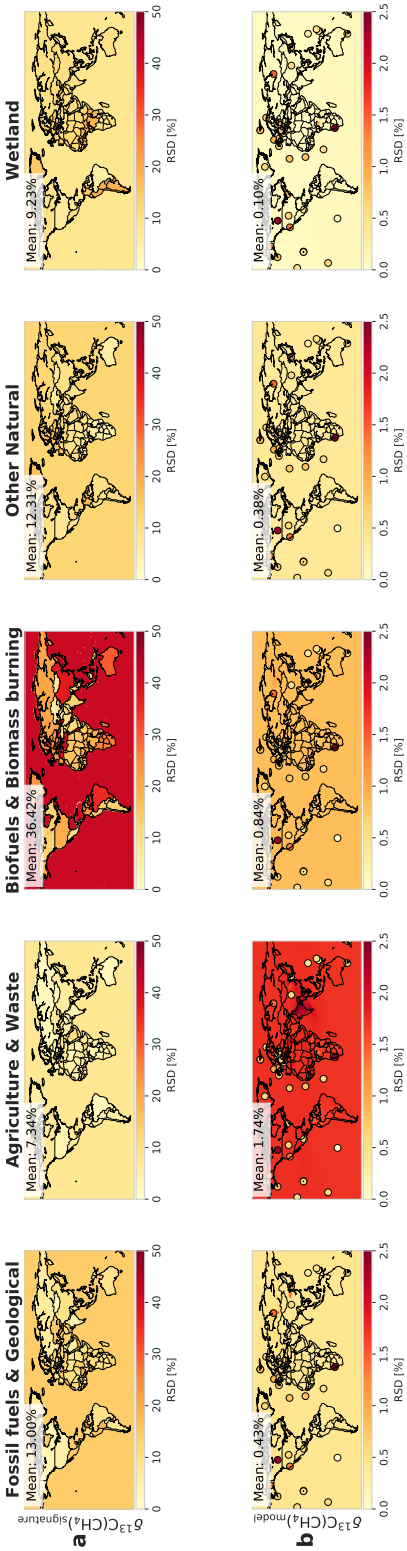

Figure 6. (a) SD (in permil) of the δ^{13}C-CH_4 source signature sensitivities inputs for Monte Carlo simulations, by sector at surface level. (b) SD of the δ^{13}C-CH_4 source signal from Monte Carlo simulations, by sector at surface level. Coloured circles indicate RSD of observed δ^{13}C-CH_4 values at each surface station over the study period (Michel et al., 2024; Schuldt et al., 2025).

https://doi.org/10.5194/essd-2025-668
Preprint. Discussion started: 13 February 2026

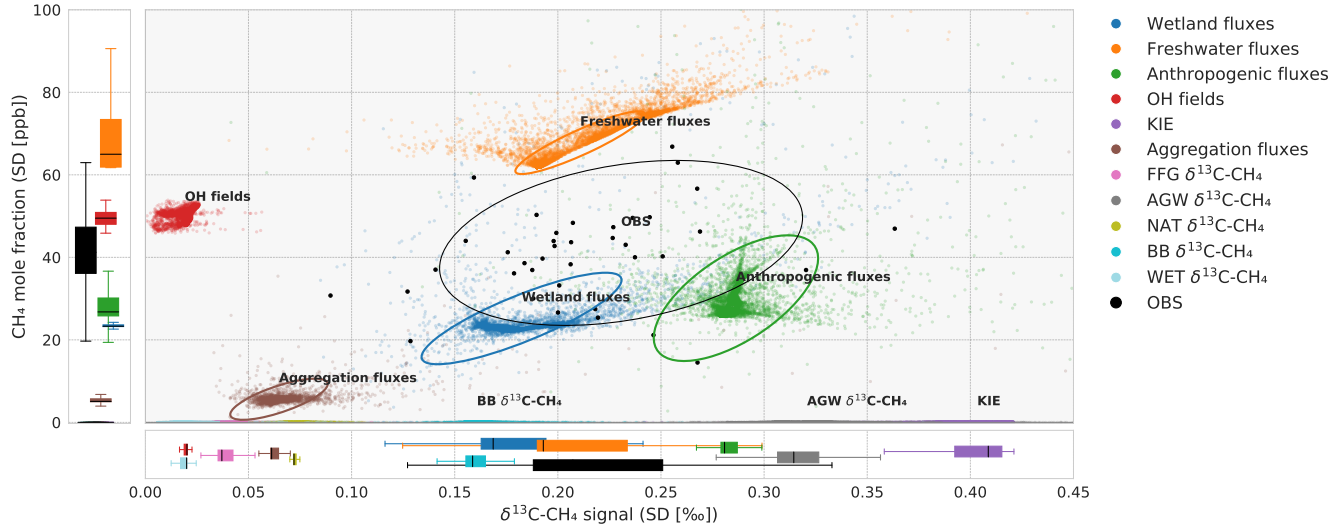

Figure 7. Uncertainties in CH_4 mole fraction and the δ^{13}C-CH_4 isotopic signal across various parameters. The x-axis shows the SD of CH_4 mole fractions in parts per billion (ppb), while the y-axis shows the SD of the δ^{13}C-CH_4 signal in per mil (‰). Each point represents a simulated grid cell, and the point labeled *OBS* corresponds to observations from a surface monitoring station. Parameters located in the upper-right quadrant induce the largest uncertainties in both mole fraction and isotopic composition.

contribute significantly. In contrast, uncertainties associated with fossil fuel and wetland source signatures, as well as those related to fluxes used for aggregation, have a more limited impact at the global level (more details in Sect 4.3.1).

4.3 Discussion

This section discusses the key outcomes of the sensitivity analysis (Sect. 4.3.1) and their implications for atmospheric methane inversions (Sect. 4.3.2). We examine how the sensitivity analysis results can inform the configuration of isotopic inversions, particularly regarding uncertainty specification and parameter prioritization. The main objective is to distinguish between uncertainty components that could be reduced through improved input data or model structure, and those that are intrinsic and must be explicitly optimized within the inversion framework (see Figure 3). Finally, we identify opportunities for future improvements, both within inversion systems and through supporting efforts such as inventories, field campaigns, and process-based models (Sect. 4.3.3).

4.3.1 Key uncertainty drivers affecting CH_4 and δ^{13}C-CH_4 simulations

This sensitivity analysis identifies and quantifies the primary contributors to uncertainties in both CH_4 mole fractions and atmospheric δ^{13}C-CH_4 isotopic signals. Figure 7 synthesizes the uncertainty patterns presented in Sections 4.2.1 to 4.2.4. It shows, for each sensitivity experiment, the standard deviation of CH_4 mole fractions (x-axis) and of δ^{13}C-CH_4 isotopic signals (y-axis) across all grid cells. Parameters located in the upper-right quadrant induce the largest uncertainties in both mole fractions

https://doi.org/10.5194/essd-2025-668
Preprint. Discussion started: 13 February 2026

and isotopic signals, indicating that these parameters are critical targets for model improvement. The figure also includes the observational uncertainty range (OBS), allowing direct comparison between model sensitivity and measurement standard deviation. This comparison provides a reference to assess whether model sensitivities exceed observational uncertainties, which influences the ability to extract useful information from atmospheric observations. More detailed implications for inversion frameworks are discussed in the following section.

The largest contributor to CH_4 mole fraction uncertainty is the freshwater fluxes, a source historically excluded from top-down inversions due to the lack of global spatially explicit priors (e.g., Saunois et al., 2020). Recent developments, however, now allow the inclusion of gridded freshwater emission estimates (Lauerwald et al., 2023). This influence is particularly significant over the Caspian Sea region. Following freshwater fluxes, uncertainties in OH concentrations represent the second-largest impact on methane variability, consistent with earlier studies (Basu et al., 2022). In contrast, the atmospheric δ^{13}C-CH_4 signal is primarily sensitive to uncertainties in the OH-KIE, confirming the central role of isotopic fractionation during CH_4 oxidation. This is consistent with Basu et al. (2022), who identified OH-KIE as a primary source of uncertainty in partitioning fossil versus microbial methane sources, and with Chandra et al. (2024), who demonstrated that OH-KIE strongly influences the magnitude of the atmospheric δ^{13}C-CH_4 signal but has limited impact on the long-term trend of methane mole fractions. Our analysis further quantifies the impact of interannual variability in OH fields, wetland emissions, freshwater emissions, and isotopic source signatures, highlighting additional sources of uncertainty relevant to isotopic inversions. The second-largest contributor to isotopic uncertainty is the source signature of agriculture and waste emissions, which induces strong regional effects, particularly over India. Freshwater and wetland fluxes also significantly contribute to isotopic variability, while uncertainties in fossil fuel and biomass burning source signatures appear to have a more limited impact. The uncertainty linked to flux aggregation choices has a minor influence on δ^{13}C-CH_4 (0.06 ‰). This result supports the transferability of the isotopic maps provided in this study across a wide range of inversion setups and emission inventories.

While not directly comparable, the standard deviations from our sensitivity tests provide insight into the scale of potential errors relative to observed trends. For example, uncertainties reaching 68 ppb in some configurations could impact multi-year trend interpretations, when the observed growth rate is around 9.4 ± 0.3 ppb yr^{-1} over 2016–2020 (Lan et al., 2025). Similarly, for δ^{13}C-CH_4, the uncertainties quantified here are non-negligible relative to the observed long-term trend of approximately -0.04‰ yr^{-1} (Schuldt et al., 2024).A more relevant comparison is with the standard deviation of atmospheric observations (Figure S8). Comparing these uncertainties to the SD of atmospheric observations provides context by situating parameter uncertainty magnitudes relative to the natural variability and measurement noise of the observations. The observed SD of atmospheric CH_4 mixing ratios is 44 ppb, indicating that uncertainties associated with parameters such as OH concentrations and freshwater emissions, with SDs exceeding this threshold, are critical contributors to model variability. For δ^{13}C-CH_4, the observed SD is 0.23 ‰, and key sources of uncertainty, including OH-KIE, anthropogenic source signatures, and wetland fluxes, exhibit SDs of similar or greater magnitude.

Figure 8 illustrates the spatial distribution of the dominant source of uncertainty in each grid cell. To complement this spatial classification, Figure S8 and Figure S9 provide a detailed quantification of the contribution of each parameter to the total variance of the simulated δ^{13}C-CH_4 signal and CH_4 mole fraction, at the model grid cell level. It enables a direct comparison

https://doi.org/10.5194/essd-2025-668
Preprint. Discussion started: 13 February 2026

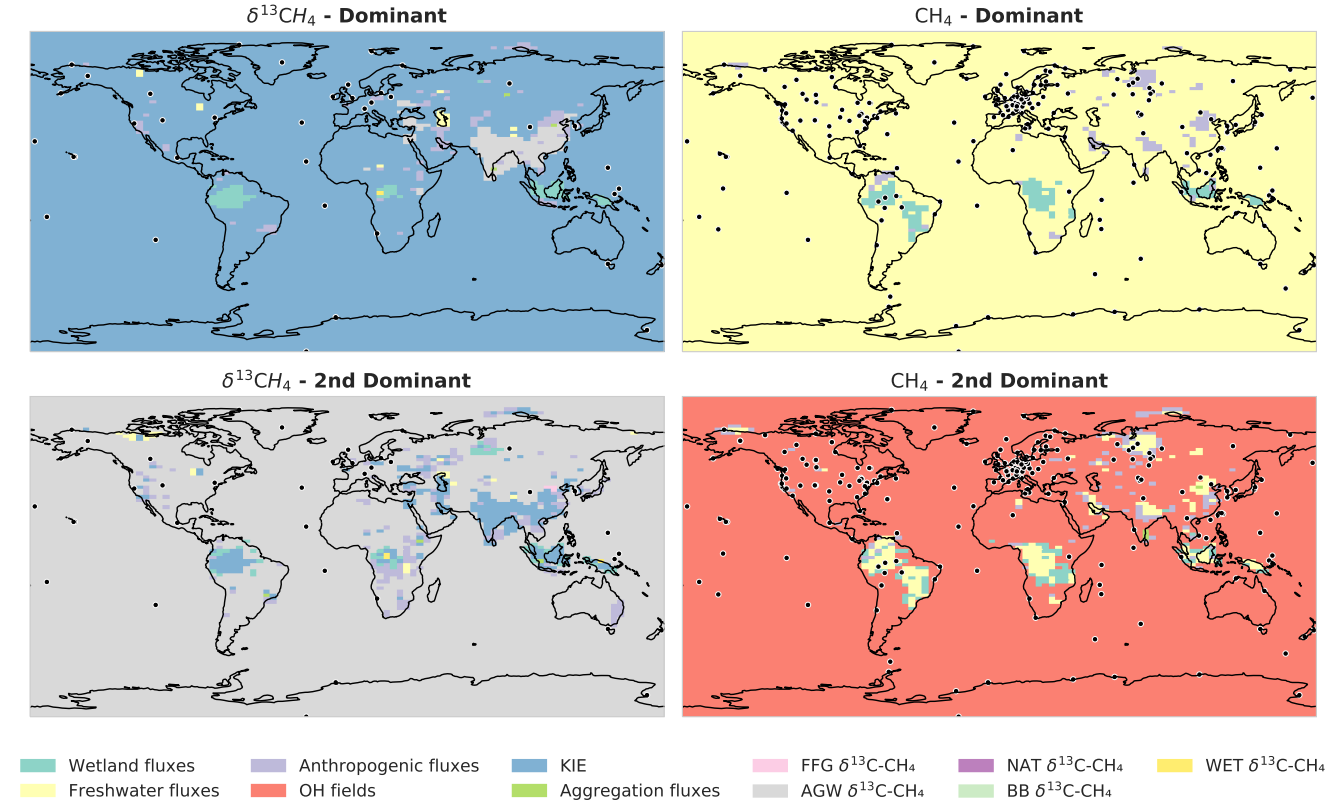

Figure 8. Spatial distribution of the dominant uncertainty driver (parameter with the highest RSD) in each grid cell at the surface. The second row of plots shows the dominant uncertainty category after removing the primary driver from the analysis. Surface stations are indicated with black dots.

of the relative importance of different uncertainty sources across regions. The main findings from these spatial patterns for the δ^{13}C-CH_4 signal are summarized as follows:

- In most areas, uncertainties in the OH-KIE dominate, accounting for approximately 50% of the total variance of δ^{13}C-CH_4 signal.
- AGW source signature uncertainties are particularly important in densely populated regions with intensive agricultural activity, notably over the Indo-Gangetic Plain, where their contribution reaches up to 80% of the total variance.
- Wetland flux uncertainties are most pronounced in tropical regions, especially over Borneo, the Amazon Basin, and Central Africa. In Borneo, the wetland flux contribution alone can represent over 60% of the total uncertainty in δ^{13}C-CH_4.

https://doi.org/10.5194/essd-2025-668
Preprint. Discussion started: 13 February 2026

– Freshwater flux uncertainties are particularly prominent in regions surrounding the Caspian Sea, where they account for more than 60% of the total variance in δ^{13}C-CH_4.

The second row of Figure 8 shows the secondary sources of uncertainty when the dominant driver is excluded, revealing additional parameters that might become critical if first-order uncertainties are reduced, such as freshwaters and anthropogenic fluxes. This spatial analysis highlights the need for region-specific strategies to reduce uncertainties in atmospheric δ^{13}C-CH_4 signals. For example, freshwater flux uncertainties dominate in the Caspian region, OH-KIE uncertainties are widespread, AGW source signature uncertainties peak over South Asia (especially the Indo-Gangetic Plain), and wetland-related uncertainties are highest in tropical wetlands such as Borneo and the Amazon. This breakdown allows us to identify which uncertainty drivers are potentially reducible through targeted improvements (e.g., inventories, field data, model representation), and which must be considered as intrinsic degrees of freedom requiring optimization in inversions (see Sect. 4.3.2). Furthermore, the results reveal a distinction between localized "hotspot" regions, where large uncertainties hinder flux attribution at the source scale (e.g., Indo-Gangetic Plain, Caspian basin, Borneo), and remote or well-mixed "background" regions, where uncertainties primarily affect large-scale budgets constrained by long-range transport and atmospheric mixing. This spatial distinction has important implications for inversion design, as discussed in Sect. 4.3.2.

4.3.2 Implications for isotopic inversions

The goal is to identify and reduce the causes of uncertainty in inversion results by improving prior information, such as inventories, process models, and field campaigns. Uncertainties that are intrinsic to the inversion system itself, however, cannot be reduced in this way and must instead be explicitly optimized within the inversion framework. This distinction guides the allocation of effort between inversion system refinement and external support from observational and inventory-based communities. Thanwerdas et al. (2022b) previously emphasized the need for comprehensive sensitivity analyses to systematically assess how multiple physical parameters, including transport, isotopic signatures, emission scenarios, and kinetic fractionation effects, affect atmospheric isotopic signals. Our study fills this gap by offering a spatially explicit, sectorally disaggregated uncertainty framework based on an ensemble of forward simulations (see Sect. 3.2).

Our results indicate that uncertainties in AGW source signatures, freshwater, and wetland fluxes tend to dominate in corresponding emission hotspots such as the Indo-Gangetic Plain, Caspian region, and Congo Basin, respectively (see Sect. 4.3.1). These hotspots should be targeted to reduce prior uncertainties via improved sectoral inventories, field isotopic characterizations, and process model refinements. AGW and BB source signatures should also be optimized during inversions, especially in regions with high emissions. As shown in Sect. 4.2.4, even small uncertainties in source signatures can induce isotopic signal variability exceeding observed variability at surface stations. Drinkwater et al. (2023) also highlighted the risks posed by overlapping or poorly constrained sectoral signatures. To effectively reduce uncertainties in these key regions, targeted efforts are needed beyond the inversion framework. This includes expanding and refining emission inventories with improved spatial and sectoral resolution, as well as conducting dedicated field campaigns to better characterize isotopic signatures on the ground. For example, the Congo Basin's extensive wetlands require comprehensive isotopic sampling campaigns to constrain

https://doi.org/10.5194/essd-2025-668
Preprint. Discussion started: 13 February 2026

Open Access Earth System Science Data Discussions

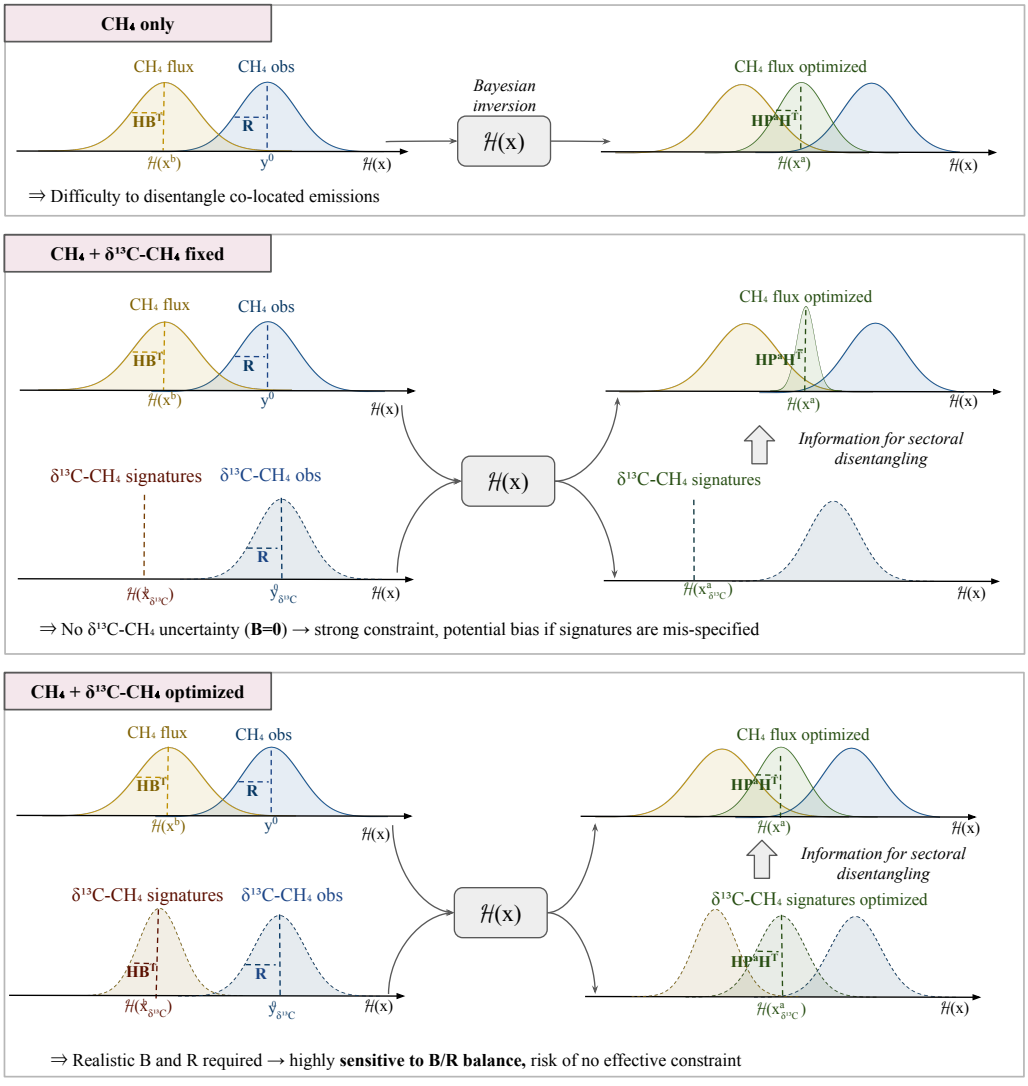

The effectiveness of δ¹³C-CH₄ constraint depends on how isotopes uncertainties are represented.

Figure 9. Schematic illustration of the effect of adding δ^{13}C–CH$_4$ constraints in the inversion. The upper panel shows the reference case using CH$_4$ only, where co-located emissions are difficult to disentangle. The middle panel illustrates the case where δ^{13}C–CH$_4$ signatures are fixed with no uncertainty (B = 0), which provides a strong constraint but may lead to potential biases if the signatures are mis-specified. The lower panel shows the case where δ^{13}C–CH$_4$ signatures are optimized with realistic uncertainties, which improves the ability to disentangle emission sectors but requires a careful balance between B and R to avoid ineffective constraints. Coloured Gaussian curves represent prior, observational and posterior distributions for CH$_4$ fluxes and δ^{13}C–CH$_4$ signatures, with the forward model H(x) linking the parameter space to the observation space.

https://doi.org/10.5194/essd-2025-668
Preprint. Discussion started: 13 February 2026

wetland emission signatures, while the Indo-Gangetic Plain would benefit from improved agricultural and waste sector inventories coupled with isotopic measurements. Similarly, enhanced process-based modeling supported by laboratory and field studies is crucial to accurately represent freshwater and wetland methane dynamics. Without these concerted external efforts, isotopic inversions face inherent limitations: unresolved uncertainties in prior data will propagate through inversions, leading to ambiguous source attribution and degraded flux estimates, particularly in emission hotspots where sectoral overlaps are strong (see Figure. 3).

In contrast, uncertainties related to the OH-KIE are widespread, large, and relatively homogeneous across background regions. This pervasive influence implies that OH-KIE uncertainties must be treated as intrinsic to the inversion and explicitly accounted for within the framework, e.g., via ensemble-based or variational approaches that sample its plausible range, unless they can be reduced through improved experimental and theoretical characterization. This conclusion aligns with recommendations from Lan et al. (2021a). The distinction between hotspot and background uncertainties is central to inversion design: localized uncertainties (AGW isotopic signature, freshwater, wetland fluxes) impact the representation and attribution of strong regional signals near measurement sites, while background uncertainties (e.g., OH-KIE) influence large-scale isotopic gradients essential for inferring hemispheric flux distributions. These conclusions reinforce earlier findings by Basu et al. (2022) and Thanwerdas et al. (2024), who highlighted the lack of robust, data-driven estimates of source signature and KIE uncertainties in current δ^{13}C-CH_4 inversions.

The relatively minor impact of flux aggregation choices on both CH_4 mole fractions and δ^{13}C-CH_4 suggests that the isotopic signature maps developed here can be flexibly applied across different inversion systems and emission inventories. However, care must be taken when aggregating sub-sectors with heterogeneous isotopic signatures. For example, livestock and waste within the AGW sector have distinct isotopic signatures, as illustrated in Table 1, and aggregating them without distinction could significantly bias the isotopic priors and affect inversion results. This recommendation is aligned with Menoud et al. (2022), who advocate for the separation of livestock and waste subcategories. Mannisenaho et al. (2023) also emphasized the importance of consistent source signatures to obtain more robust isotopic inversions.

The sector-specific total uncertainties quantified here (σ_{tot} in Table 4) provide a basis for specifying the diagonal terms of the prior error covariance matrix (B matrix) in inversion frameworks. This addresses a critical need identified by Basu et al. (2022) and Thanwerdas et al. (2024), who noted that inversions often lack realistic prior error magnitudes, especially for source isotopic signatures and KIE. The values derived in this study enable construction of better-calibrated B matrices consistent with observed atmospheric variability and parameter sensitivities. Where observations are sparse, particularly in the Southern Hemisphere, strong spatial correlations between regional source signatures may arise. In such cases, the stability of inversion systems may be improved with a spatial clustering based on isotopic similarities.

In parallel, the sensitivity analysis quantifies how each parameter perturbs simulated CH_4 and δ^{13}C-CH_4 fields, and provides a basis to construct the prior uncertainty matrix (B matrix) in the parameter space. The observation error matrix (R matrix) is typically derived from the standard deviation of observations, combined with model–observation mismatch and representativeness errors. The relative magnitude of B and R determines whether an inversion can effectively constrain a given parameter: if prior uncertainty (B) is large compared to observational uncertainty (R), and the parameter has a detectable impact on the

https://doi.org/10.5194/essd-2025-668
Preprint. Discussion started: 13 February 2026

modeled fields, the inversion has the potential to significantly reduce uncertainty. Conversely, if B is small or R is large, the observational constraint will be weak, and the posterior estimate will remain close to the prior. These relationships, between B, R, and the potential for parameter constraint are illustrated schematically in Figure 3 and in Figure 9 when adding the isotopic constraint.

For CH_4 mole fractions, freshwater emissions should be considered in inversions, but given the large uncertainties in these fluxes, it may be preferable to include them within the broader wetland category rather than treating them as a separate source. This approach reduces relative uncertainty while still accounting for freshwater contributions, until more observational data become available for more accurate flux estimates (see Sect. 4.2.2). Omitting them entirely could bias regional flux attribution, especially over Central Asia and tropical regions, where freshwater fluxes exhibit strong spatial variability.

Similarly, uncertainties in OH concentrations, although not isotopically active, significantly propagate into mole fraction variability and should be incorporated via chemistry ensemble fields.

4.3.3 Pathways for improvement

Future work should aim to better account for the temporal evolution of livestock isotopic signatures, particularly in regions where changes in feeding practices (C_3 versus C_4 plant diets) have occurred over recent decades (Chang et al., 2019; Lan et al., 2021a). Additionally, improving the differentiation between waste sub-sectors (landfills, wastewater, agricultural waste) would enhance the precision of AGW source signatures (Menoud et al., 2022). Seasonal variations in δ^{13}C-CH_4 are particularly sensitive to small shifts in isotopic source signatures, which can significantly affect both the seasonal amplitude and phase of the atmospheric signal (Kangasaho et al., 2022), underscoring the importance of improving the temporal characterization of source signatures.

Further improvements should include assessing the sensitivity of inversions to the choice of atmospheric transport models, including the influence of spatial resolution and model biases. Additional oxidation pathways, such as CH_4 loss to Cl radicals and soil uptake, remain poorly quantified and could affect both mole fraction and isotopic budgets. Beyond inversion systems themselves, several supporting research efforts are essential to reduce key input uncertainties. These include field campaigns to better constrain isotopic source signatures (e.g., for wetlands, waste, and agriculture), development of regional inventories with isotopic speciation, and improved lab-based estimates of KIE parameters. As emphasized by Thanwerdas et al. (2024), inversion results remain highly sensitive to prescribed errors, and robust, observation-based estimates of regional uncertainties in δ^{13}C-CH_4 signatures are still lacking. Without these supporting activities, inversion systems risk systematic biases or overfitting due to unrealistic priors (see Figure 9).

While inversions remain a powerful tool for constraining the global methane budget, they critically depend on external inputs that must be improved in parallel. Targeted field campaigns in tropical wetlands, major fossil production basins, and under-sampled freshwater systems could greatly improve prior flux estimates and isotopic signatures. Enhanced reporting of national sectoral emissions, particularly for waste and agriculture, and site-specific isotopic measurements are urgently needed to reduce the major uncertainties identified in this study. Finally, process-based models of wetland and freshwater CH_4

https://doi.org/10.5194/essd-2025-668
Preprint. Discussion started: 13 February 2026

emissions suffer from a lack of data on hydrological dynamics, organic matter content, and microbial reaction and population dynamics, particularly in tropical regions where large emissions coincide with sparse observations.

5 Conclusions

Existing global δ^{13}C–CH_4 datasets (e.g., Lan et al., 2021a; Oh et al., 2022; Menoud et al., 2022; Thanwerdas et al., 2024) have provided valuable benchmarks but were limited in temporal coverage, systematic uncertainty quantification, and compatibility with inversion-ready sectoral structures. To address these limitations, we produced an updated global dataset of δ^{13}C–CH_4 source signatures for five major natural and anthropogenic sectors, following the Global Methane Budget (GMB) classification. This aggregation strategy reduces the number of categories for computational efficiency in future inversion studies while preserving isotopic representativeness across emission types. The maps cover the period 1998–2022 and integrate recent spatially explicit datasets and literature-derived observations, providing explicit estimates of both intrinsic (within-sector) and aggregation-related uncertainties. Overall, this new dataset offers a temporally extended, uncertainty-quantified, and inversion-ready basis for atmospheric modeling and isotopic inversions.

Using forward simulations in the Community Inversion Framework coupled to the LMDz transport model, we conducted a comprehensive sensitivity analysis to assess the influence of key parameters on the modeled atmospheric δ^{13}C-CH_4 signal and CH_4 mole fraction. Our results highlight that uncertainties in methane oxidation chemistry, particularly related to the OH kinetic isotope effect (KIE), and uncertainties in isotopic source signatures, especially from the agriculture and waste (AGW) sector, have the largest impact on the simulated isotopic ratios. By contrast, uncertainties related to flux aggregation, fossil fuel (FFG), wetland (WET) and other natural (NAT) isotopic source signatures have a more limited influence on global atmospheric signals.

We showed that isotopic uncertainties within certain sectors, such as the AGW sector (up to $\pm 3‰$), were substantial when compared to the standard deviation of atmospheric δ^{13}C-CH_4 observations at surface stations (approximately $\pm 0.2‰$). This emphasizes the importance of reducing uncertainties in source-specific signatures and isotopic fractionation processes to improve the reliability of atmospheric inversions.

Our results demonstrated the robustness of the proposed sector aggregation approach and confirmed the applicability of the updated isotopic maps across diverse inversion configurations. We recommend prioritizing efforts to better constrain isotopic signatures in the agriculture and waste sector, and to refine the OH kinetic isotope effect. Moreover, the methodology presented here for quantifying sectoral δ^{13}C-CH_4 uncertainties can be applied to future datasets as new observations become available, allowing the isotopic maps to be updated and the associated uncertainties reduced. In addition, we provide practical guidelines for configuring isotopic inversions, including recommended uncertainty ranges, key parameters to target for enhanced source attribution, and the use of regional optimization strategies in areas where uncertainties are most significant. The sectoral uncertainty estimates provided here can directly inform the specification of prior error covariance matrices in atmospheric inversion frameworks, thereby improving the consistency between sensitivity analyses and inversion configurations.

https://doi.org/10.5194/essd-2025-668
Preprint. Discussion started: 13 February 2026

This study focused on developing and evaluating updated δ^{13}C-CH_4 source signature maps through comparison with the literature, uncertainty quantification, and forward simulations. While direct validation using atmospheric data is beyond the scope of this paper, all necessary elements are provided, including gridded maps, uncertainty ranges, and sectoral breakdowns, to enable their integration into forward modeling and atmospheric inversions under optimal conditions.

Finally, the increasing availability of satellite-based CH_4 and isotopic measurements opens promising perspectives for constraining methane sources at the global scale. Recent feasibility studies (e.g. Malina et al., 2018, 2019) have shown that instruments such as GOSAT-2, TROPOMI, and Sentinel-5/UVNS could theoretically retrieve $^{13}CH_4$ with sub-ppbv precision, although such accuracy often requires extensive spatial or temporal averaging and depends strongly on temperature and pressure profiles. Future sensitivity analyses using atmospheric inversion frameworks (e.g. CIF–LMDz) will be essential to evaluate whether current or forthcoming missions can effectively detect and interpret atmospheric isotopic variations under real conditions.

Code and data availability. Isotopic source signature datasets were provided by Xin Lan, Malika Menoud, Youmi Oh, and Giuseppe Etiope. The gridded δ^{13}C-CH_4 source signature dataset (1998–2022) developed in this study is openly available at the ESA Open Science Data portal: https://opensciencedata.esa.int/products/d13c-ch4-signatures-smart-ch4/collection. A DOI for the dataset is currently being processed by ESA and will be provided in the near future. The atmospheric modeling framework used for the sensitivity analysis is based on the Community Inversion Framework (CIF; https://doi.org/10.5194/gmd-14-5331-2021) coupled to the LMDz transport model. Scripts used for dataset processing and uncertainty analysis are available upon request from the corresponding author.

Author contributions. ET compiled and aggregated the isotopic datasets, performed temporal extrapolations, designed and carried out the simulation experiments, and analyzed the results. AB and MS contributed to the study design, supervised the project, and supported the interpretation of results and manuscript preparation. AM processed the meteorological mass fluxes used to drive the transport model, contributed data processing scripts, and provided technical support for implementation in the Community Inversion Framework. MN and XL provided source-specific isotopic datasets. MM, JT, DG and EM provided expertise on isotopic datasets and feedback on the analysis. ET prepared the manuscript with contributions from all co-authors.

Competing interests. The authors declare no competing interests relative to the present study.

Acknowledgements. This work was also was conducted in the frame of the ESA initiative SMART-CH4 (Satellite Monitoring of Atmospheric Methane, contract no. 4000142730/23/I-NS), which is part of the EC-ESA Joint Earth System Science Initiative. This work was granted access to the HPC resources of TGCC under the allocations A0140102201 made by GENCI.

Finally, we wish to thank J. Bruna (LSCE) and his team for computer support and the use of the OBELIX computing facility at LSCE.

https://doi.org/10.5194/essd-2025-668
Preprint. Discussion started: 13 February 2026

Open Access Earth System Science Data Discussions

References

Basu, S., Lan, X., Dlugokencky, E., Michel, S., Schwietzke, S., Miller, J. B., Bruhwiler, L., Oh, Y., Tans, P. P., Apadula, F., Gatti, L. V., Jordan, A., Necki, J., Sasakawa, M., Morimoto, S., Di Iorio, T., Lee, H., Arduini, J., and Manca, G.: Estimating Emissions of Methane Consistent with Atmospheric Measurements of Methane and δ^{13}C of Methane, Atmospheric Chemistry and Physics, 22, 15 351–15 377, https://doi.org/10.5194/acp-22-15351-2022, 2022.

Berchet, A., Sollum, E., Thompson, R. L., Pison, I., Thanwerdas, J., Broquet, G., Chevallier, F., Aalto, T., Berchet, A., Bergamaschi, P., Brunner, D., Engelen, R., Fortems-Cheiney, A., Gerbig, C., Groot Zwaaftink, C. D., Haussaire, J.-M., Henne, S., Houweling, S., Karstens, U., Kutsch, W. L., Luijkx, I. T., Monteil, G., Palmer, P. I., van Peet, J. C. A., Peters, W., Peylin, P., Potier, E., Rödenbeck, C., Saunois, M., Scholze, M., Tsuruta, A., and Zhao, Y.: The Community Inversion Framework v1.0: A Unified System for Atmospheric Inversion Studies, Geoscientific Model Development, 14, 5331–5354, https://doi.org/10.5194/gmd-14-5331-2021, 2021.

Bergamaschi, P., Krol, M., Meirink, J. F., Dentener, F., Segers, A., van Aardenne, J., Monni, S., Vermeulen, A. T., Schmidt, M., Ramonet, M., Yver, C., Meinhardt, F., Nisbet, E. G., Fisher, R. E., O'Doherty, S., and Dlugokencky, E. J.: Inverse Modeling of European CH_4\ Emissions 2001-2006, J. Geophys. Res., 115, https://doi.org/10.1029/2010JD014180, 2010.

Bergamaschi, P., Houweling, S., Segers, A., Krol, M., Frankenberg, C., Scheepmaker, R. A., Dlugokencky, E., Wofsy, S. C., Kort, E. A., Sweeney, C., Schuck, T., Brenninkmeijer, C., Chen, H., Beck, V., and Gerbig, C.: Atmospheric CH4 in the First Decade of the 21st Century: Inverse Modeling Analysis Using SCIAMACHY Satellite Retrievals and NOAA Surface Measurements, J. Geophys. Res. Atmos., 118, 7350–7369, https://doi.org/10.1002/jgrd.50480, 2013.

Bergamaschi, P., Karstens, U., Manning, A. J., Saunois, M., Tsuruta, A., Berchet, A., Vermeulen, A. T., Arnold, T., Janssens-Maenhout, G., Hammer, S., Levin, I., Schmidt, M., Ramonet, M., Lopez, M., Lavric, J., Aalto, T., Chen, H., Feist, D. G., Gerbig, C., Haszpra, L., Hermansen, O., Manca, G., Moncrieff, J., Meinhardt, F., Necki, J., Galkowski, M., O'Doherty, S., Paramonova, N., Scheeren, H. A., Steinbacher, M., and Dlugokencky, E.: Inverse Modelling of European CH_4 Emissions during 2006–2012 Using Different Inverse Models and Reassessed Atmospheric Observations, Atmospheric Chemistry and Physics, 18, 901–920, https://doi.org/10.5194/acp-18-901-2018, 2018.

Bernard, J., Saunois, M., Salmon, E., Ciais, P., Peng, S., Berchet, A., Serrano-Ortiz, P., Gnanamoorthy, P., and Jansen, J.: Satellite-Based Modeling of Wetland Methane Emissions on a Global Scale (SatWetCH4 1.0), https://doi.org/10.5194/egusphere-2024-1331, 2024.

Bohn, T. J., Melton, J. R., Ito, A., Kleinen, T., Spahni, R., Stocker, B. D., Zhang, B., Zhu, X., Schroeder, R., Glagolev, M. V., Maksyutov, S., Brovkin, V., Chen, G., Denisov, S. N., Eliseev, A. V., Gallego-Sala, A., McDonald, K. C., Rawlins, M. A., Riley, W. J., Subin, Z. M., Tian, H., Zhuang, Q., and Kaplan, J. O.: WETCHIMP-WSL: Intercomparison of Wetland Methane Emissions Models over West Siberia, Biogeosciences, 12, 3321–3349, https://doi.org/10.5194/bg-12-3321-2015, 2015.

Bourn, M., Robinson, R., Innocenti, F., and Scheutz, C.: Regulating Landfills Using Measured Methane Emissions: An English Perspective, Waste Management, 87, 860–869, https://doi.org/10.1016/j.wasman.2018.06.032, 2019.

Brownlow, R., Lowry, D., Fisher, R. E., France, J. L., Lanoisellé, M., White, B., Wooster, M. J., Zhang, T., and Nisbet, E. G.: Isotopic Ratios of Tropical Methane Emissions by Atmospheric Measurement, Global Biogeochemical Cycles, 31, 1408–1419, https://doi.org/10.1002/2017GB005689, 2017.

Camin, F., Besic, D., Brewer, P. J., Allison, C. E., Coplen, T. B., Dunn, P. J. H., Gehre, M., Gröning, M., Meijer, H. A. J., Hélie, J.-F., Iacumin, P., Kraft, R., Krajnc, B., Kümmel, S., Lee, S., Meija, J., Mester, Z., Mohn, J., Moossen, H., Qi, H., Skrzypek, G., Sperlich, P., Viallon,

https://doi.org/10.5194/essd-2025-668
Preprint. Discussion started: 13 February 2026

J., Wassenaar, L. I., and Wielgosz, R. I.: Stable Isotope Reference Materials and Scale Definitions—Outcomes of the 2024 IAEA Experts Meeting, Rapid Communications in Mass Spectrometry, 39, e10 018, https://doi.org/10.1002/rcm.10018, 2025.

Cantrell, C. A., Shetter, R. E., McDaniel, A. H., Calvert, J. G., Davidson, J. A., Lowe, D. C., Tyler, S. C., Cicerone, R. J., and Greenberg, J. P.: Carbon Kinetic Isotope Effect in the Oxidation of Methane by the Hydroxyl Radical, Journal of Geophysical Research: Atmospheres, 95, 22 455–22 462, https://doi.org/10.1029/JD095iD13p22455, 1990.

Chandra, N., Patra, P. K., Fujita, R., Höglund-Isaksson, L., Umezawa, T., Goto, D., Morimoto, S., Vaughn, B. H., and Röckmann, T.: Methane Emissions Decreased in Fossil Fuel Exploitation and Sustainably Increased in Microbial Source Sectors during 1990–2020, Communications Earth & Environment, 5, 1–15, https://doi.org/10.1038/s43247-024-01286-x, 2024.

Chang, J., Peng, S., Ciais, P., Saunois, M., Dangal, S. R. S., Herrero, M., Havlík, P., Tian, H., and Bousquet, P.: Revisiting Enteric Methane Emissions from Domestic Ruminants and Their δ13CCH4 Source Signature, Nature Communications, 10, 3420, https://doi.org/10.1038/s41467-019-11066-3, 2019.

Chanton, J. P., Rutkowski, C. M., Schwartz, C. C., Ward, D. E., and Boring, L.: Factors Influencing the Stable Carbon Isotopic Signature of Methane from Combustion and Biomass Burning, Journal of Geophysical Research: Atmospheres, 105, 1867–1877, https://doi.org/10.1029/1999JD900909, 2000.

Chevallier, F., Fisher, M., Peylin, P., Serrar, S., Bousquet, P., Bréon, F. M., Chédin, A., and Ciais, P.: Inferring CO_2\ Sources and Sinks from Satellite Observations: Method and Application to TOVS Data, J. Geophys. Res., 110, D24 309, https://doi.org/10.1029/2005JD006390, 2005.

Collins, W. J., Lamarque, J.-F., Schulz, M., Boucher, O., Eyring, V., Hegglin, M. I., Maycock, A., Myhre, G., Prather, M., Shindell, D., and Smith, S. J.: AerChemMIP: Quantifying the Effects of Chemistry and Aerosols in CMIP6, Geoscientific Model Development, 10, 585–607, https://doi.org/10.5194/gmd-10-585-2017, 2017.

Crippa, M., Guizzardi, D., Schaaf, E., Monforti-Ferrario, F., Quadrelli, R., Risquez Martin, A., Rossi, S., Vignati, E., Muntean, M., Brandao De Melo, J., Oom, D., Pagani, F., Banja, M., Taghavi-Moharamli, P., Köykkä, J., Grassi, G., Branco, A., and San-Miguel, J.: GHG Emissions of All World Countries: 2023, Publications Office of the European Union, ISBN 978-92-68-07550-0, 2023.

Douglas, P. M. J., Stratigopoulos, E., Park, S., and Phan, D.: Geographic Variability in Freshwater Methane Hydrogen Isotope Ratios and Its Implications for Global Isotopic Source Signatures, Biogeosciences, 18, 3505–3527, https://doi.org/10.5194/bg-18-3505-2021, 2021.

Drinkwater, A., Palmer, P. I., Feng, L., Arnold, T., Lan, X., Michel, S. E., Parker, R., and Boesch, H.: Atmospheric Data Support a Multi-Decadal Shift in the Global Methane Budget towards Natural Tropical Emissions, Atmospheric Chemistry and Physics, 23, 8429–8452, https://doi.org/10.5194/acp-23-8429-2023, 2023.

Dunn, P. J. H., Malinovsky, D., Ogrinc, N., Potočnik, D., Flierl, L., Rienitz, O., Paul, D., and Meijer, H. A. J.: Re-Determination of R(13C/12C) for Vienna Peedee Belemnite (VPDB), Rapid Communications in Mass Spectrometry, 38, e9773, https://doi.org/10.1002/rcm.9773, 2024.

Etiope, G., Ciotoli, G., Schwietzke, S., and Schoell, M.: Gridded Maps of Geological Methane Emissions and Their Isotopic Signature, Earth System Science Data, 11, 1–22, https://doi.org/10.5194/essd-11-1-2019, 2019.

European Commission: MEthane Goes MObile - MEasurements and MOdelling | MEMO2 | Projekt | Fact Sheet | H2020, https://cordis.europa.eu/project/id/722479, 2017.

Ferrario, F. M., Crippa, M., Guizzardi, D., Muntean, M., Schaaf, E., Vullo, E. L., Solazzo, E., Olivier, J., and Vignati, E.: EDGAR v6.0 Greenhouse Gas Emissions, 2021.

https://doi.org/10.5194/essd-2025-668
Preprint. Discussion started: 13 February 2026

Forster, P. M., Smith, C. J., Walsh, T., Lamb, W. F., Lamboll, R., Hauser, M., Ribes, A., Rosen, D., Gillett, N., Palmer, M. D., Rogelj, J., von Schuckmann, K., Seneviratne, S. I., Trewin, B., Zhang, X., Allen, M., Andrew, R., Birt, A., Borger, A., Boyer, T., Broersma, J. A., Cheng, L., Dentener, F., Friedlingstein, P., Gutiérrez, J. M., Gütschow, J., Hall, B., Ishii, M., Jenkins, S., Lan, X., Lee, J.-Y., Morice, C., Kadow, C., Kennedy, J., Killick, R., Minx, J. C., Naik, V., Peters, G. P., Pirani, A., Pongratz, J., Schleussner, C.-F., Szopa, S., Thorne, P., Rohde, R., Rojas Corradi, M., Schumacher, D., Vose, R., Zickfeld, K., Masson-Delmotte, V., and Zhai, P.: Indicators of Global Climate Change 2022: Annual Update of Large-Scale Indicators of the State of the Climate System and Human Influence, Earth System Science Data, 15, 2295–2327, https://doi.org/10.5194/essd-15-2295-2023, 2023a.

Forster, P. M., Smith, C. J., Walsh, T., Lamb, W. F., Lamboll, R., Hauser, M., Ribes, A., Rosen, D., Gillett, N., Palmer, M. D., Rogelj, J., von Schuckmann, K., Seneviratne, S. I., Trewin, B., Zhang, X., Allen, M., Andrew, R., Birt, A., Borger, A., Boyer, T., Broersma, J. A., Cheng, L., Dentener, F., Friedlingstein, P., Gutiérrez, J. M., Gütschow, J., Hall, B., Ishii, M., Jenkins, S., Lan, X., Lee, J.-Y., Morice, C., Kadow, C., Kennedy, J., Killick, R., Minx, J. C., Naik, V., Peters, G. P., Pirani, A., Pongratz, J., Schleussner, C.-F., Szopa, S., Thorne, P., Rohde, R., Rojas Corradi, M., Schumacher, D., Vose, R., Zickfeld, K., Masson-Delmotte, V., and Zhai, P.: Indicators of Global Climate Change 2022: Annual Update of Large-Scale Indicators of the State of the Climate System and Human Influence, Earth System Science Data, 15, 2295–2327, https://doi.org/10.5194/essd-15-2295-2023, 2023b.

France, J. L., Lunt, M. F., Andrade, M., Moreno, I., Ganesan, A. L., Lachlan-Cope, T., Fisher, R. E., Lowry, D., Parker, R. J., Nisbet, E. G., and Jones, A. E.: Very Large Fluxes of Methane Measured above Bolivian Seasonal Wetlands, Proceedings of the National Academy of Sciences, 119, e2206345 119, https://doi.org/10.1073/pnas.2206345119, 2022.

Fujita, R., Morimoto, S., Maksyutov, S., Kim, H.-S., Arshinov, M., Brailsford, G., Aoki, S., and Nakazawa, T.: Global and Regional CH4 Emissions for 1995–2013 Derived From Atmospheric CH4, δ13C-CH4, and δD-CH4 Observations and a Chemical Transport Model, Journal of Geophysical Research: Atmospheres, 125, e2020JD032 903, https://doi.org/10.1029/2020JD032903, 2020.

Ganesan, A. L., Stell, A. C., Gedney, N., Comyn-Platt, E., Hayman, G., Rigby, M., Poulter, B., and Hornibrook, E. R. C.: Spatially Resolved Isotopic Source Signatures of Wetland Methane Emissions, Geophysical Research Letters, 45, 3737–3745, https://doi.org/10.1002/2018GL077536, 2018.

Gaubert, B., Worden, H. M., Arellano, A. F. J., Emmons, L. K., Tilmes, S., Barré, J., Martinez Alonso, S., Vitt, F., Anderson, J. L., Alkemade, F., Houweling, S., and Edwards, D. P.: Chemical Feedback From Decreasing Carbon Monoxide Emissions, Geophysical Research Letters, 44, 9985–9995, https://doi.org/10.1002/2017GL074987, 2017.

Global Methane Pledge: Global Methane Pledge:, https://www. 2717 globalmethanepledge.org/#pledges, 2023.

Guthrie, P. D.: The CH4 - CO - OH Conundrum: A Simple Analytic Approach, Global Biogeochemical Cycles, 3, 287–298, https://doi.org/10.1029/GB003i004p00287, 1989.

Hauglustaine, D. A., Hourdin, F., Jourdain, L., Filiberti, M.-A., Walters, S., Lamarque, J.-F., and Holland, E. A.: Interactive Chemistry in the Laboratoire de Météorologie Dynamique General Circulation Model: Description and Background Tropospheric Chemistry Evaluation, Journal of Geophysical Research: Atmospheres, 109, https://doi.org/10.1029/2003JD003957, 2004.

Höglund-Isaksson, L., Gómez-Sanabria, A., Klimont, Z., Rafaj, P., and Schöpp, W.: Technical Potentials and Costs for Reducing Global Anthropogenic Methane Emissions in the 2050 Timeframe –Results from the GAINS Model, Environmental Research Communications, 2, 025 004, https://doi.org/10.1088/2515-7620/ab7457, 2020.

Holmes, C. D., Prather, M. J., Søvde, O. A., and Myhre, G.: Future Methane, Hydroxyl, and Their Uncertainties: Key Climate and Emission Parameters for Future Predictions, Atmospheric Chemistry and Physics, 13, 285–302, https://doi.org/10.5194/acp-13-285-2013, 2013.

https://doi.org/10.5194/essd-2025-668
Preprint. Discussion started: 13 February 2026

Hourdin, F., Talagrand, O., and Idelkadi, A.: Eulerian Backtracking of Atmospheric Tracers. II: Numerical Aspects, Q.J.R. Meteorol. Soc., 132, 585–603, https://doi.org/10.1256/qj.03.198.B, 2006.

Houweling, S., Bergamaschi, P., Chevallier, F., Heimann, M., Kaminski, T., Krol, M., Michalak, A. M., and Patra, P.: Global Inverse Modeling of CH_4 Sources and Sinks: An Overview of Methods, Atmospheric Chemistry and Physics, 17, 235–256, https://doi.org/10.5194/acp-17-235-2017, 2017.

IEA: US Natural Gas Production by Source, https://www.iea.org/data-and-statistics/charts/us-natural-gas-production-by-source-2013-2023, 2013-2023.

Jackson, R. B., Saunois, M., Bousquet, P., Canadell, J. G., Poulter, B., Stavert, A. R., Bergamaschi, P., Niwa, Y., Segers, A., and Tsuruta, A.: Increasing Anthropogenic Methane Emissions Arise Equally from Agricultural and Fossil Fuel Sources, Environmental Research Letters, 15, 071 002, https://doi.org/10.1088/1748-9326/ab9ed2, 2020.

Jackson, R. B., Saunois, M., Martinez, A., Canadell, J. G., Yu, X., Li, M., Poulter, B., Raymond, P. A., Regnier, P., Ciais, P., Davis, S. J., and Patra, P. K.: Human Activities Now Fuel Two-Thirds of Global Methane Emissions, Environmental Research Letters, 19, 101 002, https://doi.org/10.1088/1748-9326/ad6463, 2024.

Kangasaho, V., Tsuruta, A., Backman, L., Mäkinen, P., Houweling, S., Segers, A., Krol, M., Dlugokencky, E. J., Michel, S., White, J. W. C., and Aalto, T.: The Role of Emission Sources and Atmospheric Sink in the Seasonal Cycle of CH4 and δ13-CH4: Analysis Based on the Atmospheric Chemistry Transport Model TM5, Atmosphere, 13, 888, https://doi.org/10.3390/atmos13060888, 2022.

Karlson, M. and Bastviken, D.: Multi-Source Mapping of Peatland Types Using Sentinel-1, Sentinel-2, and Terrain Derivatives—A Comparison Between Five High-Latitude Landscapes, Journal of Geophysical Research: Biogeosciences, 128, e2022JG007 195, https://doi.org/10.1029/2022JG007195, 2023.

Kirschke, S., Bousquet, P., Ciais, P., Saunois, M., Canadell, J. G., Dlugokencky, E. J., Bergamaschi, P., Bergmann, D., Blake, D. R., Bruhwiler, L., Cameron-Smith, P., Castaldi, S., Chevallier, F., Feng, L., Fraser, A., Heimann, M., Hodson, E. L., Houweling, S., Josse, B., Fraser, P. J., Krummel, P. B., Lamarque, J.-F., Langenfelds, R. L., Le Quéré, C., Naik, V., O'Doherty, S., Palmer, P. I., Pison, I., Plummer, D., Poulter, B., Prinn, R. G., Rigby, M., Ringeval, B., Santini, M., Schmidt, M., Shindell, D. T., Simpson, I. J., Spahni, R., Steele, L. P., Strode, S. A., Sudo, K., Szopa, S., van der Werf, G. R., Voulgarakis, A., van Weele, M., Weiss, R. F., Williams, J. E., and Zeng, G.: Three Decades of Global Methane Sources and Sinks, Nature Geosci, 6, 813–823, https://doi.org/10.1038/ngeo1955, 2013.

Knox, S. H., Bansal, S., McNicol, G., Schafer, K., Sturtevant, C., Ueyama, M., Valach, A. C., Baldocchi, D., Delwiche, K., Desai, A. R., Euskirchen, E., Liu, J., Lohila, A., Malhotra, A., Melling, L., Riley, W., Runkle, B. R. K., Turner, J., Vargas, R., Zhu, Q., Alto, T., Fluet-Chouinard, E., Goeckede, M., Melton, J. R., Sonnentag, O., Vesala, T., Ward, E., Zhang, Z., Feron, S., Ouyang, Z., Alekseychik, P., Aurela, M., Bohrer, G., Campbell, D. I., Chen, J., Chu, H., Dalmagro, H. J., Goodrich, J. P., Gottschalk, P., Hirano, T., Iwata, H., Jurasinski, G., Kang, M., Koebsch, F., Mammarella, I., Nilsson, M. B., Ono, K., Peichl, M., Peltola, O., Ryu, Y., Sachs, T., Sakabe, A., Sparks, J. P., Tuittila, E.-S., Vourlitis, G. L., Wong, G. X., Windham-Myers, L., Poulter, B., and Jackson, R. B.: Identifying Dominant Environmental Predictors of Freshwater Wetland Methane Fluxes across Diurnal to Seasonal Time Scales, Global Change Biology, 27, 3582–3604, https://doi.org/10.1111/gcb.15661, 2021.

Krautwurst, S., Gerilowski, K., Jonsson, H. H., Thompson, D. R., Kolyer, R. W., Iraci, L. T., Thorpe, A. K., Horstjann, M., Eastwood, M., Leifer, I., Vigil, S. A., Krings, T., Borchardt, J., Buchwitz, M., Fladeland, M. M., Burrows, J. P., and Bovensmann, H.: Methane Emissions from a Californian Landfill, Determined from Airborne Remote Sensing and in Situ Measurements, Atmospheric Measurement Techniques, 10, 3429–3452, https://doi.org/10.5194/amt-10-3429-2017, 2017.

https://doi.org/10.5194/essd-2025-668
Preprint. Discussion started: 13 February 2026

Lan, X., Basu, S., Schwietzke, S., Bruhwiler, L. M. P., Dlugokencky, E. J., Michel, S. E., Sherwood, O. A., Tans, P. P., Thoning, K., Etiope, G., Zhuang, Q., Liu, L., Oh, Y., Miller, J. B., Pétron, G., Vaughn, B. H., and Crippa, M.: Improved Constraints on Global Methane Emissions and Sinks Using δ13C-CH4, Global Biogeochemical Cycles, 35, e2021GB007 000, https://doi.org/10.1029/2021GB007000, 2021a.

Lan, X., Nisbet, E. G., Dlugokencky, E. J., and Michel, S. E.: What Do We Know about the Global Methane Budget? Results from Four Decades of Atmospheric CH4 Observations and the Way Forward, Philosophical Transactions of the Royal Society A: Mathematical, Physical and Engineering Sciences, 379, 20200 440, https://doi.org/10.1098/rsta.2020.0440, 2021b.

Lan, X., Thoning, K., and Dlugokencky, E.: Trends in Globally-Averaged CH4, N2O, and SF6 Determined from NOAA Global Monitoring Laboratory Measurements, https://doi.org/10.15138/P8XG-AA10, 2025.

Lauerwald, R., Allen, G. H., Deemer, B. R., Liu, S., Maavara, T., Raymond, P., Alcott, L., Bastviken, D., Hastie, A., Holgerson, M. A., Johnson, M. S., Lehner, B., Lin, P., Marzadri, A., Ran, L., Tian, H., Yang, X., Yao, Y., and Regnier, P.: Inland Water Greenhouse Gas Budgets for RECCAP2: 1. State-Of-The-Art of Global Scale Assessments, Global Biogeochemical Cycles, 37, e2022GB007 657, https://doi.org/10.1029/2022GB007657, 2023.

Lauvaux, T., Giron, C., Mazzolini, M., d'Aspremont, A., Duren, R., Cusworth, D., Shindell, D., and Ciais, P.: Global Assessment of Oil and Gas Methane Ultra-Emitters, Science, 375, 557–561, https://doi.org/10.1126/science.abj4351, 2022.

Lelieveld, J., Gromov, S., Pozzer, A., and Taraborrelli, D.: Global Tropospheric Hydroxyl Distribution, Budget and Reactivity, Atmospheric Chemistry and Physics, 16, 12 477–12 493, https://doi.org/10.5194/acp-16-12477-2016, 2016.

Lin, X., Trainer, M., and Liu, S. C.: On the Nonlinearity of the Tropospheric Ozone Production, Journal of Geophysical Research: Atmospheres, 93, 15 879–15 888, https://doi.org/10.1029/JD093iD12p15879, 1988.

Liu, G., Peng, S., Lin, X., Ciais, P., Li, X., Xi, Y., Lu, Z., Chang, J., Saunois, M., Wu, Y., Patra, P., Chandra, N., Zeng, H., and Piao, S.: Recent Slowdown of Anthropogenic Methane Emissions in China Driven by Stabilized Coal Production, Environmental Science & Technology Letters, 8, 739–746, https://doi.org/10.1021/acs.estlett.1c00463, 2021.

Louis, J.-F.: A Parametric Model of Vertical Eddy Fluxes in the Atmosphere, Boundary-Layer Meteorology, 17, 187–202, https://doi.org/10.1007/BF00117978, 1979.

Malina, E., Yoshida, Y., Matsunaga, T., and Muller, J.-P.: Information Content Analysis: The Potential for Methane Isotopologue Retrieval from GOSAT-2, Atmospheric Measurement Techniques, 11, 1159–1179, https://doi.org/10.5194/amt-11-1159-2018, 2018.

Malina, E., Hu, H., Landgraf, J., and Veihelmann, B.: A Study of Synthetic $^{13}CH_4$ Retrievals from TROPOMI and Sentinel-5/UVNS, Atmospheric Measurement Techniques, 12, 6273–6301, https://doi.org/10.5194/amt-12-6273-2019, 2019.

Mannisenaho, V., Tsuruta, A., Backman, L., Houweling, S., Segers, A., Krol, M., Saunois, M., Poulter, B., Zhang, Z., Lan, X., Dlugokencky, E. J., Michel, S., White, J. W. C., and Aalto, T.: Global Atmospheric δ13CH4 and CH4 Trends for 2000–2020 from the Atmospheric Transport Model TM5 Using CH4 from Carbon Tracker Europe–CH4 Inversions, Atmosphere, 14, 1121, https://doi.org/10.3390/atmos14071121, 2023.

Martinez, A., Saunois, M., Poulter, B., Bousquet, P., Canadell, J. G., Jackson, R. B., Dlugokencky, E. J., Ciais, P., Bastviken, D., Blake, D. R., Castaldi, S., Etiope, G., Gedney, N., Höglund-Isaksson, L., Hugelius, G., Ito, A., Kleinen, T., Krummel, P. B., Liu, L., McDonald, K. C., Melton, J. R., Müller, J., Murguia-Flores, F., Niwa, Y., Noce, S., Parker, R. J., Peng, C., Ramonet, M., Riley, W. J., Rosentreter, J. A., Segers, A., Smith, S. J., Tian, H., Tubiello, F. N., Tsuruta, A., Weber, T. S., van der Werf, G. R., Worthy, D., Yoshida, Y., Zhang, W., Zhang, Z., Zheng, B., Zhu, Q., Zhu, Q., and Zhuang, Q.: Supplemental Data of the Global Carbon Project Methane Budget 2024 V1, https://doi.org/10.18160/GKQ9-2RHT, 2024.

https://doi.org/10.5194/essd-2025-668
Preprint. Discussion started: 13 February 2026

McNicol, G., Fluet-Chouinard, E., Ouyang, Z., Knox, S., Zhang, Z., Aalto, T., Bansal, S., Chang, K.-Y., Chen, M., Delwiche, K., Feron, S., Goeckede, M., Liu, J., Malhotra, A., Melton, J. R., Riley, W., Vargas, R., Yuan, K., Ying, Q., Zhu, Q., Alekseychik, P., Aurela, M., Billesbach, D. P., Campbell, D. I., Chen, J., Chu, H., Desai, A. R., Euskirchen, E., Goodrich, J., Griffis, T., Helbig, M., Hirano, T., Iwata, H., Jurasinski, G., King, J., Koebsch, F., Kolka, R., Krauss, K., Lohila, A., Mammarella, I., Nilson, M., Noormets, A., Oechel, W., Peichl, M., Sachs, T., Sakabe, A., Schulze, C., Sonnentag, O., Sullivan, R. C., Tuittila, E.-S., Ueyama, M., Vesala, T., Ward, E., Wille, C., Wong, G. X., Zona, D., Windham-Myers, L., Poulter, B., and Jackson, R. B.: Upscaling Wetland Methane Emissions From the FLUXNET-CH4 Eddy Covariance Network (UpCH4 v1.0): Model Development, Network Assessment, and Budget Comparison, AGU Advances, 4, e2023AV000 956, https://doi.org/10.1029/2023AV000956, 2023.

McNorton, J., Wilson, C., Gloor, M., Parker, R. J., Boesch, H., Feng, W., Hossaini, R., and Chipperfield, M. P.: Attribution of Recent Increases in Atmospheric Methane through 3-D Inverse Modelling, Atmospheric Chemistry and Physics, 18, 18 149–18 168, https://doi.org/10.5194/acp-18-18149-2018, 2018.

Melton, J. R., Wania, R., Hodson, E. L., Poulter, B., Ringeval, B., Spahni, R., Bohn, T., Avis, C. A., Beerling, D. J., Chen, G., Eliseev, A. V., Denisov, S. N., Hopcroft, P. O., Lettenmaier, D. P., Riley, W. J., Singarayer, J. S., Subin, Z. M., Tian, H., Zürcher, S., Brovkin, V., van Bodegom, P. M., Kleinen, T., Yu, Z. C., and Kaplan, J. O.: Present State of Global Wetland Extent and Wetland Methane Modelling: Conclusions from a Model Inter-Comparison Project (WETCHIMP), Biogeosciences, 10, 753–788, https://doi.org/10.5194/bg-10-753-2013, 2013.

Menoud, M.: The European Methane Isotope Database Coupled with a Global Inventory of Fossil and Non-Fossil δ13C- and δ2H-CH4 Source Signature Measurements, https://public.yoda.uu.nl/science/UU01/YP43IN.html, https://doi.org/10.24416/UU01-YP43IN, 2022.

Menoud, M., van der Veen, C., Lowry, D., Fernandez, J. M., Bakkaloglu, S., France, J. L., Fisher, R. E., Maazallahi, H., Stanisavljević, M., Nęcki, J., Vinkovic, K., Łakomiec, P., Rinne, J., Korbeń, P., Schmidt, M., Defratyka, S., Yver-Kwok, C., Andersen, T., Chen, H., and Röckmann, T.: New Contributions of Measurements in Europe to the Global Inventory of the Stable Isotopic Composition of Methane, Earth System Science Data, 14, 4365–4386, https://doi.org/10.5194/essd-14-4365-2022, 2022.

Menoud, M., Thomas, R., Carina, v. d. V., Julianne, F., Semra, B., Dave, L., James, F., Rebecca, F., Hossein, M., Piotr, K., Martina, S., Mila, S., Jaroslaw, N., Patryk, Ł., Janne, R., Sara, D., Camille, Y.-K., Katarina, V., Truls, A., and Huilin, C.: The European Methane Isotope Database Coupled with a Global Inventory of Fossil and Non-Fossil δ13C- and δ2H-CH4 Source Signature Measurements, https://doi.org/10.24416/UU01-YP43IN, 2024.

Michel, S. E., Lan, X., Miller, J., Tans, P., Clark, J. R., Schaefer, H., Sperlich, P., Brailsford, G., Morimoto, S., Moossen, H., and Li, J.: Rapid Shift in Methane Carbon Isotopes Suggests Microbial Emissions Drove Record High Atmospheric Methane Growth in 2020–2022, Proceedings of the National Academy of Sciences, 121, e2411212 121, https://doi.org/10.1073/pnas.2411212121, 2024.

Milkov, A. V. and Etiope, G.: Revised Genetic Diagrams for Natural Gases Based on a Global Dataset of >20,000 Samples, Organic Geochemistry, 125, 109–120, https://doi.org/10.1016/j.orggeochem.2018.09.002, 2018.

Milkov, A. V., Faiz, M., and Etiope, G.: Geochemistry of Shale Gases from around the World: Composition, Origins, Isotope Reversals and Rollovers, and Implications for the Exploration of Shale Plays, Organic Geochemistry, 143, 103 997, https://doi.org/10.1016/j.orggeochem.2020.103997, 2020a.

Milkov, A. V., Schwietzke, S., Allen, G., Sherwood, O. A., and Etiope, G.: Using Global Isotopic Data to Constrain the Role of Shale Gas Production in Recent Increases in Atmospheric Methane, Scientific Reports, 10, 4199, https://doi.org/10.1038/s41598-020-61035-w, 2020b.

https://doi.org/10.5194/essd-2025-668
Preprint. Discussion started: 13 February 2026

Nicely, J. M., Salawitch, R. J., Canty, T., Anderson, D. C., Arnold, S. R., Chipperfield, M. P., Emmons, L. K., Flemming, J., Huijnen, V., Kinnison, D. E., Lamarque, J.-F., Mao, J., Monks, S. A., Steenrod, S. D., Tilmes, S., and Turquety, S.: Quantifying the Causes of Differences in Tropospheric OH within Global Models, Journal of Geophysical Research: Atmospheres, 122, 1983–2007, https://doi.org/10.1002/2016JD026239, 2017.

Nisbet, E. G.: Climate Feedback on Methane from Wetlands, Nature Climate Change, 13, 421–422, https://doi.org/10.1038/s41558-023-01634-3, 2023.

Nisbet, E. G., Dlugokencky, E. J., Manning, M. R., Lowry, D., Fisher, R. E., France, J. L., Michel, S. E., Miller, J. B., White, J. W. C., Vaughn, B., Bousquet, P., Pyle, J. A., Warwick, N. J., Cain, M., Brownlow, R., Zazzeri, G., Lanoisellé, M., Manning, A. C., Gloor, E., Worthy, D. E. J., Brunke, E.-G., Labuschagne, C., Wolff, E. W., and Ganesan, A. L.: Rising Atmospheric Methane: 2007–2014 Growth and Isotopic Shift, Global Biogeochemical Cycles, 30, 1356–1370, https://doi.org/10.1002/2016GB005406, 2016.

Nisbet, E. G., Manning, M. R., Dlugokencky, E. J., Fisher, R. E., Lowry, D., Michel, S. E., Myhre, C. L., Platt, S. M., Allen, G., Bousquet, P., Brownlow, R., Cain, M., France, J. L., Hermansen, O., Hossaini, R., Jones, A. E., Levin, I., Manning, A. C., Myhre, G., Pyle, J. A., Vaughn, B. H., Warwick, N. J., and White, J. W. C.: Very Strong Atmospheric Methane Growth in the 4 Years 2014–2017: Implications for the Paris Agreement, Global Biogeochemical Cycles, 33, 318–342, https://doi.org/10.1029/2018GB006009, 2019.

Nisbet, E. G., Manning, M. R., Dlugokencky, E. J., Michel, S. E., Lan, X., Röckmann, T., Denier van der Gon, H. A. C., Schmitt, J., Palmer, P. I., Dyonisius, M. N., Oh, Y., Fisher, R. E., Lowry, D., France, J. L., White, J. W. C., Brailsford, G., and Bromley, T.: Atmospheric Methane: Comparison Between Methane's Record in 2006–2022 and During Glacial Terminations, Global Biogeochemical Cycles, 37, e2023GB007 875, https://doi.org/10.1029/2023GB007875, 2023.

Ocko, I. B., Sun, T., Shindell, D., Oppenheimer, M., Hristov, A. N., Pacala, S. W., Mauzerall, D. L., Xu, Y., and Hamburg, S. P.: Acting Rapidly to Deploy Readily Available Methane Mitigation Measures by Sector Can Immediately Slow Global Warming, Environmental Research Letters, 16, 054 042, https://doi.org/10.1088/1748-9326/abf9c8, 2021.

Oh, Y., Zhuang, Q., Welp, L. R., Liu, L., Lan, X., Basu, S., Dlugokencky, E. J., Bruhwiler, L., Miller, J. B., Michel, S. E., Schwietzke, S., Tans, P., Ciais, P., and Chanton, J. P.: Improved Global Wetland Carbon Isotopic Signatures Support Post-2006 Microbial Methane Emission Increase, Communications Earth & Environment, 3, 1–12, https://doi.org/10.1038/s43247-022-00488-5, 2022.

O'Rourke, P., Smith, S., Mott, A., Ahsan, H., Mcduffie, E., Crippa, M., Klimont, Z., Mcdonald, B., Wang, S., Nicholson, M., Hoesly, R., and Feng, L.: CEDS V_2021_04_21 Gridded Emissions Data, https://doi.org/10.25584/PNNLDATAHUB/1779095, 2021.

Parker, R. J., Wilson, C., Comyn-Platt, E., Hayman, G., Marthews, T. R., Bloom, A. A., Lunt, M. F., Gedney, N., Dadson, S. J., McNorton, J., Humpage, N., Boesch, H., Chipperfield, M. P., Palmer, P. I., and Yamazaki, D.: Evaluation of Wetland CH_4 in the Joint UK Land Environment Simulator (JULES) Land Surface Model Using Satellite Observations, Biogeosciences, 19, 5779–5805, https://doi.org/10.5194/bg-19-5779-2022, 2022.

Patra, P. K., Houweling, S., Krol, M., Bousquet, P., Belikov, D., Bergmann, D., Bian, H., Cameron-Smith, P., Chipperfield, M. P., Corbin, K., Fortems-Cheiney, A., Fraser, A., Gloor, E., Hess, P., Ito, A., Kawa, S. R., Law, R. M., Loh, Z., Maksyutov, S., Meng, L., Palmer, P. I., Prinn, R. G., Rigby, M., Saito, R., and Wilson, C.: TransCom Model Simulations of CH4 and Related Species: Linking Transport, Surface Flux and Chemical Loss with CH4 Variability in the Troposphere and Lower Stratosphere, Atmos. Chem. Phys., 11, 12 813–12 837, https://doi.org/10.5194/acp-11-12813-2011, 2011.

Patra, P. K., Krol, M. C., Prinn, R. G., Takigawa, M., Mühle, J., Montzka, S. A., Lal, S., Yamashita, Y., Naus, S., Chandra, N., Weiss, R. F., Krummel, P. B., Fraser, P. J., O'Doherty, S., and Elkins, J. W.: Methyl Chloroform Continues to Constrain the Hydroxyl (OH) Variability in the Troposphere, Journal of Geophysical Research: Atmospheres, 126, e2020JD033 862, https://doi.org/10.1029/2020JD033862, 2021.

https://doi.org/10.5194/essd-2025-668
Preprint. Discussion started: 13 February 2026

Pison, I., Bousquet, P., Chevallier, F., Szopa, S., and Hauglustaine, D.: Multi-Species Inversion of CH4, CO and H2 Emissions from Surface Measurements, Atmos. Chem. Phys., 9, 5281–5297, https://doi.org/10.5194/acp-9-5281-2009, 2009.

Poulter, B., Bousquet, P., Canadell, J. G., Ciais, P., Peregon, A., Saunois, M., Arora, V. K., Beerling, D. J., Brovkin, V., Jones, C. D., Joos, F., Gedney, N., Ito, A., Kleinen, T., Koven, C. D., McDonald, K., Melton, J. R., Peng, C., Peng, S., Prigent, C., Schroeder, R., Riley, W. J., Saito, M., Spahni, R., Tian, H., Taylor, L., Viovy, N., Wilton, D., Wiltshire, A., Xu, X., Zhang, B., Zhang, Z., and Zhu, Q.: Global Wetland Contribution to 2000–2012 Atmospheric Methane Growth Rate Dynamics, Environmental Research Letters, 12, 094 013, https://doi.org/10.1088/1748-9326/aa8391, 2017.

Prather, M. J., Holmes, C. D., and Hsu, J.: Reactive Greenhouse Gas Scenarios: Systematic Exploration of Uncertainties and the Role of Atmospheric Chemistry, Geophys. Res. Lett., 39, L09 803, https://doi.org/10.1029/2012GL051440, 2012.

Qin, S., Tang, X., Song, Y., and Wang, H.: Distribution and Fractionation Mechanism of Stable Carbon Isotope of Coalbed Methane, Science in China Series D: Earth Sciences, 49, 1252–1258, https://doi.org/10.1007/s11430-006-2036-3, 2006.

Randerson, J. T., Chen, Y., van der Werf, G. R., Rogers, B. M., and Morton, D. C.: Global Burned Area and Biomass Burning Emissions from Small Fires, Journal of Geophysical Research: Biogeosciences, 117, https://doi.org/10.1029/2012JG002128, 2012.

Remaud, M., Chevallier, F., Cozic, A., Lin, X., and Bousquet, P.: On the Impact of Recent Developments of the LMDz Atmospheric General Circulation Model on the Simulation of CO_2 Transport, Geoscientific Model Development, 11, 4489–4513, https://doi.org/10.5194/gmd-11-4489-2018, 2018.

Rigby, M., Montzka, S. A., Prinn, R. G., White, J. W. C., Young, D., O'Doherty, S., Lunt, M. F., Ganesan, A. L., Manning, A. J., Simmonds, P. G., Salameh, P. K., Harth, C. M., Mühle, J., Weiss, R. F., Fraser, P. J., Steele, L. P., Krummel, P. B., McCulloch, A., and Park, S.: Role of Atmospheric Oxidation in Recent Methane Growth, Proceedings of the National Academy of Sciences, 114, 5373–5377, https://doi.org/10.1073/pnas.1616426114, 2017.

Sansone, F. J., Popp, B. N., Gasc, A., Graham, A. W., and Rust, T. M.: Highly Elevated Methane in the Eastern Tropical North Pacific and Associated Isotopically Enriched Fluxes to the Atmosphere, Geophysical Research Letters, 28, 4567–4570, https://doi.org/10.1029/2001GL013460, 2001.

Saueressig, G., Bergamaschi, P., Crowley, J. N., Fischer, H., and Harris, G. W.: Carbon Kinetic Isotope Effect in the Reaction of CH4 with Cl Atoms, Geophysical Research Letters, 22, 1225–1228, https://doi.org/10.1029/95GL00881, 1995.

Saueressig, G., Crowley, J. N., Bergamaschi, P., Brühl, C., Brenninkmeijer, C. A. M., and Fischer, H.: Carbon 13 and D Kinetic Isotope Effects in the Reactions of CH4 with O(1 D) and OH: New Laboratory Measurements and Their Implications for the Isotopic Composition of Stratospheric Methane, Journal of Geophysical Research: Atmospheres, 106, 23 127–23 138, https://doi.org/10.1029/2000JD000120, 2001.

Saunois, M., Bousquet, P., Poulter, B., Peregon, A., Ciais, P., Canadell, J. G., Dlugokencky, E. J., Etiope, G., Bastviken, D., Houweling, S., Janssens-Maenhout, G., Tubiello, F. N., Castaldi, S., Jackson, R. B., Alexe, M., Arora, V. K., Beerling, D. J., Bergamaschi, P., Blake, D. R., Brailsford, G., Bruhwiler, L., Crevoisier, C., Crill, P., Covey, K., Frankenberg, C., Gedney, N., Höglund-Isaksson, L., Ishizawa, M., Ito, A., Joos, F., Kim, H.-S., Kleinen, T., Krummel, P., Lamarque, J.-F., Langenfelds, R., Locatelli, R., Machida, T., Maksyutov, S., Melton, J. R., Morino, I., Naik, V., O'Doherty, S., Parmentier, F.-J. W., Patra, P. K., Peng, C., Peng, S., Peters, G. P., Pison, I., Prinn, R., Ramonet, M., Riley, W. J., Saito, M., Santini, M., Schroeder, R., Simpson, I. J., Spahni, R., Takizawa, A., Thornton, B. F., Tian, H., Tohjima, Y., Viovy, N., Voulgarakis, A., Weiss, R., Wilton, D. J., Wiltshire, A., Worthy, D., Wunch, D., Xu, X., Yoshida, Y., Zhang, B., Zhang, Z., and Zhu, Q.: Variability and Quasi-Decadal Changes in the Methane Budget over the Period 2000–2012, Atmospheric Chemistry and Physics, 17, 11 135–11 161, https://doi.org/10.5194/acp-17-11135-2017, 2017.

https://doi.org/10.5194/essd-2025-668
Preprint. Discussion started: 13 February 2026

Saunois, M., Stavert, A. R., Poulter, B., Bousquet, P., Canadell, J. G., Jackson, R. B., Raymond, P. A., Dlugokencky, E. J., Houweling, S., Patra, P. K., Ciais, P., Arora, V. K., Bastviken, D., Bergamaschi, P., Blake, D. R., Brailsford, G., Bruhwiler, L., Carlson, K. M., Carrol, M., Castaldi, S., Chandra, N., Crevoisier, C., Crill, P. M., Covey, K., Curry, C. L., Etiope, G., Frankenberg, C., Gedney, N., Hegglin, M. I., Höglund-Isaksson, L., Hugelius, G., Ishizawa, M., Ito, A., Janssens-Maenhout, G., Jensen, K. M., Joos, F., Kleinen, T., Krummel, P. B., Langenfelds, R. L., Laruelle, G. G., Liu, L., Machida, T., Maksyutov, S., McDonald, K. C., McNorton, J., Miller, P. A., Melton, J. R., Morino, I., Müller, J., Murguia-Flores, F., Naik, V., Niwa, Y., Noce, S., O'Doherty, S., Parker, R. J., Peng, C., Peng, S., Peters, G. P., Prigent, C., Prinn, R., Ramonet, M., Regnier, P., Riley, W. J., Rosentreter, J. A., Segers, A., Simpson, I. J., Shi, H., Smith, S. J., Steele, L. P., Thornton, B. F., Tian, H., Tohjima, Y., Tubiello, F. N., Tsuruta, A., Viovy, N., Voulgarakis, A., Weber, T. S., van Weele, M., van der Werf, G. R., Weiss, R. F., Worthy, D., Wunch, D., Yin, Y., Yoshida, Y., Zhang, W., Zhang, Z., Zhao, Y., Zheng, B., Zhu, Q., Zhu, Q., and Zhuang, Q.: The Global Methane Budget 2000–2017, Earth System Science Data, 12, 1561–1623, https://doi.org/10.5194/essd-12-1561-2020, 2020.

Saunois, M., Martinez, A., Poulter, B., Zhang, Z., Raymond, P. A., Regnier, P., Canadell, J. G., Jackson, R. B., Patra, P. K., Bousquet, P., Ciais, P., Dlugokencky, E. J., Lan, X., Allen, G. H., Bastviken, D., Beerling, D. J., Belikov, D. A., Blake, D. R., Castaldi, S., Crippa, M., Deemer, B. R., Dennison, F., Etiope, G., Gedney, N., Höglund-Isaksson, L., Holgerson, M. A., Hopcroft, P. O., Hugelius, G., Ito, A., Jain, A. K., Janardanan, R., Johnson, M. S., Kleinen, T., Krummel, P. B., Lauerwald, R., Li, T., Liu, X., McDonald, K. C., Melton, J. R., Mühle, J., Müller, J., Murguia-Flores, F., Niwa, Y., Noce, S., Pan, S., Parker, R. J., Peng, C., Ramonet, M., Riley, W. J., Rocher-Ros, G., Rosentreter, J. A., Sasakawa, M., Segers, A., Smith, S. J., Stanley, E. H., Thanwerdas, J., Tian, H., Tsuruta, A., Tubiello, F. N., Weber, T. S., van der Werf, G. R., Worthy, D. E. J., Xi, Y., Yoshida, Y., Zhang, W., Zheng, B., Zhu, Q., Zhu, Q., and Zhuang, Q.: Global Methane Budget 2000–2020, Earth System Science Data, 17, 1873–1958, https://doi.org/10.5194/essd-17-1873-2025, 2025.

Scarpelli, T. R., Jacob, D. J., Grossman, S., Lu, X., Qu, Z., Sulprizio, M. P., Zhang, Y., Reuland, F., Gordon, D., and Worden, J. R.: Updated Global Fuel Exploitation Inventory (GFEI) for Methane Emissions from the Oil, Gas, and Coal Sectors: Evaluation with Inversions of Atmospheric Methane Observations, Atmospheric Chemistry and Physics, 22, 3235–3249, https://doi.org/10.5194/acp-22-3235-2022, 2022.

Schaefer, H.: On the Causes and Consequences of Recent Trends in Atmospheric Methane, Current Climate Change Reports, 5, 259–274, https://doi.org/10.1007/s40641-019-00140-z, 2019.

Schaefer, H., Fletcher, S. E. M., Veidt, C., Lassey, K. R., Brailsford, G. W., Bromley, T. M., Dlugokencky, E. J., Michel, S. E., Miller, J. B., Levin, I., Lowe, D. C., Martin, R. J., Vaughn, B. H., and White, J. W. C.: A 21st-Century Shift from Fossil-Fuel to Biogenic Methane Emissions Indicated by 13CH4, Science, 352, 80–84, https://doi.org/10.1126/science.aad2705, 2016.

Schoell, M., Jenden, P. D., Beeunas, M. A., and Coleman, D. D.: Isotope Analyses of Gases in Gas Field and Gas Storage Operations, in: SPE Gas Technology Symposium, OnePetro, https://doi.org/10.2118/26171-MS, 1993.

Schuldt, K. N., Aalto, T., Andrade, M., Arlyn Andrews, Apadula, F., Jgor Arduini, Arnold, S., Baier, B., Bäni, L., Bartyzel, J., Bergamaschi, P., Biermann, T., Biraud, S. C., Pierre-Eric Blanc, Boenisch, H., Brailsford, G., Brand, W. A., Brunner, D., Bui, T. P. V., Van Den Bulk, P., Benoit Burban, Francescopiero Calzolari, Chang, C. S., Huilin Chen, Lukasz Chmura, St. Clair, J. M., Sites Climadat, Coletta, J. D., Colomb, A., Condori, L., Conen, F., Conil, S., Couret, C., Cristofanelli, P., Cuevas, E., Curcoll, R., Daube, B., Davis, K. J., Dean-Day, J. M., Delmotte, M., Ankur Desai, DiGangi, E., DiGangi, J. P., Elsasser, M., Emmenegger, L., Forster, G., Frumau, A., Fuente-Lastra, M., Galkowski, M., Gatti, L. V., Gehrlein, T., Gerbig, C., Francois Gheusi, Gloor, E., Goto, D., Hammer, S., Hanisco, T. F., Haszpra, L., Hatakka, J., Heimann, M., Heliasz, M., Heltai, D., Henne, S., Hensen, A., Hermans, C., Hermansen, O., Hoheisel, A., Holst, J., Di Iorio, T., Iraci, L. T., Ivakhov, V., Jaffe, D. A., Jordan, A., Joubert, W., Kang, H.-Y., Karion, A., Kazan, V., Keeling, R. F., Keronen,

https://doi.org/10.5194/essd-2025-668
Preprint. Discussion started: 13 February 2026

P., Kers, B., Jooil Kim, Klausen, J., Kneuer, T., Ko, M.-Y., Kolari, P., Kominkova, K., Kort, E., Kozlova, E., Krummel, P. B., Kubistin, D., Kulawik, S. S., Kumps, N., Labuschagne, C., Lan, X., Langenfelds, R. L., Lanza, A., Laurent, O., Laurila, T., Lauvaux, T., Lavric, J., Choong-Hoon Lee, Lee, J., Lehner, I., Lehtinen, K., Leppert, R., Leskinen, A., Leuenberger, M., Levin, I., Levula, J., Lindauer, M., Lindroth, A., Mikaell Ottosson Löfvenius, Loh, Z. M., Lopez, M., Lowry, D., Lunder, C. R., Machida, T., Mammarella, I., Manca, G., Manning, A., Marek, M. V., Marklund, P., Marrero, J. E., Martin, D., Martin, M. Y., Giordane A. Martins, Matsueda, H., De Mazière, M., McKain, K., Meinhardt, F., Menoud, M., Jean-Marc Metzger, Miles, N. L., Miller, C. E., Miller, J. B., Mölder, M., Monteiro, V., Montzka, S., Moore, F., Moossen, H., Moreno, C., Morgan, E., Josep-Anton Morgui, Morimoto, S., Müller-Williams, J., Munro, D., Mutuku, M., Myhre, C. L., Jaroslaw Necki, Nichol, S., Nisbet, E., Niwa, Y., Njiru, D. M., Noe, S. M., O'Doherty, S., Obersteiner, F., Parworth, C. L., Peltola, O., Peters, W., Philippon, C., Piacentino, S., Pichon, J. M., Pickers, P., Pitt, J., Pittman, J., Plass-Dülmer, C., Platt, S. M., Popa, M. E., Prinzivalli, S., Ramonet, M., Richardson, S. J., Louis-Jeremy Rigouleau, Rivas, P. P., Röckmann, T., Rothe, M., Yves-Alain Roulet, Ju-Mee Ryoo, Santoni, G., Di Sarra, A. G., Sasakawa, M., Schaefer, H., Scheeren, B., Schmidt, M., Schuck, T., Schumacher, M., Seifert, T., Sha, M. K., Shepson, P., Daegeun Shin, Sloop, C. D., Smale, D., Smith, P. D., Sørensen, L. L., De Souza, R. A. F., Spain, G., Steger, D., Steinbacher, M., Stephens, B., Sweeney, C., Taipale, R., Takatsuji, S., Thoning, K., Timas, H., Torn, M., Trisolino, P., Turnbull, J., Van Der Veen, C., Vermeulen, A., Viner, B., Vitkova, G., De Vries, M., Watson, A., Weiss, R., Weyrauch, D., Wofsy, S. C., Worsey, J., Worthy, D., Xueref-Remy, I., Yates, E. L., Dickon Young, Yver-Kwok, C., Zaehle, S., Zahn, A., Zazzeri, G., Zellweger, C., and Miroslaw Zimnoch: Multi-Laboratory Compilation of Atmospheric Carbon Dioxide Data for the Period 1983-2023; obspack_ch4_1_GLOBALVIEWplus_v7.0_2024-10-29, https://doi.org/10.25925/20241001, 2024.

Schuldt, K. N., Arlyn Andrews, Bartyzel, J., Brailsford, G., Brand, W. A., Huilin Chen, Clark, R., Heimann, M., Jordan, A., Kers, B., Lan, X., Lavric, J., Lowry, D., Menoud, M., Michel, S. E., Miller, J. B., Moossen, H., Morimoto, S., Jaroslaw Necki, Nisbet, E., Ortega, J., Popa, M. E., Röckmann, T., Rothe, M., Schaefer, H., Scheeren, B., Sweeney, C., Umezawa, T., Van Der Veen, C., De Vries, M., and Zazzeri, G.: Multi-Laboratory Compilation of Atmospheric Methane Isotope Data for the Period 1991-2023; Obspack_ch4c13_1_methane-Isotope_2025-04-07, https://doi.org/10.25925/20250401, 2025.

Schwietzke, S., Griffin, W. M., Matthews, H. S., and Bruhwiler, L. M. P.: Global Bottom-Up Fossil Fuel Fugitive Methane and Ethane Emissions Inventory for Atmospheric Modeling, ACS Sustainable Chemistry & Engineering, 2, 1992–2001, https://doi.org/10.1021/sc500163h, 2014.

Schwietzke, S., Sherwood, O. A., Bruhwiler, L. M. P., Miller, J. B., Etiope, G., Dlugokencky, E. J., Michel, S. E., Arling, V. A., Vaughn, B. H., White, J. W. C., and Tans, P. P.: Upward Revision of Global Fossil Fuel Methane Emissions Based on Isotope Database, Nature, 538, 88–91, https://doi.org/10.1038/nature19797, 2016.

Sherwood, O. A., Schwietzke, S., Arling, V. A., and Etiope, G.: Global Inventory of Gas Geochemistry Data from Fossil Fuel, Microbial and Burning Sources, Version 2017, Earth System Science Data, 9, 639–656, https://doi.org/10.5194/essd-9-639-2017, 2017.

Sherwood, O. A., Schwietzke, S., and Lan, X.: Global δ13C-CH4 Source Signature Inventory 2020, https://doi.org/10.15138/qn55-e011, 2021.

Shindell, D., Ravishankara, A. R., Kuylenstierna, J. C. I., Michalopoulou, E., Höglund-Isaksson, L., Zhang, Y., Seltzer, K., Ru, M., Castelino, R., Faluvegi, G., Naik, V., Horowitz, L., He, J., Lamarque, J.-F., Sudo, K., Collins, W. J., Malley, C., Harmsen, M., Stark, K., Junkin, J., Li, G., Glick, A., and Borgford-Parnell, N.: Global Methane Assessment: Benefits and Costs of Mitigating Methane Emissions, 2021.

Snover, A. K. and Quay, P. D.: Hydrogen and Carbon Kinetic Isotope Effects during Soil Uptake of Atmospheric Methane, Global Biogeochemical Cycles, 14, 25–39, https://doi.org/10.1029/1999GB900089, 2000.

https://doi.org/10.5194/essd-2025-668
Preprint. Discussion started: 13 February 2026

Stavert, A. R., Saunois, M., Canadell, J. G., Poulter, B., Jackson, R. B., Regnier, P., Lauerwald, R., Raymond, P. A., Allen, G. H., Patra, P. K., Bergamaschi, P., Bousquet, P., Chandra, N., Ciais, P., Gustafson, A., Ishizawa, M., Ito, A., Kleinen, T., Maksyutov, S., McNorton, J., Melton, J. R., Müller, J., Niwa, Y., Peng, S., Riley, W. J., Segers, A., Tian, H., Tsuruta, A., Yin, Y., Zhang, Z., Zheng, B., and Zhuang, Q.: Regional Trends and Drivers of the Global Methane Budget, Global Change Biology, 28, 182–200, https://doi.org/10.1111/gcb.15901, 2022.

Stevenson, D. S., Zhao, A., Naik, V., O'Connor, F. M., Tilmes, S., Zeng, G., Murray, L. T., Collins, W. J., Griffiths, P. T., Shim, S., Horowitz, L. W., Sentman, L. T., and Emmons, L.: Trends in Global Tropospheric Hydroxyl Radical and Methane Lifetime since 1850 from AerChemMIP, Atmospheric Chemistry and Physics, 20, 12 905–12 920, https://doi.org/10.5194/acp-20-12905-2020, 2020.

Still, C. J., Berry, J. A., Collatz, G. J., and DeFries, R. S.: Global Distribution of C3 and C4 Vegetation: Carbon Cycle Implications, Global Biogeochemical Cycles, 17, 6–1–6–14, https://doi.org/10.1029/2001GB001807, 2003.

Stocker, T.: Climate Change 2013: The Physical Science Basis: Working Group I Contribution to the Fifth Assessment Report of the Intergovernmental Panel on Climate Change, Cambridge University Press, ISBN 978-1-107-05799-9, 2014.

Sugimoto, A., Inoue, T., Kirtibutr, N., and Abe, T.: Methane Oxidation by Termite Mounds Estimated by the Carbon Isotopic Composition of Methane, Global Biogeochemical Cycles, 12, 595–605, https://doi.org/10.1029/98GB02266, 1998.

Tans, P. P.: A Note on Isotopic Ratios and the Global Atmospheric Methane Budget, Global Biogeochemical Cycles, 11, 77–81, https://doi.org/10.1029/96GB03940, 1997.

Thanwerdas, J., Saunois, M., Berchet, A., Pison, I., Vaughn, B. H., Michel, S. E., and Bousquet, P.: Variational Inverse Modeling within the Community Inversion Framework v1.1 to Assimilate $\delta^{13}C(CH_4)$ and CH_4: A Case Study with Model LMDz-SACS, Geoscientific Model Development, 15, 4831–4851, https://doi.org/10.5194/gmd-15-4831-2022, 2022a.

Thanwerdas, J., Saunois, M., Pison, I., Hauglustaine, D., Berchet, A., Baier, B., Sweeney, C., and Bousquet, P.: How Do Cl Concentrations Matter for the Simulation of CH_4 and $\delta^{13}C(CH_4)$ and Estimation of the CH_4 Budget through Atmospheric Inversions?, Atmospheric Chemistry and Physics, 22, 15 489–15 508, https://doi.org/10.5194/acp-22-15489-2022, 2022b.

Thanwerdas, J., Saunois, M., Berchet, A., Pison, I., and Bousquet, P.: Investigation of the Renewed Methane Growth Post-2007 with High-Resolution 3-D Variational Inverse Modeling and Isotopic Constraints, Atmospheric Chemistry and Physics, 24, 2129–2167, https://doi.org/10.5194/acp-24-2129-2024, 2024.

Thompson, R. L., Nisbet, E. G., Pisso, I., Stohl, A., Blake, D., Dlugokencky, E. J., Helmig, D., and White, J. W. C.: Variability in Atmospheric Methane From Fossil Fuel and Microbial Sources Over the Last Three Decades, Geophysical Research Letters, 45, 11,499–11,508, https://doi.org/10.1029/2018GL078127, 2018.

Tian, H., Xu, X., Liu, M., Ren, W., Zhang, C., Chen, G., and Lu, C.: Spatial and Temporal Patterns of CH_4 and N_2O Fluxes in Terrestrial Ecosystems of North America during 1979–2008: Application of a Global Biogeochemistry Model, Biogeosciences, 7, 2673–2694, https://doi.org/10.5194/bg-7-2673-2010, 2010.

Turner, A. J., Frankenberg, C., and Kort, E. A.: Interpreting Contemporary Trends in Atmospheric Methane, Proceedings of the National Academy of Sciences, 116, 2805–2813, https://doi.org/10.1073/pnas.1814297116, 2019.

UNEP: United Nations Environment Programme/Climate and Clean Air Coalition. Global Methane Assessment: 2030 Baseline Report., Tech. rep., Nairobi, 2022.

Van Bergen, T. J. H. M., Barros, N., Mendonça, R., Aben, R. C. H., Althuizen, I. H. J., Huszar, V., Lamers, L. P. M., Lürling, M., Roland, F., and Kosten, S.: Seasonal and Diel Variation in Greenhouse Gas Emissions from an Urban Pond and Its Major Drivers, Limnology and Oceanography, 64, 2129–2139, https://doi.org/10.1002/lno.11173, 2019.

https://doi.org/10.5194/essd-2025-668
Preprint. Discussion started: 13 February 2026

van Wees, D., van der Werf, G. R., Randerson, J. T., Rogers, B. M., Chen, Y., Veraverbeke, S., Giglio, L., and Morton, D. C.: Global Biomass Burning Fuel Consumption and Emissions at 500 m Spatial Resolution Based on the Global Fire Emissions Database (GFED), Geoscientific Model Development, 15, 8411–8437, https://doi.org/10.5194/gmd-15-8411-2022, 2022.

Vanselow, S., Schneising, O., Buchwitz, M., Reuter, M., Bovensmann, H., Boesch, H., and Burrows, J. P.: Automated Detection of Regions with Persistently Enhanced Methane Concentrations Using Sentinel-5 Precursor Satellite Data, Atmospheric Chemistry and Physics, 24, 10 441–10 473, https://doi.org/10.5194/acp-24-10441-2024, 2024.

Wang, X., Jacob, D. J., Downs, W., Zhai, S., Zhu, L., Shah, V., Holmes, C. D., Sherwen, T., Alexander, B., Evans, M. J., Eastham, S. D., Neuman, J. A., Veres, P. R., Koenig, T. K., Volkamer, R., Huey, L. G., Bannan, T. J., Percival, C. J., Lee, B. H., and Thornton, J. A.: Global Tropospheric Halogen (Cl, Br, I) Chemistry and Its Impact on Oxidants, Atmospheric Chemistry and Physics, 21, 13 973–13 996, https://doi.org/10.5194/acp-21-13973-2021, 2021.

Wang, X., Liu, C.-Q., Yi, Y., Zeng, M., Li, S.-L., and Niu, X.: Machine Learning Predicts the Methane Clumped Isotopologue (12CH2D2) Distributions Constrain Biogeochemical Processes and Estimates the Potential Budget, Environmental Science & Technology, 57, 17 876–17 888, https://doi.org/10.1021/acs.est.3c00184, 2023.

Weber, T., Wiseman, N. A., and Kock, A.: Global Ocean Methane Emissions Dominated by Shallow Coastal Waters, Nature Communications, 10, 4584, https://doi.org/10.1038/s41467-019-12541-7, 2019.

Wei, M., Yu, Z., Jiang, Z., and Zhang, H.: Microbial Diversity and Biogenic Methane Potential of a Thermogenic-Gas Coal Mine, International Journal of Coal Geology, 134–135, 96–107, https://doi.org/10.1016/j.coal.2014.09.008, 2014.

Worden, J. R., Bloom, A. A., Pandey, S., Jiang, Z., Worden, H. M., Walker, T. W., Houweling, S., and Röckmann, T.: Reduced Biomass Burning Emissions Reconcile Conflicting Estimates of the Post-2006 Atmospheric Methane Budget, Nature Communications, 8, 2227, https://doi.org/10.1038/s41467-017-02246-0, 2017.

Zhang, Z., Poulter, B., Feldman, A. F., Ying, Q., Ciais, P., Peng, S., and Li, X.: Recent Intensification of Wetland Methane Feedback, Nature Climate Change, 13, 430–433, https://doi.org/10.1038/s41558-023-01629-0, 2023.

Zhao, Y., Saunois, M., Bousquet, P., Lin, X., Berchet, A., Hegglin, M. I., Canadell, J. G., Jackson, R. B., Hauglustaine, D. A., Szopa, S., Stavert, A. R., Abraham, N. L., Archibald, A. T., Bekki, S., Deushi, M., Jöckel, P., Josse, B., Kinnison, D., Kirner, O., Marécal, V., O'Connor, F. M., Plummer, D. A., Revell, L. E., Rozanov, E., Stenke, A., Strode, S., Tilmes, S., Dlugokencky, E. J., and Zheng, B.: Inter-Model Comparison of Global Hydroxyl Radical (OH) Distributions and Their Impact on Atmospheric Methane over the 2000–2016 Period, Atmospheric Chemistry and Physics, 19, 13 701–13 723, https://doi.org/10.5194/acp-19-13701-2019, 2019.

Zimmermann, P. H., Brenninkmeijer, C. A. M., Pozzer, A., Jöckel, P., Winterstein, F., Zahn, A., Houweling, S., and Lelieveld, J.: Model Simulations of Atmospheric Methane (1997–2016) and Their Evaluation Using NOAA and AGAGE Surface and IAGOS-CARIBIC Aircraft Observations, Atmospheric Chemistry and Physics, 20, 5787–5809, https://doi.org/10.5194/acp-20-5787-2020, 2020.